

1993

# Determining char burning and sulfur sorption rates from dynamic analysis of CO<sub>2</sub> and SO<sub>2</sub> profiles

Nearchos J. Christofides  
*Iowa State University*

Follow this and additional works at: <https://lib.dr.iastate.edu/rtd>

 Part of the [Chemical Engineering Commons](#), and the [Mechanical Engineering Commons](#)

## Recommended Citation

Christofides, Nearchos J., "Determining char burning and sulfur sorption rates from dynamic analysis of CO<sub>2</sub> and SO<sub>2</sub> profiles " (1993). *Retrospective Theses and Dissertations*. 10220.  
<https://lib.dr.iastate.edu/rtd/10220>

This Dissertation is brought to you for free and open access by the Iowa State University Capstones, Theses and Dissertations at Iowa State University Digital Repository. It has been accepted for inclusion in Retrospective Theses and Dissertations by an authorized administrator of Iowa State University Digital Repository. For more information, please contact [digirep@iastate.edu](mailto:digirep@iastate.edu).

6

93

34969

U·M·I

MICROFILMED 1993

## **INFORMATION TO USERS**

**This manuscript has been reproduced from the microfilm master. UMI films the text directly from the original or copy submitted. Thus, some thesis and dissertation copies are in typewriter face, while others may be from any type of computer printer.**

**The quality of this reproduction is dependent upon the quality of the copy submitted. Broken or indistinct print, colored or poor quality illustrations and photographs, print bleedthrough, substandard margins, and improper alignment can adversely affect reproduction.**

**In the unlikely event that the author did not send UMI a complete manuscript and there are missing pages, these will be noted. Also, if unauthorized copyright material had to be removed, a note will indicate the deletion.**

**Oversize materials (e.g., maps, drawings, charts) are reproduced by sectioning the original, beginning at the upper left-hand corner and continuing from left to right in equal sections with small overlaps. Each original is also photographed in one exposure and is included in reduced form at the back of the book.**

**Photographs included in the original manuscript have been reproduced xerographically in this copy. Higher quality 6" x 9" black and white photographic prints are available for any photographs or illustrations appearing in this copy for an additional charge. Contact UMI directly to order.**

# **U·M·I**

University Microfilms International  
A Bell & Howell Information Company  
300 North Zeeb Road, Ann Arbor, MI 48106-1346 USA  
313/761-4700 800/521-0600



**Order Number 9334969**

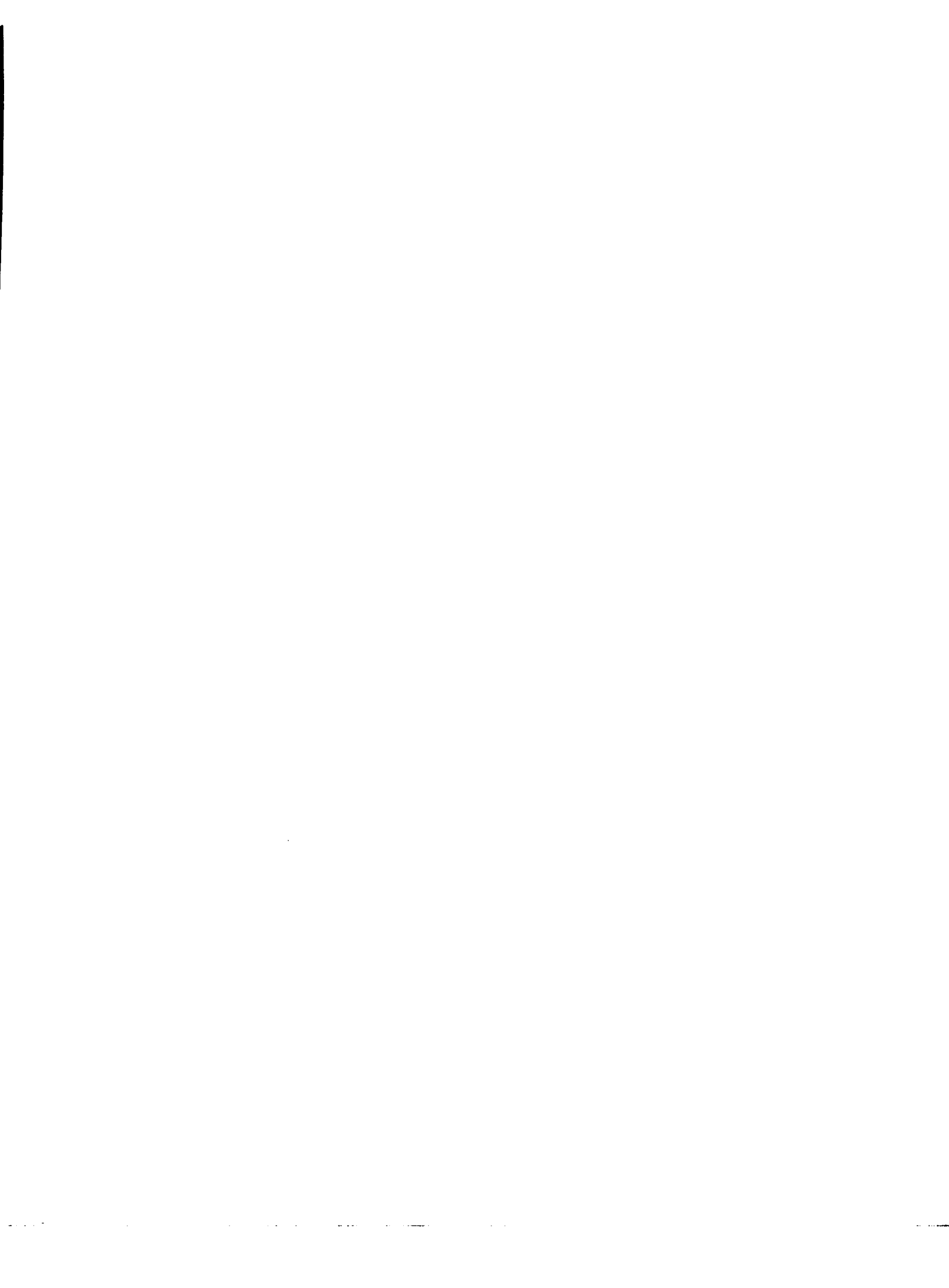
**Determining char burning and sulfur sorption rates from  
dynamic analysis of CO<sub>2</sub> and SO<sub>2</sub> profiles**

**Christofides, Nearchos J., Ph.D.**

**Iowa State University, 1993**

**Copyright ©1993 by Christofides, Nearchos J. All rights reserved.**

**U·M·I**  
300 N. Zeeb Rd.  
Ann Arbor, MI 48106



**Determining char burning and sulfur sorption rates from dynamic  
analysis of CO<sub>2</sub> and SO<sub>2</sub> profiles**

by

**Nearchos J. Christofides**

**A Dissertation Submitted to the  
Graduate Faculty in Partial Fulfilment of the  
Requirements for the Degree of  
DOCTOR OF PHILOSOPHY**

**Department: Mechanical Engineering  
Major: Mechanical Engineering**

**Approved:**

Signature was redacted for privacy.

**In Charge of the Major Work**

Signature was redacted for privacy.

**For the Major Department**

Signature was redacted for privacy.

**For the Graduate College**

**Iowa State University  
Ames, Iowa**

**1993**

**Copyright © Nearchos J. Christofides, 1993. All rights reserved.**

## **DEDICATION**

**Dreams are made for those who make them real**

**Thank you LORD for giving me the strength to face my fears and achieve my goals.**

**Once, a great poet said:**

**" 'Tis not the goal that breeds wisdom,  
but the road you take to achieve your goal"**

**The poet was Kavafis, the Poem "Ithaka". The poem was a spin-off Ulysses trip to Ithaka. Ulysses followed an adventurous route to his homeland, his ultimate goal. He faced danger, he faced death. He learned to face his fears and fight his foes. When he reached his goal, he did not celebrate for being there, but for learning so much on his way to his homeworld.**

**So, let us think back to the journey to our ultimate goal. And let us think of what we have learned, the experience, the success, the failure, the good moments, the bad moments, the people we met. Life itself has an ultimate goal: To become one with the Lord. Let us not forget the One Who gave us life. Let us live to make ourselves better, not in wealth, but in faith and good deeds. The road you follow to your ultimate goal will determine your reward.**

**I dedicate this work to my parents who, despite all the obstacles they faced, stood by my side during these long years and helped me in my moments of difficulty. To them, who brought me in this world and loved me beyond themselves. May the rest of their life be as fruitful and happy.**

**TABLE OF CONTENTS**

<b>1. INTRODUCTION</b>	1
<b>2. BACKGROUND</b>	3
2.1 Coal combustion	3
2.1.1 Devolatilization	3
2.1.2 Char burnout	6
2.2 Sulfur release from coal and sulfur sorption	9
2.2.1 Mechanism of sulfur release from coal	9
2.2.2 Limestones	9
2.2.3 Limiting steps in limestone sulfation rate and utilization	10
2.2.4 Dependence of limestone utilization on temperature	12
2.2.5 The effect substoichiometric conditions on sulfation	13
<b>3. MODELS FOR COAL COMBUSTION</b>	16
3.1 Coal combustion	16
3.1.1 Devolatilization relationships	18
3.1.2 Char combustion	19
<b>4. MODELS FOR CALCINATION AND SULFATION</b>	23
4.1 A combined calcination and sulfation model	23
4.1.1 Calcination	23
4.1.2 Sulfation	26
4.3 Model results	30
4.4 Model simplification	36
4.4.1 Calcination	36
4.4.2 Sulfation	38
<b>5. EXPERIMENTAL APPARATUS</b>	48
5.1 Combustor	48
5.2 Fuel and sorbent feeding systems.	48
5.3 Gas sampling system	49
5.4 Data acquisition system	51
<b>6. MATERIALS AND METHODS</b>	52

6.1 Fuels and sorbents	52
6.2 Methods and Techniques	52
6.2.1 Coal and char batch tests	52
6.2.2 Limestone batch tests	52
6.3 Methodology for estimating characteristic devolatilization and char burnout times	55
6.3.1 Devolatilization time constants	54
6.3.2 Char burnout time constants	54
6.4 Methodology for estimating time constants for calcination and sulfation	56
<b>7. RESULTS AND DISCUSSION FOR COAL BATCH TESTS</b>	<b>60</b>
7.1 Devolatilization	60
7.2 Char burnout	63
<b>8. RESULTS AND DISCUSSION FOR SULFUR SORPTION</b>	<b>70</b>
8.1 Investigating the effect of inlet SO <sub>2</sub> conditions	70
8.1.1 Extents of calcination and sulfation	70
8.1.2 Characteristic times for calcination and sulfation	72
8.2 The effect of sample mass	73
8.2.1 Extents of calcination and sulfation	73
8.2.2 Characteristic times for calcination and sulfation	74
8.3 Effect of bed temperature	75
8.3.1 Extents of calcination and sulfation	75
8.3.2 Activation energies	77
8.4 Effect of particle size	81
8.4.1 Extents of calcination and sulfation	81
8.4.2 Time constants for calcination and sulfation	83
<b>9. CONCLUSION</b>	<b>90</b>
9.1 Coal combustion	90
9.2 Limestone calcination	91
9.3 Sulfation kinetics	91
9.4 Suggestions for future tests	94
<b>BIBLIOGRAPHY</b>	<b>95</b>
<b>APPENDIX A. INTRAPARTICLE DIFFUSION KINETICS</b>	<b>98</b>

<b>APPENDIX B. PARAMETERS USED IN CALCINATION/SULFATION MODEL</b>	<b>104</b>
<b>APPENDIX C. CALIBRATION OF INSTRUMENTS AND MEASUREMENT ACCURACY</b>	<b>106</b>
<b>APPENDIX D. PROGRAM CODE</b>	<b>108</b>

## NOMENCLATURE

$a$	coefficient in devolatilization rate power law (s)
$a_c$	total internal area of calcined stone per bed volume ( $m^2/m^3$ )
$a_o$	factor in char burnout rate constant power law (m/s)
$a_p$	external limestone particle area per bed volume ( $m^2/m^3$ )
$a_r$	total uncalcined core area per bed volume ( $m^2/m^3$ )
$A_i$	pre-exponential factor for devolatilization of individual species (1/s)
$A_v$	pre-exponential factor (1/s)
$A_b$	bed area ( $m^2$ )
$C_a$	concentration of species A at reaction site ( $mol/m^3$ )
$\hat{C}_a$	dimensionless concentration of species A
$C_{as}$	concentration of species A at particle surface ( $mol/m^3$ )
$[CO_2]_A$	concentration of $CO_2$ at analyzer ( $mol/m^3$ )
$[CO_2]_c$	concentration of $CO_2$ at surface of uncalcined core ( $mol/m^3$ )
$[CO_2]_f$	$N(g_o + k d_i^2 [O_2]_e) / Q$
$[CO_2]_s$	concentration of $CO_2$ at the surface of limestone particle ( $mol/m^3$ )
$[CO_2]_i$	$N k d_i^2 [O_2]_e / Q$ for char coal combustion, or concentration of $CO_2$ at bed inlet for calcination ( $mol/m^3$ )
$[CO_2]_o$	initial concentration of $CO_2$ in bed ( $mol/m^3$ )
$[CO_2]_R$	concentration of $CO_2$ exiting the reactor ( $mol/m^3$ )
$d$	coal particle diameter (m)
$d_i$	initial coal particle diameter (m)
$d_p$	limestone particle diameter (m)

$D_a$	general bulk diffusion coefficient of species $a$ ( $\text{m}^2/\text{s}$ )
$D_b$	bed diameter (m)
$D_e$	intraparticle diffusion coefficient ( $\text{m}^2/\text{s}$ )
$D_{ec}$	effective $\text{CO}_2$ pore diffusion coefficient ( $\text{m}^2/\text{s}$ )
$D_{es}$	effective $\text{SO}_2$ pore diffusion coefficient ( $\text{m}^2/\text{s}$ )
$D_{eso}$	initial effective $\text{SO}_2$ pore diffusion coefficient ( $\text{m}^2/\text{s}$ )
$D_K$	Knudsen diffusivity ( $\text{m}^2/\text{s}$ )
$D_m$	diffusivity of oxygen to the coal particle ( $\text{m}^2/\text{s}$ )
$D_p$	general pore diffusion coefficient ( $\text{m}^2/\text{s}$ )
$D_{pl}$	product layer diffusivity of $\text{SO}_2$ ( $\text{m}^2/\text{s}$ )
$D_{si}$	pore diffusion diffusion coefficient for sintering ( $\text{m}^2/\text{s}$ )
$D_{so}$	initial pore diffusion diffusion coefficient for sintering ( $\text{m}^2/\text{s}$ )
$D_{AB}$	binary diffusion coefficient of A in B ( $\text{m}^2/\text{s}$ )
$E_a$	apparent activation energy for the combustion of char (cal/mol)
$E_{ap}$	activation energy associated with pore plugging (cal/mol)
$E_{as}$	activation energy associated with sintering (cal/mol)
$E_i$	activation energy for volatiles release for individual species $i$ (cal/mol)
$E_v$	overall activation energy for volatiles release (cal/mol)
$f_c$	fractional conversion of limestone
$g_o$	rate of production of $\text{CO}_2$ from combustion of volatiles (mol/s/particle)
$h_c$	mass transfer coefficient of $\text{CO}_2$ from film to bed during calcination (m/s)
$h_s$	mass transfer coefficient of $\text{SO}_2$ from bed to film during sulfation (m/s)
$k$	overall reaction coefficient for char burnout (m/s)

$k_1$	$\left( \frac{t_{pl}}{\eta_s D_{pl}} + \frac{1}{k_s} \right)^{-1}$ (m/s)
$k_2$	$\frac{V_b/Q}{1/(k_1 a_c) + 1/(h_s a_p)}$
$k_3$	$\eta_s k_s \rho_{ba} S_g V_b/Q$
$k_4$	$\frac{\eta_s D_{pl} \rho_{ba} S_g V_b}{t_{pl} Q}$
$k_5$	$\frac{3k_s m_a}{r_p Q} \sqrt{\frac{S_g D_{eso} t_{pl}}{\rho_a D_{pl}}}$
$k_c$	specific reaction constant for reverse calcination ( $\text{atm}^{-1} \text{s}^{-1}$ )
$k_s$	sulfation reaction constant (m/s)
$k_o$	surface reaction rate constant for char burnout (m/s)
$k_v$	general intrinsic reaction rate constant (1/s)
$L$	bed depth (m)
$m$	mass of carbon in particle(g)
$m_{coal}$	mass of coal batched in the fluidized bed (g)
$m_i$	initial mass of carbon in char particle (g)
$m_l$	mass of limestone in bed (g)
$m_L$	initial mass of limestone batched in the bed (g)
$M$	molecular weight of diffusing species (g/mol)
$M_A$	molecular weight of CaO (g/mol)
$M_L$	molecular weight of CaCO <sub>3</sub> (g/mol)
$M_c$	molecular weight of carbon (g/mol)
$M_s$	molecular weight of SO <sub>2</sub> (g/mol)
$n$	exponent in char burnout time power law

$N$	number of coal or limestone particles in bed
$[O_2]_e$	oxygen concentration in emulsion phase of fluidized bed ( $\text{mol/m}^3$ )
$[O_2]_i$	oxygen concentration at fluidized bed inlet ( $\text{mol/m}^3$ )
$Q$	volumetric flow rate exiting the combustor ( $\text{m}^3/\text{s}$ )
$r_c$	radius of uncalcined $\text{CaCO}_3$ core (m)
$r_g$	radius of CaO grain (m)
$r_{gc}$	radius of unreacted CaO grain core (m)
$r_p$	initial radius of $\text{CaCO}_3$ particle (m)
$r_s$	sulfation rate ( $\text{mol/m}^3/\text{s}$ )
$R$	limestone particle radius (m)
$R_u$	universal gas constant ( $\text{cal/mol}^\circ\text{C}$ )
$\hat{R}$	dimensionless particle radius
$S_g$	B.E.T. area of calcined stone ( $\text{m}^2/\text{g}$ )
$Sh$	Sherwood number
$[SO_2]_c$	concentration of $\text{SO}_2$ at reaction site ( $\text{mol/m}^3$ )
$[SO_2]_i$	concentration of $\text{SO}_2$ at bed inlet ( $\text{mol/m}^3$ )
$[SO_2]_o$	initial concentration of $\text{SO}_2$ in the reactor ( $\text{mol/m}^3$ )
$[SO_2]_R$	concentration of $\text{SO}_2$ exiting the reactor ( $\text{mol/m}^3$ )
$[SO_2]_s$	concentration of $\text{SO}_2$ at surface of limestone particle ( $\text{mol/m}^3$ )
$t$	time (s)
$t_c$	char burnout time (s)
$t_o$	initial time associated with the instrument lag response (s)
$t_{pl}$	product layer thickness (m)
$t_{si}$	induction time for sintering (m)
$t_v$	total devolatilization time (s)

$T$	temperature (K)
$u$	superficial bed velocity (m/s)
$u_o$	minimum fluidization velocity (m/s)
$V$	volatiles yield (%)
$V^*$	maximum volatiles yield (%)
$V_b$	bed volume (m <sup>3</sup> )
$y_c$	mass fraction of CaCO <sub>3</sub> in limestone
$X$	cross flow factor

### *Greek Symbols*

$\epsilon_p$	particle void
$\eta$	effectiveness factor
$\eta_s$	effectiveness factor for sulfation
$\zeta$	tortuosity factor
$\nu$	exponent in devolatilization rate power law
$\xi$	dimensionless bed depth
$\rho_a$	CaO particle density (g/m <sup>3</sup> )
$\rho_{ba}$	bulk density of CaO in bed (g/m <sup>3</sup> )
$\rho_L$	particle density of CaCO <sub>3</sub> (g/m <sup>3</sup> )
$\rho_c$	density of char particle (g/m <sup>3</sup> )
$\rho_g$	CaO grain density (g/m <sup>3</sup> )
$\rho_L$	particle density of limestone (g/m <sup>3</sup> )
$\tau_{bm}$	characteristic time for bed kinetics limited sulfation (s)
$\tau_c$	characteristic time for char burnout or limestone calcination (s)
$\tau_{ch}$	time constant for chemistry rate limited sulfation (s)

$\tau_i$	characteristic interphase transport time of oxygen (s)
$\tau_I$	characteristic time associated with instrumentation lag (s)
$\tau_v$	time constant for volatiles release (s)
$\tau_p$	time constant for sulfation with pore plugging (s)
$\tau_p$	initial time constant for sulfation with pore plugging (s)
$\tau_{pl}$	time constant for product layer diffusion limited sulfation (s)
$\tau_s$	time constant for sulfur sorption (s)
$\tau_{si}$	time constant associated with sintering (s)
$\tau_{so}$	initial time constant associated with sintering (s)
$\phi_s$	Thiele modulus for sulfation
$\phi_{s1}$	Thiele modulus for a general first order reaction inside a spherical particle
$\Omega$	$u - (u - u_o) e^{-X}$ (m/s)

## ACKNOWLEDGMENTS

My thanks to Dr. Robert Brown for his advice and guidance during the progress of my research. I would also like to thank Dr. Gerald Colver, Dr. Howard Shapiro, Dr. Richard Seagrave, Dr. Terry King, and Dr. L. Doraiswamy for serving on my graduate committee. I also would like to thank Mr. Brad Kohlmeyer who patiently helped me in preparing the fuel and sorbent used in my experiments.

This work was initiated with Iowa State University consortium grant from the Electric Power Research Center, the Breen Fund, and the Iowa State Mining and Mineral Resources Research Institute. Additional support has been provided by the U. S. Department of Energy through Cooperative Agreement No. DE-FC21-91MC28081.

## 1. INTRODUCTION

A new methodology for estimating coal burning characteristics and sorbent utilization in fluidized bed reactors has been developed and validated. The method aims at determining time constants for devolatilization and char burnout from carbon dioxide ( $\text{CO}_2$ ) profiles and time constants for sulfur sorption from sulfur dioxide profiles. These time constants can be directly related to fundamental burning properties of the coal and sulfation kinetics of the sorbent, respectively.

Previous research in coal combustion [1,2,3] used visual methods for estimating coal devolatilization and char burnout times. Coal devolatilization times were in most cases obtained by observing and timing the extinction of volatile flames from suspended burning particles [1] or coal particles burning in jets [2]. These methods tend to underestimate devolatilization times partly because the extinction of volatile flames may be followed by a brief release of unburned gas from the particles [1]. Char burnout times were also estimated by watching and timing burning char particles in jets [2] or in small quartz tube reactors [3]. Visual methods may underestimate char burnout times because of an ash layer formed around the burning particle that prevents direct observation of unburned material [2]. In addition, these methods are greatly influenced by systematic errors by the observer. Techniques for the estimation of sulfur sorption rates have been based on the analysis of material retrieved from the reactor or on thermogravimetric techniques [4]. All existing methods for estimating coal burning and sulfur sorption rates are intrusive to the reaction process, involve the use of special equipment, and are not suited for direct use in large-scale combustors.

The methodology developed in this work involves the batching of small samples of coal or sorbent in a reactor heated with propane or coal. Devolatilization and char burnout time constants are obtained from analysis of  $\text{CO}_2$  perturbations from background level, which are imposed by batching coal samples in a bed heated with propane. Similarly, sulfation time constants are obtained by analyzing  $\text{SO}_2$  perturbations from the background level, which, in

this case, are imposed by batching limestone in a bed heated with propane with direct SO<sub>2</sub> injection at the air inlet to the bed. Variations of coal devolatilization times and char burnout times with particle size and temperature are examined. The variations of sulfur sorption times on temperature and limestone particle size are also investigated.

Unlike existing methods, this approach is non-intrusive and utilizes standard power plant equipment, thus making it applicable to large-scale boilers. Continuous monitoring of coal combustion and sorbent characteristics, validation of the combustion characteristics of new coals and sorbent utilization are a few of the applications of this new dynamic approach to measuring coal burning rates and characterize sorbent reactivity.

## **2. BACKGROUND**

### **2.1 Coal combustion**

Coal is a heterogeneous mixture of organic and inorganic matter [5,6]. The organic matter in coal consists primarily of carbon, hydrogen, oxygen, nitrogen, and sulfur. Coal may also contain substantial amounts of inorganic matter like sulfate salts of calcium and potassium, pyrites, and aluminum oxide, which are collectively referred to as ash. Organic matter in coal is arranged either as free carbon or as complex organic matter consisting of polycyclic clusters.

Coal combustion proceeds in two stages. Stage one involves the rapid release of volatile matter from the coal particle which starts at about 400 °C. Moisture in the coal can be perceived as part of the volatiles, but it usually evolves long before the devolatilization temperature is reached. The second stage is the combustion of the carbonaceous residue to ash (char burnout) which commences at temperatures above 600-700 °C.

Devolatilization and char burnout are strong functions of particle size [1,2,5-7]. Although coal rank does not affect devolatilization times [6], it influences product composition and yield as well as morphology and combustion characteristics of the residual char [5-7].

#### **2.1.1 Devolatilization**

Volatile matter in coal is found as polycyclic aromatic clusters the structure of which varies greatly from coal to coal. At temperatures in excess of 400 °C the cross bonds in these large molecules rupture, releasing a mixture of light hydrocarbon base compounds (methane, benzene, toluene, thiols, thiamines etc.), CO<sub>2</sub>, CO, H<sub>2</sub>, H<sub>2</sub>S, SO<sub>2</sub>, water, and tar (heavy hydrocarbons). Given [7] describes the release of volatile matter from coal in four steps:

1. Low temperature loss of hydroxyl groups (400-500 °C).

2. Dehydrogenation of hydroaromatic structures.
3. Scission of the heavy molecules at double bond bridges.
4. Rupture of alicyclic compounds.

Under oxidizing conditions, the hydrocarbons will burn readily to produce primarily  $\text{CO}_2$ ,  $\text{CO}$ ,  $\text{H}_2\text{O}$ , and  $\text{SO}_2$ . The ultimate volatiles yield is more a function of the particle's final temperature than the heating rate [8]. Pressure and particle size affect product yield and composition. Higher pressures and larger particle sizes increase the residence times of volatiles in the coal particle, thus allowing secondary reactions (tar cracking, oxygenation of hydrocarbons, etc.) to take place.

A number of researchers [1,5,9] have suggested a first order model to describe devolatilization yield

$$\frac{dV}{dt} = \frac{V^* - V}{\tau_v}, \quad (2.1)$$

where the characteristic time for devolatilization,  $\tau_v$ , is assumed to follow the Arrhenius law

$$\frac{1}{\tau_v} = A_v \exp\left(-\frac{E_v}{R_u T}\right). \quad (2.2)$$

The first order devolatilization law is easy to use but has several limitations. As Howard [8] states, pyrolysis is the evolution of a group of species and cannot be approximated with a single activation energy since each species may evolve independently of other species at a rate with its own characteristic activation energy. A more involved model is derived from the assumption that pyrolysis consists of multiple parallel first-order reactions that do not interact. The characteristic times for each species are thus given by the law

$$\left(\frac{1}{\tau_v}\right)_i = A \exp\left(-\frac{E_i}{RT}\right), \quad (2.3)$$

where the subscript  $i$  denotes each of the different species involved. The pre-exponential factor,  $A_i$ , is taken to be the same for all processes. The activation energies are then assumed to follow a Gaussian type distribution, which results in a total volatiles yield [8]

$$V_i^* - V_i = V_i^* \exp \left( -A_i \exp \left( -\frac{E_i}{R_u T} \right) \right). \quad (2.4)$$

This more complicated approach yields somewhat better results than the first order model, but it can again be simplified, as demonstrated by Anthony et al. [10], to a simple first-order model with an activation energy  $E_v$ , which is smaller than the smallest  $E_i$ . For the purpose of this research a single, first-order model for volatiles release is assumed.

Many researchers estimate the total devolatilization time,  $t_v$ , by noting the time at which the volatile flame around the particle is extinguished [1,11,12]. Others measure the time required to evolve 95 wt% volatiles from a coal sample [12]. The devolatilization time is strongly dependent on initial particle size [1,6,8] but is not a strong function of coal rank [6].

Commonly, the volatiles release time,  $t_v$ , is expressed as a power of the initial particle diameter [1,2,11]

$$t_v = a d_i^v. \quad (2.5)$$

Essenhigh [1] determined volatile release times by observing the extinction of flames from single coal particles. For particles in the range of 0.3 to 5 mm,  $t_v$  was found to be proportional to the square of the particle diameter with the factor  $a$  equal to  $0.9 \text{ s/mm}^2$  [1]. Ragland and Weiss [2] also observed the extinction of flames from coal particles and estimated both  $a$  and  $v$  to be 1.5 for particles 2 to 12 mm in diameter. Pillai [11], on the other hand, found  $v$  to vary from 0.3 to 1.8 depending on coal type for coal particles smaller than 8 mm.

Upon integration, Eq. 2.1 yields the exponential law

$$V = V^* \left[ 1 - \exp\left(-\frac{t}{\tau_v}\right) \right]. \quad (2.6)$$

Since Eq. 2.6 suggests that 95% of the volatiles are released within three characteristic time constants, the devolatilization time can be approximated as

$$t_v = 3 \tau_v. \quad (2.7)$$

Devolatilization is a very important process in the combustion of coal. Essenhigh [1] and Ragland and Weiss [2] observed that coal particles may fragment during devolatilization due to the vigorous volatile release. These observations were also confirmed by Chirone et al. [13] and Chirone and Massimilla [14] who observed that primary fragmentation during volatiles release significantly reduces the burnout time of the subsequent char. The swelling of the particle during devolatilization also determines the strength of the remaining char matrix. Coal plasticity is determined by rank. Bituminous coals are known to be the most plastic and swell considerably during devolatilization [6]. The swelling during devolatilization produces, porous, frail char matrices that, besides fragmenting during devolatilization [1,2,13,14], break up quickly during the subsequent char combustion [5,6,8]. Low free-swelling index coals, like lignites and sub-bituminous coals, do not swell much during devolatilization and their char is far less fragile [6,8] although primary fragmentation may occur due to pressure build-up in the particle. Knowing the devolatilization times of coals is therefore extremely important in understanding the combustion mechanism of char.

### 2.1.2 Char burnout

Char burnout is a relatively slow process compared to devolatilization. The time for char burnout is a strong function of particle size [1,3,15,16]. Avedesian and Davidson [3] were among the first to investigate char burnout in fluidized beds. They developed a two film model to explain why the burnout time,  $t_c$ , for large coal particles was proportional to the square of the particle diameter in their experiments. Later, Ross and Davidson [15] improved

this model to include the effects of chemical reaction on burnout time. The revised model assumes that all reactions are fast with the exception of the surface reaction  $CO_2 + C \rightarrow 2CO$ . The latter reaction is at a finite rate so that there is a finite surface concentration of  $CO_2$  at the particle surface as shown in Fig. 2.1 The two zone model in Fig. 2.1 is described by Eq. 2.8 [15]

$$t_c = \frac{m_i}{12[O_2]_i A_b [u - (u - u_o) e^{-X}]} + \frac{\rho_c d_i}{24 k_o [O_2]_i} + \frac{\rho_c d_i^2}{48 Sh D_m [O_2]_i} \quad (2.8)$$

The first term on the right side of Eq. 2.8, which will be referred to as  $t_p$ , is the time associated with the interphase transport of oxygen between bubble and emulsion phases of the fluidized bed. The second term is associated with the surface reaction of oxygen with char, and the third term describes the mass transfer of oxygen through the film surrounding the particle.

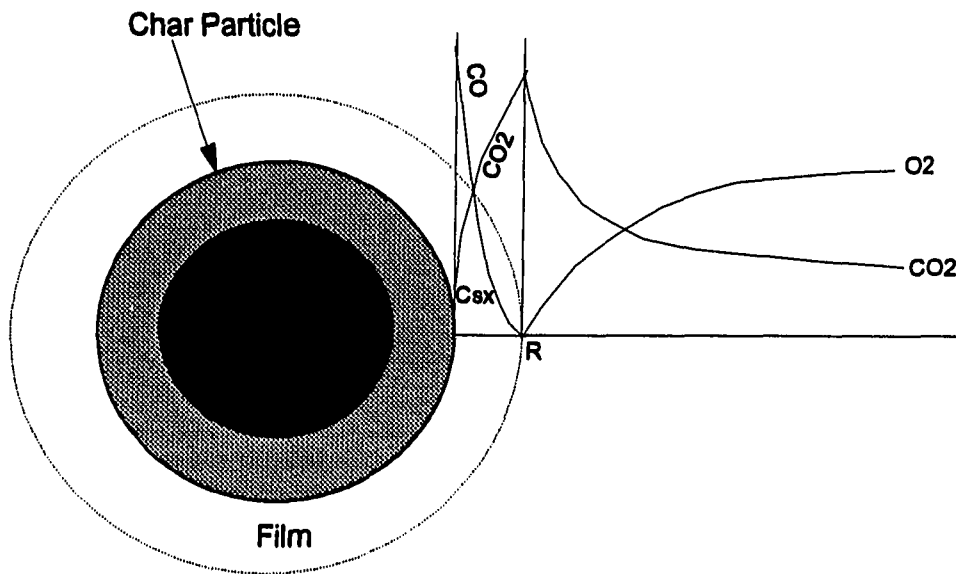


Figure 2.1: Two zone model for the combustion of char

For particles larger than 1mm [3], the controlling mechanism is mass transfer of oxygen through the film surrounding the particle, thus the time for the char burnout is proportional to the square of  $d_i$ . Combustion of particles smaller than 100  $\mu\text{m}$  is controlled by chemical reaction and the burnout time,  $t_c$ , is proportional to  $d_i$  [3].

Ragland and Weiss [2] showed that for coal particles 2-12 mm diameter burned in a gas jet, the burnout time dependence on diameter takes the form

$$t_c = \frac{0.56d_i^2 + 6.4}{X} \quad (2.9)$$

Equation 2.9 assumes that diffusion is rate limiting for large coal particles. A "d-squared" law for  $t_c$  was also observed by Essenhigh [1] for particles between 0.3 and 5 mm under diffusion limited combustion.

On the other hand, Basu [16] observed the burning rates of 3-10mm coal particles in fluidized beds to follow a power law of the order

$$\frac{dm}{dt} \propto d_i^p \quad (2.10)$$

where the exponent  $p$  is expected to be 1 for diffusion limited combustion and 2 for chemical kinetics control. Basu [16] found  $p$  to be between 1.22 and 1.55 which was interpreted to be an indication that the rates of film diffusion and chemical kinetics are comparable during the combustion of char.

Several researchers [3,15-17] measured char burnout times in fluidized beds by observing and timing coal particles as they burned. Burnout times for large coal particles are known to be substantially underestimated by the d-squared law if particles fragment during devolatilization or char combustion [1,2,13,14].

## **2.2 Sulfur release from coal and sulfur sorption**

### **2.2.1 Mechanism of sulfur release from coal**

The sulfur in coal is found in the form of organic compounds ( $\text{H}_2\text{S}$ , thiols, etc.), as pyritic compounds denoted by  $\text{FeS}_x$ , and a variety of other metal silfides (e.g.  $\text{CaS}$ ) [18,19]. The release of sulfur takes place in two stages. Moffat [19] showed that most of the sulfur in coal is found as organic compounds that are released during devolatilization. The devolatilized sulfur compounds are immediately oxidized to  $\text{SO}_2$ . Additional smaller quantities of sulfur are released at the end of the char burnout via oxidation inorganic sulfur compounds [19]. Figure 2.2 illustrates, qualitatively, the release of  $\text{SO}_2$  from coal as reported by Moffat [19]. The initial spike in the  $\text{SO}_2$  concentration appears during release and oxidation of volatile matter from coal and is followed by a much smaller transience at a later time, which is the product of oxidation of pyritic sulfur found in the char residue [19].

Controlling the amount of  $\text{SO}_2$  released to the atmosphere during the combustion of coal has long been a major concern. In conventional coal fired boilers (stoker and pulverized coal) the sorption of  $\text{SO}_2$  is part of the exhaust gas treatment and requires expensive equipment. Fluidized beds offer the ideal environment for in-situ capture of  $\text{SO}_2$  by limestone, which is directly added to the bed either as part of the bed material or as an additive to the fuel in the case of coal-water-mixtures [20].

### **2.2.2 Limestones**

Limestone and dolomites are the cheapest sulfur sorbents for use in fluidized bed boilers. Limestone consists primarily of calcium carbonate,  $\text{CaCO}_3$ , (typically 85-98 wt%) and a variety of trace minerals. Dolomites contain comparable amounts of  $\text{CaCO}_3$  and magnesium carbonate ( $\text{MgCO}_3$ ). Limestones and dolomites calcine above  $550^\circ\text{C}$  to produce  $\text{CaO}$  and a mixture of  $\text{CaO}$  and  $\text{MgO}$ , respectively

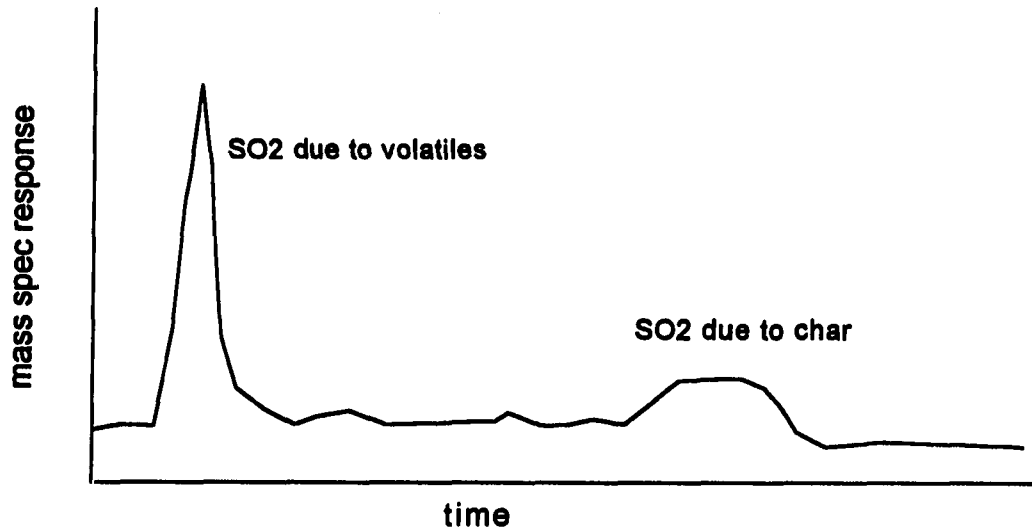
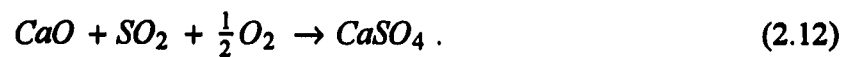


Figure 2.2: Mechanism of sulfur release from coal (19).



The release of  $\text{CO}_2$  from limestone leaves a porous  $\text{CaO}$  matrix. In the presence of oxygen,  $\text{CaO}$  reacts readily with  $\text{SO}_2$  to produce calcium sulfate ( $\text{CaSO}_4$ )



### 2.2.3 Limiting steps in limestone sulfation rate and utilization

Full utilization of  $\text{CaO}$  (and limestone) is not always possible because reactions may be slowed down or halted by the build-up of layers of  $\text{CaSO}_4$  [4,21,22], which limit access to active sites. Mulligan et al. [4], investigated the controlling steps in the sulfation of  $\text{CaO}$  by examining the variation of the weight gained by calcined limestone over time in a thermobalance for particle sizes between  $150 \mu\text{m}$  and  $212 \mu\text{m}$ . They [4] observed that, initially, sulfation is

controlled by the rate of chemical reaction. For longer periods, they [4] observed that the reaction rate is controlled by the rate of diffusion of reacting species through the  $\text{CaSO}_4$  product layer. Mulligan et al. [4] proposed that the rather high activation energies observed in their experiments (53 kcal/mol) were indicative of diffusion of ionic species ( $\text{Ca}^{2+}$  and  $\text{O}^{2-}$ ) through the product ( $\text{CaSO}_4$ ) layer. Borgwardt et al. [22] also investigated the effect of product layer diffusion on the rate of limestone sulfation for 5  $\mu\text{m}$  sorbent particles. Contrary to Mulligan et al. [4], they [22] observed that product layer diffusion of gaseous reactants limited the rate of sulfation. The activation energy estimated for this process was 33 kcal/mol [22].

On the other hand, Simmons et al. [21] suggested that the rate and degree of sulfation of CaO are limited by pore plugging, which restricts mass transfer to active sites much faster than product layer diffusion. The latter researchers [21] modeled the CaO pore structure as a tree-like network having large trunks, which represent the large pores near the surface and smaller branches, which represent the small pores. Simmons et al. [21] showed that product deposits quickly fill pores of all sizes resulting in total loss of porosity and, therefore, in complete cessation of the sulfation reaction.

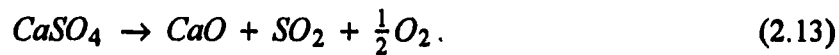
All previous researchers [4,21,22] used CaO (calcined limestone) in their experiments. Starting with uncalcined limestone may change the limiting steps in the sulfation of limestone as observed by Haji-Sulaiman and Scaroni [23], who observed that the degree of calcination of the sorbent limits limestone utilization. The degree of calcination of limestone determines the reactivity of the sorbent since CaO is more reactive than  $\text{CaCO}_3$ . Calcium sulfate deposits on the outer surface of limestone prohibit additional calcination of the sorbent by restricting the escape of  $\text{CO}_2$ . The same researchers [23] showed that the degree of calcination is also limited by the partial pressure of  $\text{CO}_2$  in the reactor. High  $\text{CO}_2$  concentrations further reduce the degree of calcination by increasing the backward reaction (Eq. 2.11) and producing  $\text{CaCO}_3$ . Furthermore, Christofides and Brown [20], who performed XRD scans on coal-water-limestone mixture (CWLM) agglomerates recovered from a fluidized bed, observed little or no CaO and significant amounts of  $\text{CaCO}_3$  and  $\text{CaSO}_4$  in the agglomerates. They [20]

attributed the small concentrations of CaO to the fact that SO<sub>2</sub> reacts with CaO as soon as the latter is formed and the relatively high local CO<sub>2</sub> pressures (produced by char combustion), which considerably slow down the calcination reaction by shifting the equilibrium toward producing more CaCO<sub>3</sub>.

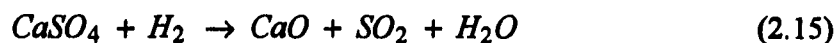
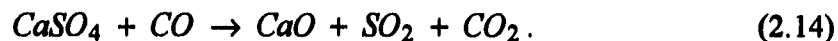
#### 2.2.4 Dependence of limestone utilization on temperature

Sulfur sorption by limestone is temperature dependent. The optimum temperature for maximum sulfur removal lies between 815 and 860 °C [20,18,24]. This optimum temperature is better understood by noting that as temperature is increased, increased calcination improves sorbent porosity. As the optimum temperature is exceeded, SO<sub>2</sub> reacts with CaO before it can diffuse into the core of the sorbent particle and pores become blocked to further sorbent utilization [25].

At temperatures lower than 815 °C, low concentrations of the active CaO result in low sorbent utilization. At temperatures higher than 860 °C the degree of sulfation may be reduced by the decomposition of CaSO<sub>4</sub>



Other factors, like the presence of CO and H<sub>2</sub> at the reaction site, may promote reductive decomposition of CaSO<sub>4</sub> [18] at temperatures higher than the optimum. At temperatures in excess of 1000 °C reduction of CaSO<sub>4</sub> significantly reduces the efficiency of sulfation by regenerating SO<sub>2</sub>



These conditions are highly unlikely in a fluidized bed environment where combustion temperatures are typically around 800 - 900 °C. However reactions 2.14 and 2.15 are very important in the regeneration of limestone sorbent.

### 2.2.5 The effect substoichiometric conditions on sulfation

Under oxygen-lean conditions, sulfur appears in the form of hydrogen sulfide ( $H_2S$ ). The product of the sulfation reaction in this case is calcium sulfide ( $CaS$ ) [24]



Calcium sulfite has substantially lower molar volume compared to  $CaSO_4$  therefore pore plugging is prevented and limestone utilization is significantly increased (see Fig. 2.3). According to Jonke et al. [24] this reaction is favored in coal fired boilers where combustion of coal may reduce local oxygen concentrations to below 50% the stoichiometric concentration, thereby reducing sulfur to  $H_2S$ . Oxygen lean conditions may be present in the emulsion phase of a fluidized bed coal combustor where combustion of coal consumes most of the oxygen. Calcium sulfate, however, is very reactive can be quickly converted to  $CaSO_4$  in a combustion environment where oxygen is 70% of the stoichiometric, thereby reducing sulfur retention due to deposits in the particle pores (see Fig. 2.3).

The processes involved during the calcination and sulfation of limestone are summarized in Fig. 2.4. The schematic includes  $CaSO_4$  decomposition reactions and reactions of  $CaSO_4$  with  $CO$  and  $H_2$ .

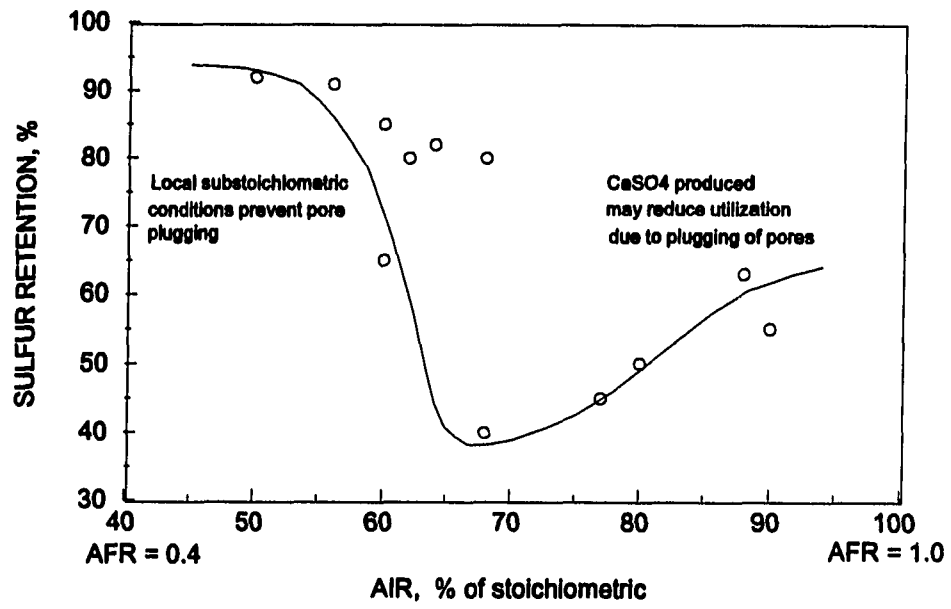


Figure 2.3: Variation of sulfur retention with % stoichiometric air (24)

The air to fuel ratio (AFR) is also shown.

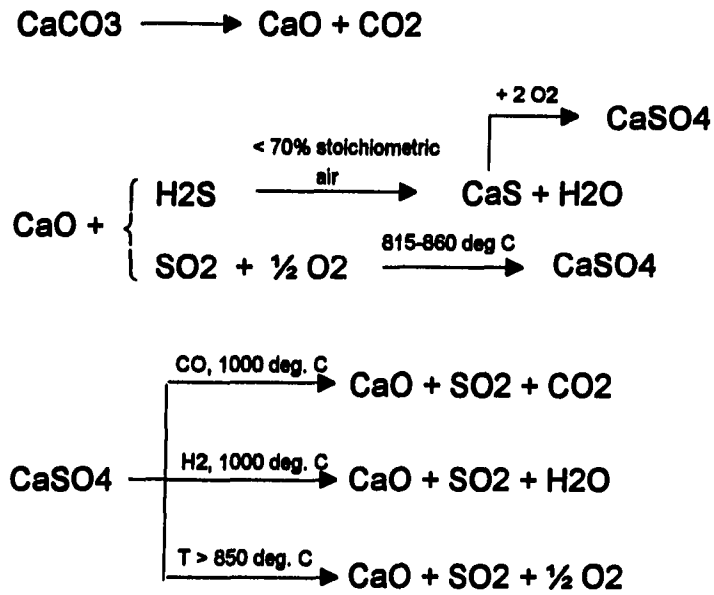


Figure 2.4: Processes involved during calcination and sulfation of limestone and decomposition reactions of  $\text{CaSO}_4$

### 3. MODELS FOR COAL COMBUSTION

The coal combustion model simulates the batching of single-sized coal particles into a fluidized bed heated with propane gas or other fuel. The model predicts CO<sub>2</sub> profiles due to burning of volatiles and char in a fluidized bed.

#### 3.1 Coal combustion

Assuming that the overall combustor is well mixed, the concentration of CO<sub>2</sub> exiting the combustor is given by the overall mass balance on the reactor

$$V_b \frac{d[CO_2]_R}{dt} + Q[CO_2]_R = -\frac{1}{M_c} \left. \frac{dm}{dt} \right|_{devol.} - \frac{1}{M_c} \left. \frac{dm}{dt} \right|_{char}, \quad (3.1)$$

where the first term on the right hand side of Eq. 3.1 is the rate that volatiles are converted to CO<sub>2</sub> and the second term is the rate that the carbon in the residual char is converted to CO<sub>2</sub>.

Since gas phase reactions are very fast, carbon compounds released during devolatilization are assumed to be instantaneously oxidized to CO<sub>2</sub>. Accordingly, the rate of CO<sub>2</sub> formation from volatiles is given by the first-order devolatilization model in Eq. 2.4

$$-\frac{1}{M_c} \left. \frac{dm}{dt} \right|_{devol.} = N g_o \exp\left(-\frac{t}{\tau_v}\right). \quad (3.2)$$

The consumption of char is assumed to primarily occur in the emulsion phase [3] and follow the first-order oxidation model for a shrinking sphere [3]

$$-\frac{1}{M_c} \left. \frac{dm}{dt} \right|_{char} = N d^2 k [O_2]_e, \quad (3.3)$$

where the concentration of oxygen in the emulsion phase,  $[O_2]_e$ , is influenced by the rates of oxygen consumption and the interphase transport of oxygen from bubbles to the emulsion phase. Avedesian and Davidson [3] applied a quasi-steady assumption on oxygen mass balance to obtain the expression for  $[O_2]_e$

$$[O_2]_e = \frac{[O_2]_i}{kN\pi d_b^2 / (A_b \Omega) + 1}, \quad (3.4)$$

where  $[O_2]_i$  is the concentration of oxygen at the bed inlet.

The overall char reaction rate constant,  $k$ , may be a combination of both mass transfer rate and intrinsic chemical kinetics [15]

$$\frac{1}{k} = \frac{1}{k_o} + \frac{d}{ShD_m}. \quad (3.5)$$

This rate constant can be approximated with a simple power law which well describes rate-limiting combustion regimes

$$k = a_o d^{1-n}. \quad (3.6)$$

Although this power law is an oversimplification of the general case of char combustion, it well represents several rate-limiting cases shown in Table 3.1.

Analysis of gas emissions from the combustor must account for the lag time associated with the gas sampling system and gas analyzers. Tests carried out with  $CO_2$  as a tracer gas suggest that a single lag time, which is referred to as the instrumentation lag time,  $\tau_l$ , can describe the composite behavior of the gas sampling and gas analyzer systems. The transient  $CO_2$  signal registered at the gas analyzer,  $[CO_2]_A$ , is described by

Table 3.1: Summary of char burnout regimes

Regime	$n$	$a_n$
Mass transfer limited (fixed Sh)	2	$\alpha D_m$
Mass transfer limited (variable Sh)	3/2	$\beta D_m$
Chemistry limited	1	$k_p$

$$\frac{d[CO_2]_A}{dt} = -\frac{1}{\tau_I} \{ [CO_2]_R - [CO_2]_A \}. \quad (3.7)$$

The lag time  $\tau_I$  should be made very small under which circumstances the analyzer registers the gas concentrations in the bed and the subscript designation on  $CO_2$  can be dropped. However, this condition was not always met in the experiments subsequently described.

### 3.1.1 Devolatilization relationships

Devolatilization can be described by a first-order model with characteristic time  $\tau_v$ . During devolatilization, the char consumption rate is assumed to be very slow compared to the advection of gas through the fluidized bed and the release of volatiles from coal particles. For a batch of coal, the diameter is assumed to remain constant during devolatilization (i.e.  $d = d_i$ ). Furthermore, assuming that quasi-steady condition prevails between  $CO_2$  formed from fast burning volatiles and  $CO_2$  removed by gas advection, Eq. 3.1 becomes

$$Q[CO_2]_R = Ng_o \exp\left(-\frac{t}{\tau_v}\right) + Nd_i^2 k[O_2]_e. \quad (3.8)$$

Dividing by  $Q$  and defining  $[CO_2]_f$  as the almost constant contribution of char combustion to the  $CO_2$  signal during devolatilization, Eq. 3.8 yields:

$$[CO_2]_f = Nd_i^2 k[O_2]_i / Q. \quad (3.9)$$

Also, defining  $[CO_2]_i$  as initial  $CO_2$  concentration at the beginning of devolatilization, Eq. 3.8 yields:

$$[CO_2]_i = \frac{N}{Q} (g_o + kd_i^2 [O_2]_e). \quad (3.10)$$

Combining Eq. 3.9 and Eq. 3.8 and noting that

$$Ng_o = [CO_2]_i - [CO_2]_f, \quad (3.11)$$

the following non-dimensional expression for  $[CO_2]_R$  is obtained

$$\frac{[CO_2]_R - [CO_2]_f}{[CO_2]_i - [CO_2]_f} = \exp\left(-\frac{t}{\tau_v}\right). \quad (3.12)$$

The constants  $[CO_2]_i$  and  $[CO_2]_f$  are estimated from the  $CO_2$  profiles as it will be subsequently explained. Equation 3.12 can be used to estimate the time constant for the release of volatiles,  $\tau_v$ , from the  $CO_2$  profiles for times in the range  $V_b/Q < t < 3\tau_v$ .

In the development of Eq. 3.12, it has been assumed that the combustion of volatiles and char occur simultaneously. Saxena [5] and Ragland and Weiss [2] have suggested that char consumption does not begin until after devolatilization, an idea that assumes oxygen cannot diffuse to the coal particle surface while volatiles are being expelled. If such was the case,  $[CO_2]_f$  would be zero in Eq. 3.12. The experiments in this work investigate whether devolatilization and char combustion occur simultaneously.

### 3.1.2 Char combustion

The consumption of char is an extremely non-linear process. A more complicated analysis is, therefore, required to interpret the char burnout data. For times  $t > 3\tau_v$ , only char

burning substantially contributes to the  $\text{CO}_2$  signal. Applying the quasi-steady assumption to Eq. 3.1 yields

$$[\text{CO}_2]_R = -\frac{1}{M_c} \left. \frac{dm}{dt} \right|_{char.} = \frac{[\text{O}_2]_i}{Q} \left\{ \frac{kN\pi d^2}{kN\pi d_i^2 / (A_b \Omega) + 1} \right\}, \quad (3.13)$$

where  $k$  depends on diameter according to Eq. 3.6. Substituting  $m = N\rho_c \pi d^3 / 6$  in Eq. 3.3 for spherical particles burning as shrinking cores and substituting for  $[\text{O}_2]_e$  from Eq. 3.4 yields

$$-\frac{1}{M_c} \left. \frac{dm}{dt} \right|_{char.} = -\frac{1}{2} \frac{N d^2 \rho_c}{M_c} \frac{d(d)}{dt} = \frac{N\pi d^2 [\text{O}_2]_i}{kN\pi d^2 / (A_b \Omega) + 1}. \quad (3.14)$$

Simplifying Eq. 3.14 and substituting the power law given by Eq. 3.6 for  $k$  yields a differential equation describing the rate of change in particle diameter

$$-\frac{\rho_c}{2M_c} \frac{d(d)}{dt} = \frac{a_o d^{1-n} [\text{O}_2]_i}{a_o d^{1-n} N\pi d^2 / (A_b \Omega) + 1}. \quad (3.15)$$

Using the initial condition  $d = d_i$  at  $t = 0$ , Eq. 3.15 can be integrated to obtain an expression for particle diameter as a function of time

$$\frac{1}{3} \frac{N\pi (d_i^3 - d^3)}{A_b \Omega} + \frac{1}{n} (d_i^n - d^n) = \frac{2M_c a_o [\text{O}_2]_i}{\rho_c} t. \quad (3.16)$$

To estimate the char burnout time  $t_c$ ,  $d$  is set equal to zero at  $t = t_c$  in Eq. 3.16

$$\begin{aligned}
t_c &= \frac{1}{6} \frac{N\pi d_i^3}{A_b \Omega M_c [O_2]_i} + \frac{\rho_c d_i^n}{2 a_o n M_c [O_2]_i} \\
&= \frac{m_i}{A_b \Omega M_c [O_2]_i} + \frac{\rho_c d_i^n}{2 a_o n M_c [O_2]_i}.
\end{aligned} \tag{3.17}$$

Defining the time for interphase mass transport of oxygen between emulsion and bubble phase as  $t_i$

$$t_i \equiv \frac{m_i}{A_b \Omega M_c [O_2]_i} \tag{3.18}$$

Equation 3.17 becomes

$$t_c - t_i = \frac{\rho_c d_i^n}{2 a_o n M_c [O_2]_i} \tag{3.19}$$

In the experiments,  $t_c$  was taken as the time at which the transient  $CO_2$  signal was no longer detectable above the steady state background  $CO_2$  level. Accordingly,  $t_c$  may be significantly underestimated for large, slow burning particles that do not generate strong  $CO_2$  signals in the last stages of char burnout.

For times much shorter than the burnout time, it is convenient to linearize Eq. 3.16 using the Taylor expansion

$$\frac{d}{d_i} = 1 - \frac{2M_c[O_2]_i t / \rho_c}{N\pi d_i^3 / (A_b \Omega) + d_i^n / a_o} = 1 - \frac{t}{\tau_c} = \exp\left(-\frac{t}{\tau_c}\right) \tag{3.20}$$

The characteristic time is defined as

$$\tau_c - \tau_i = \frac{\rho_c d_i^n}{2 a_o M_c [O_2]_i} \tag{3.21}$$

where  $\tau_i$ , the characteristic interphase mass transfer time of  $O_2$  between bubble and emulsion phase and is defined as

$$\tau_i \equiv \frac{3 m_i}{A_b \Omega M_c [O_2]_i} \quad (3.22)$$

The relationship between  $t_c$  and  $\tau_c$  can be found by dividing Eq. 3.19 by Eq. 3.21

$$\frac{t_c - t_i}{\tau_c - \tau_i} = \frac{1}{n}, \quad (3.23)$$

where the value of  $n$  depends on the nature of the rate-limiting mechanism during the combustion of char. Values for the ratio in Eq. 3.23, corresponding to rate limiting regimes, are shown in Table 3.2.

The simple results obtained in Eqs. 3.19 and 3.21 were used to interpret the results obtained in the experiments.

Table 3.2: Rate limiting regimes in the combustion of char

Regime	$(t_c - t_i) / (\tau_c - \tau_i)$	CO <sub>2</sub> profile	Burnout time power law
Mass transfer limited (fixed Sh)	0.5	$(1-at)^{1/2}$	$d_i^{2.0}$
Mass transfer limited (variable Sh)	0.66	$(1-at)$	$d_i^{1.5}$
Chemistry limited	1	$(1-at)^2$	$d_i^{1.0}$

#### 4. MODELS FOR CALCINATION AND SULFATION

The models are developed for limestone batching in a bed heated with propane or coal, but they can be applied for continuous limestone feed conditions with only minor modifications. Mass balances are taken over the entire reactor. Assumptions will be made as the model is developed.

##### 4.1 A combined calcination and sulfation model

The sulfur sorption model assumes that the bed is a well mixed reactor, calcination and sulfation are assumed to occur simultaneously, and gas solid reactions take place only in the emulsion phase. Limestone is assumed to calcine according to the shrinking core model and  $\text{SO}_2$  reacts with CaO grains after it has diffused inside the particle. As calcination proceeds inside the particle, a porous "ash" layer is formed which consists of CaO micrograins. Sulfation within the porous media is assumed to coat the micrograins with a layer of  $\text{CaSO}_4$  through which  $\text{SO}_2$  has to diffuse prior to further sulfation. Particle porosity is assumed to decrease with time as bulky  $\text{CaSO}_4$  deposits plug the pores.

##### 4.1.1 Calcination

The overall mass balance for  $\text{CO}_2$  released during calcination of a batch of limestone depends on the rate of advection of  $\text{CO}_2$  through the bed and the rate at which  $\text{CO}_2$  diffuses from the particle to the bed

$$V_b \frac{d[\text{CO}_2]_R}{dt} = -Q \{ [\text{CO}_2]_R - [\text{CO}_2]_i \} + h_c a_p V_b \{ [\text{CO}_2]_s - [\text{CO}_2]_R \}, \quad (4.1)$$

where  $[CO_2]_R$  is the overall concentration of  $CO_2$  in the bed,  $[CO_2]_i$  is the concentration of  $CO_2$  at the bed inlet,  $[CO_2]_s$  is the  $CO_2$  concentration at the particle's surface, and  $h_c$  is the mass transfer coefficient from the particle to the bed. The quantities  $Q$  and  $V_b$  are the volume flow through the bed and the bed volume, respectively. The parameter  $a_p$  is the total particle external area per  $m^3$  of bed volume and is defined as

$$a_p = \frac{N\pi d_p^2}{V_b}, \quad (4.2)$$

where  $N$  is the number of limestone particles batched,  $d_p$  is the diameter of the limestone particles.

According to the shrinking core model for calcination (Fig. 4.1), as the limestone particle calcines, a porous CaO matrix is formed through which  $CO_2$  has to diffuse. This "ash" layer forms an additional resistance to the expulsion of  $CO_2$  from the unreacted particle core. Consequently, the film concentration of  $CO_2$  depends on the rate at which  $CO_2$  diffuses through the freshly formed pores to the particle surface and the rate at which  $CO_2$  diffuses through the particle film to the bed

$$\frac{d[CO_2]_s}{dt} = h_c a_p \{ [CO_2]_R - [CO_2]_s \} + 4\pi \frac{D_{ec}}{\frac{1}{r_p} - \frac{1}{r_c}} \frac{N}{V_b} \{ [CO_2]_c - [CO_2]_s \}, \quad (4.3)$$

where  $D_{ec}$  is the effective diffusivity of  $CO_2$  through the pores of CaO,  $r_p$  is the initial particle radius,  $r_c$  is the radius of the uncalcined particle core, and  $[CO_2]_c$  is the concentration of  $CO_2$  at the surface of the unreacted core, which is a function of species diffusion through the CaO "ash" and the rate at which  $CO_2$  is formed by calcination

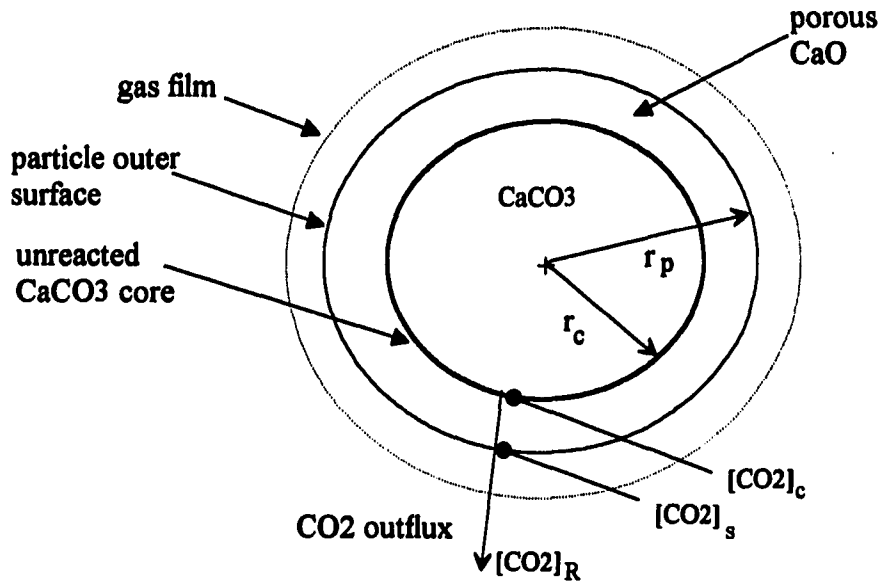


Figure 4.1: Shrinking core calcination model

$$\frac{d[\text{CO}_2]_c}{dt} = 4\pi \frac{D_{ec}}{\frac{1}{r_p} - \frac{1}{r_c}} \frac{N}{V_b} \{[\text{CO}_2]_s - [\text{CO}_2]_c\} + k_c a_r, \quad (4.4)$$

where  $k_c$  is the rate constant for calcination in  $\text{mol/m}^2/\text{s}$  and  $a_r$ , the total external area of the uncalcined core per bed volume, is defined by

$$a_r = 4\pi r_c^2 \frac{N}{V_b}. \quad (4.5)$$

The particle core shrinks because of the loss of  $\text{CO}_2$ , which leaves behind a porous  $\text{CaO}$  matrix. The rate at which the uncalcined core radius shrinks is

$$\frac{dr_c}{dt} = -\frac{k_c M_L}{\rho_L}, \quad (4.6)$$

where  $M_L$  is the molecular weight of limestone and  $\rho_L$  is the density of the core. Finally, the mass of  $\text{CaCO}_3$ ,  $m_p$ , disappears according to

$$\frac{dm_l}{dt} = -k_c M_L a_r V_b \quad (4.7)$$

#### 4.1.2 Sulfation

The concentration of  $\text{SO}_2$  in the bed is also a function of the advection through the bed and the diffusion of species from the bed to the particle's surface

$$V_b \frac{d[\text{SO}_2]_R}{dt} = -Q \{[\text{SO}_2]_R - [\text{SO}_2]_i\} + h_s a_p \{[\text{SO}_2]_s - [\text{SO}_2]_R\}, \quad (4.8)$$

where  $[\text{SO}_2]_R$  is the concentration of  $\text{SO}_2$  in the reactor,  $[\text{SO}_2]_s$  is the concentration of  $\text{SO}_2$  at the particle surface,  $[\text{SO}_2]_i$  is the inlet  $\text{SO}_2$  concentration, and  $h_s$  is the mass transfer coefficient of  $\text{SO}_2$  from the bed to the particle surface.

The calcine is assumed to consist of a porous  $\text{CaO}$  grain structure. Sulfur dioxide diffuses through the particle pores in order to reach the reaction site. Sulfation is assumed to take place at the outer surface of these grains. The deposition of  $\text{CaSO}_4$  on the outer surface of the micrograins creates an additional barrier through which  $\text{SO}_2$  has to diffuse [22]. Sulfate deposits eventually plug the pores and halt sulfation altogether [21]. This model is illustrated in Fig. 4.2

According to the micrograin model, the rate of disappearance of  $\text{SO}_2$  at the particle surface will be a function of the rate of  $\text{SO}_2$  diffusion from the bed to the surface and the rate at which  $\text{SO}_2$  diffuses through the product layer. Analogous to the introduction of effectiveness factors to treat the combined effects of pore diffusion and surface reaction in catalysis [26,27], an effectiveness factor is used here to treat the combined effects pore diffusion and product layer diffusion

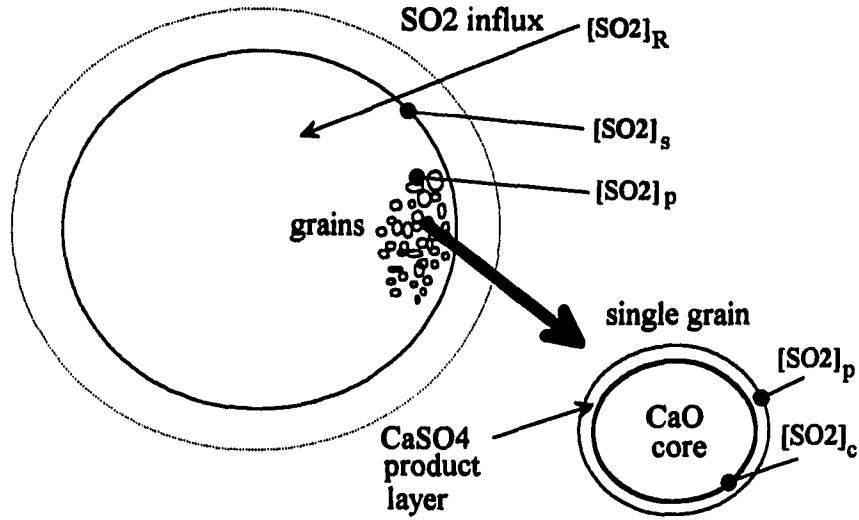


Figure 4.2: Grain model for sulfation

$$\frac{d[SO_2]_s}{dt} = h_s a_p \{ [SO_2]_R - [SO_2]_s \} + \eta_s \frac{D_{pl}}{t_{pl}} a_c \{ [SO_2]_c - [SO_2]_s \}, \quad (4.9)$$

where the  $D_{pl}$  is the product layer diffusion coefficient,  $t_{pl}$  is the product layer thickness,  $[SO_2]_c$  is the concentration of  $SO_2$  at the surface of the unreacted grain core, and  $a_c$  is the total available grain area per bed volume and is related to the B.E.T. area of the particle. Since total grain area decreases as product layer increases (e.g., grain core shrinks), this area must be evaluated according to

$$a_c = \left( \frac{r_{gc}}{r_g} \right)^2 S_g \rho_{ba}, \quad (4.10)$$

where  $r_{gc}$  is the radius of the unreacted grain core,  $r_g$  is the initial core radius,  $S_g$  is the B.E.T. area of calcined limestone, and  $\rho_{ba}$  is the bulk density of CaO in the bed. Furthermore, the

bulk density of CaO in the bed depends on the amount of calcined limestone available. The fractional conversion of CaCO<sub>3</sub> to CaO,  $f_c$ , is defined as

$$f_c = 1 - \frac{m_I}{m_L}, \quad (4.11)$$

where  $m_L$  is the initial mass of CaCO<sub>3</sub> in the bed. Thus the bulk density of CaO in the bed will be equal to the amount of CaO produced divided by the bed volume

$$\rho_{ba} = \frac{M_A f_c m_L}{M_L V_b}. \quad (4.12)$$

The effectiveness factor,  $\eta_s$ , is the ratio of the actual reaction rate to the reaction rate that would have resulted had the entire area  $a_c$  been exposed to the surface concentration of SO<sub>2</sub>. The effectiveness factor is defined in terms of the Thiele modulus for sulfation,  $\phi_s$ , [26, 27]

$$\eta_s = \frac{3}{\phi_s^2} (\phi_s \coth \phi_s - 1), \quad (4.13)$$

where the Thiele modulus is defined as the ratio of the product layer diffusion rate to the rate at which species diffuses through the particle pores

$$\phi_s = r_p \sqrt{\frac{D_{pl}}{t_{pl}} \frac{\rho_a S_g}{D_{es}}}, \quad (4.14)$$

where  $\rho_a$  is the density of the CaO particle and  $D_{es}$  is the effective diffusion coefficient of SO<sub>2</sub> through the pores.

Pore plugging during sulfation reduces the effective diffusivity  $D_{es}$  significantly. The process of pore plugging is only poorly understood. Szekely [28] has applied a semi-empirical

model to the closely related problem of pore plugging due to sintering during the reduction of nickel oxide by hydrogen. This model assumes that the effective diffusivity of the reactant gas through the pores follows the exponential decay

$$D_{si} = D_{so} e^{-\frac{(t-t_{si})}{\tau_{si}}} \quad (4.15)$$

The time constant  $\tau_{si}$  is the characteristic time associated with sintering and can be defined by an Arrhenius expression as

$$\frac{1}{\tau_{si}} = \frac{1}{\tau_{so}} \exp\left(-\frac{E_{as}}{R_u T}\right), \quad (4.16)$$

where  $\tau_{so}$  is the pre-exponential factor and  $E_{as}$  is the activation energy associated with sintering. The induction time,  $t_{si}$ , is the time it takes for the reaction front to reach a radius  $r$  inside the particle.

Analogous to sintering is the deposition of bulky  $\text{CaSO}_4$  in the pores during limestone sulfation. The reduction in effective diffusivity due to pore plugging can be modeled as an exponential decay,

$$D_{es} = D_{eso} e^{-t/\tau_p}, \quad (4.17)$$

where  $D_{eso}$  is the initial effective diffusivity of  $\text{SO}_2$  and  $\tau_p$  is the time constant associated with the plugging of the pores. No induction time is assumed for pore plugging. Similarly to sintering, the characteristic time for pore plugging is defined by an Arrhenius expression

$$\frac{1}{\tau_p} = \frac{1}{\tau_{po}} \exp\left(-\frac{E_{ap}}{R_u T}\right), \quad (4.18)$$

where  $\tau_{po}$  is the pre-exponential factor and  $E_{ap}$  is the apparent activation energy associated with pore plugging.

The concentration of  $SO_2$  at the reaction site will depend on the rate at which species diffuses through the product layer and the rate at which  $SO_2$  is consumed by sulfation at the reaction site

$$\frac{d[SO_2]_c}{dt} = \eta_s \frac{D_{pl}}{l_{pl}} a_c \{ [SO_2]_s - [SO_2]_c \} - k_s a_c [SO_2]_c. \quad (4.18)$$

Finally, the radius of the unreacted grain core is given by

$$\frac{dr_{gc}}{dt} = -k_s M_A [SO_2]_c / \rho_g. \quad (4.19)$$

The system of 8 differential equations was solved numerically using FORTRAN 77 and the stiff equation subroutine D02EAF from the NAG library on the Vincent workstations. Rate constants and other parameters used in the simulation were taken from literature. Mass transfer coefficients were estimated using empirical relationships for particles in fluidized beds. All parameters used in the simulations are listed in Appendix B. Initial conditions are also listed in Appendix B.

### 4.3 Model results

The simulation was performed using 1 mm limestone particles at 850 °C and 1 m/s fluidization velocity. Carbon dioxide profiles are plotted versus time in Figs. 4.3 and 4.4. Figure 4.3 compares the model response with the equivalent experimental data from a 1 mm limestone test. Evidently, the model follows the data closely for a value of  $k_c = 0.2$  m/s, computed from experimental time constants in this work as described Appendix B, which is significantly higher than the calcination rate constants reported in literature. The concentrations of  $CO_2$  at

the particle surface and unreacted core,  $[CO_2]_s$  and  $[CO_2]_c$  respectively, are shown in Fig. 4.4. The  $CO_2$  at the particle surface rises to 5.5% above background and decays exponentially thenceforth, whereas the core concentration, after reaching a maximum of 6% above background, decays linearly and does not seem to return to background.

Reactor concentrations of  $SO_2$  follow different profiles according to which regime is rate limiting. If  $\tau_p$  is made very large, i.e. if pore diffusion does not become rate limiting, the  $SO_2$  concentration for calcined stone (Fig. 4.6) drops to a minimum of 650 ppm rising slowly thereafter. The  $SO_2$  profile, in this case, requires around 67 minutes to return to background, whereas, experimentally it takes only 7 minutes for the background concentration to be reached (also shown in Fig. 4.6). The slow-down observed in the simulation results from product layer diffusion becoming rate limiting. Varying the product layer diffusivity, sulfation rate constant, or film mass transfer coefficient of  $SO_2$  in the simulation did not seem to improve model predictions as long as  $\tau_p$  was very large.

Based on these observations, it was deduced that pore plugging is the primary mechanism that forces the  $SO_2$  concentration to return to background within 400 seconds as observed experimentally. As it will be shown in a later section of this chapter, the time constant for pore plugging,  $\tau_p$ , is equal to 1/2 the time constant for sulfation,  $\tau_s$ . This relationship was used to calculate a value of  $\tau_p$  from experimental data on sulfation (Appendix B). The model response for calcined limestone with pore plugging (variable pore diffusivity) is also shown in Fig. 4.6. This model follows the experimental data closely except during the initial  $SO_2$  concentration drop. This disagreement is attributed to the lag time of the sampling system or to slow calcination. The sampling system used in the experiments embodies extensive filtering prior to introducing the gas to the analyzers. The combustor and the sampling system can be modeled as two CSTRs in series with an overall time constant  $\tau_p$ , which was estimated to be 3 s. This characteristic lag time slows down the system response during the initial drop in the  $SO_2$  concentration, which otherwise would have been significantly faster.

The effect of calcination on the profile (pore plugging included) for a calcination rate constant of 0.2 m/s is also plotted in Fig. 4.6 using a value of  $\tau_p$  of 60 s. There is a significant difference between this profile and the experimental data. This behavior can be explained in terms of the diffusion of species from the bed to the particle's surface. The concentration of  $\text{SO}_2$  at the particle surface, shown in Fig. 4.7, follows a similar pattern to the experimental reactor concentration. In comparison to the  $\text{SO}_2$  concentration in the reactor, the particle surface concentration drops rapidly. Evidently, if a higher bed to particle mass transfer coefficient is used, the bed concentration of  $\text{SO}_2$  would become equal to the surface concentration, thus following an equivalent profile.

As expected, the core concentration of  $\text{SO}_2$  is quickly depleted due to fast reaction kinetics (Fig. 4.8), suggesting that chemical kinetics are not rate limiting in the sulfation of CaO. The radius of the unreacted CaO grain core (plotted in Fig. 4.9) drops sharply in the first few

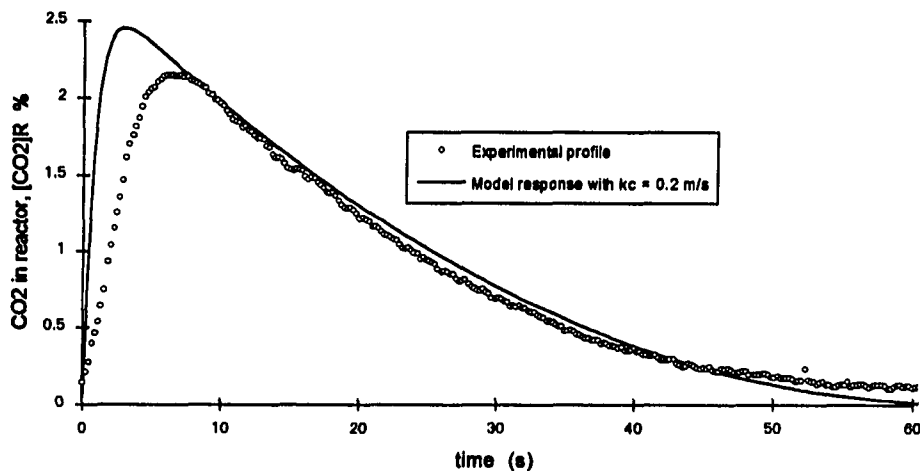


Figure 4.3: Experimental and theoretical  $\text{CO}_2$  profiles

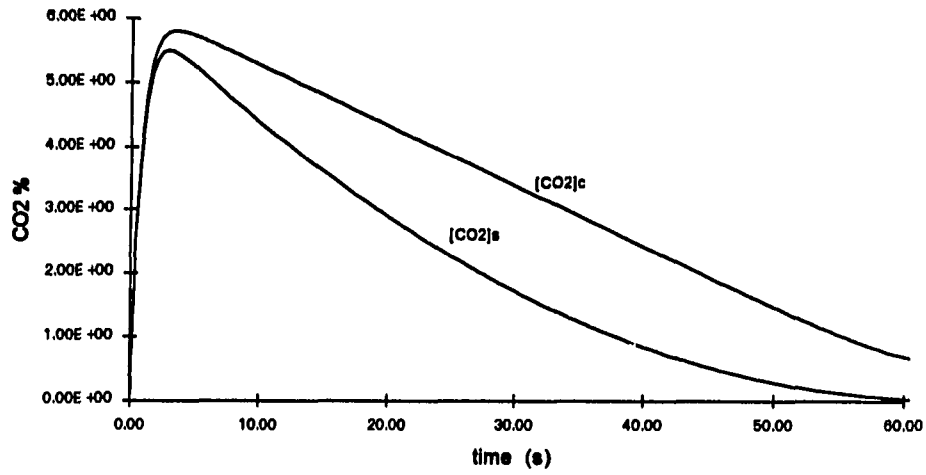


Figure 4.4: Surface and core CO<sub>2</sub> concentrations vs. time

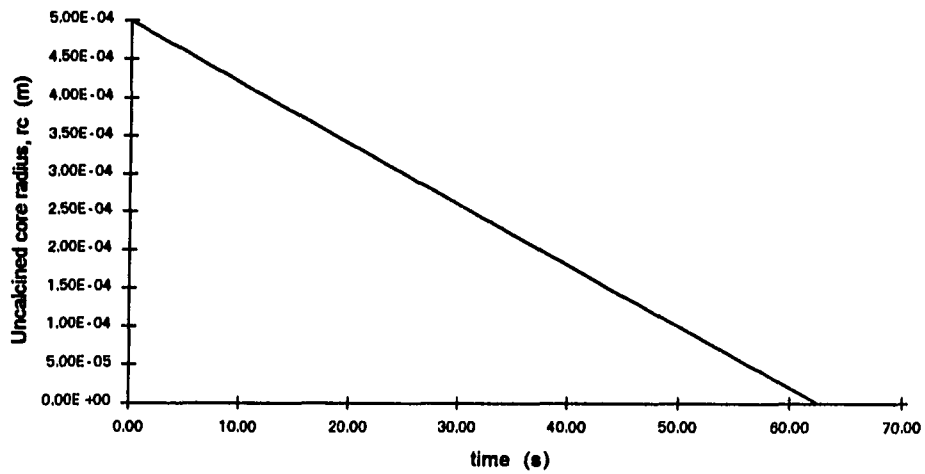


Figure 4.5: Radius of uncalcined CaCO<sub>3</sub> core

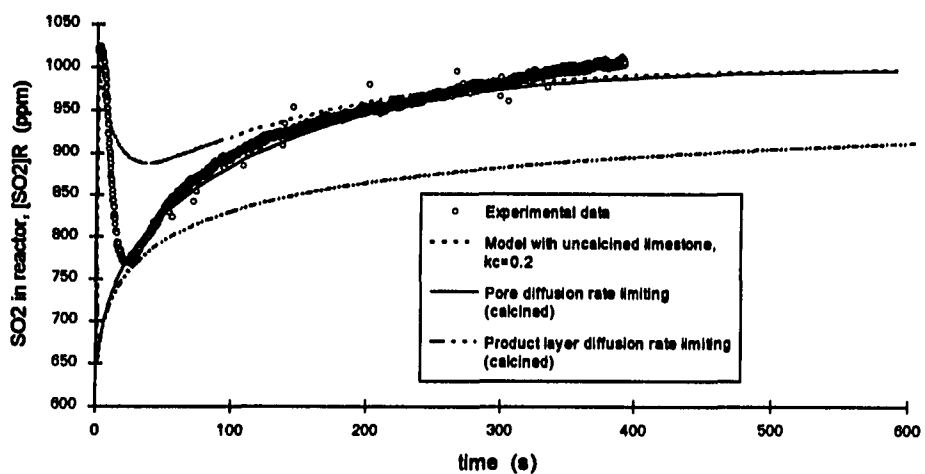


Figure 4.6: Experimental and theoretical response of SO<sub>2</sub> in the reactor

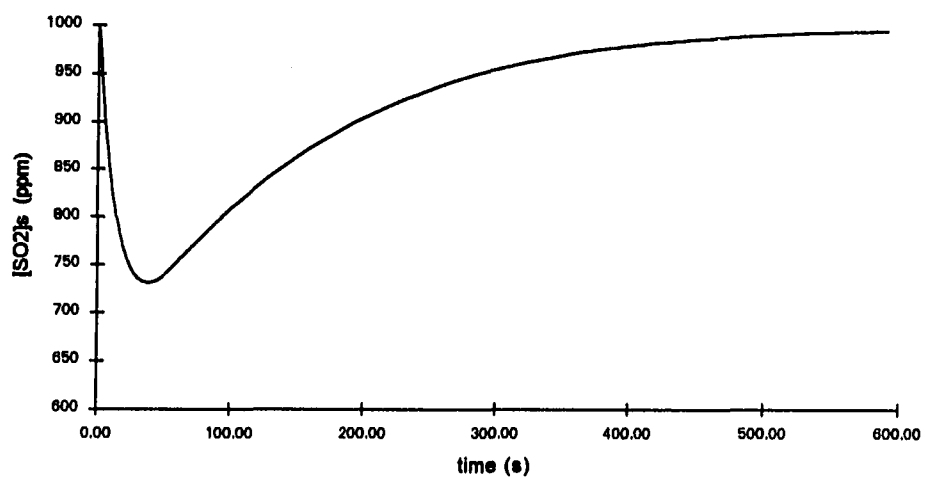


Figure 4.7: Film concentration of SO<sub>2</sub> vs. time

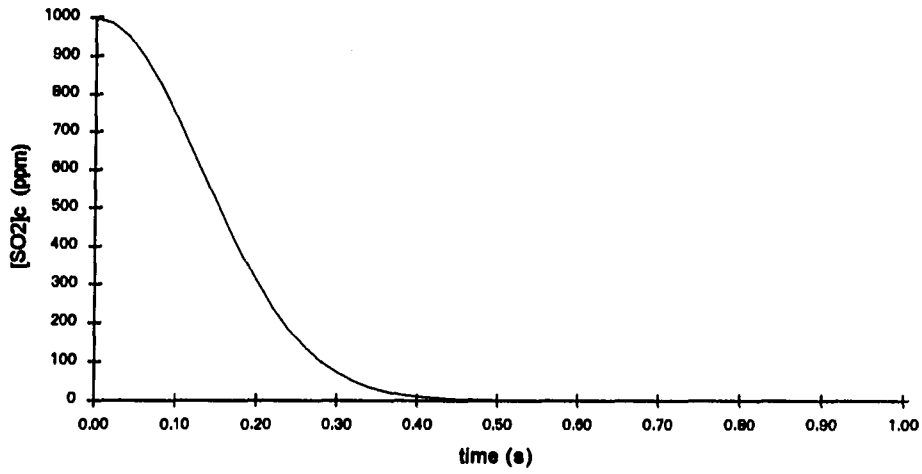


Figure 4.8: Concentration of SO<sub>2</sub> at surface of unreacted grain

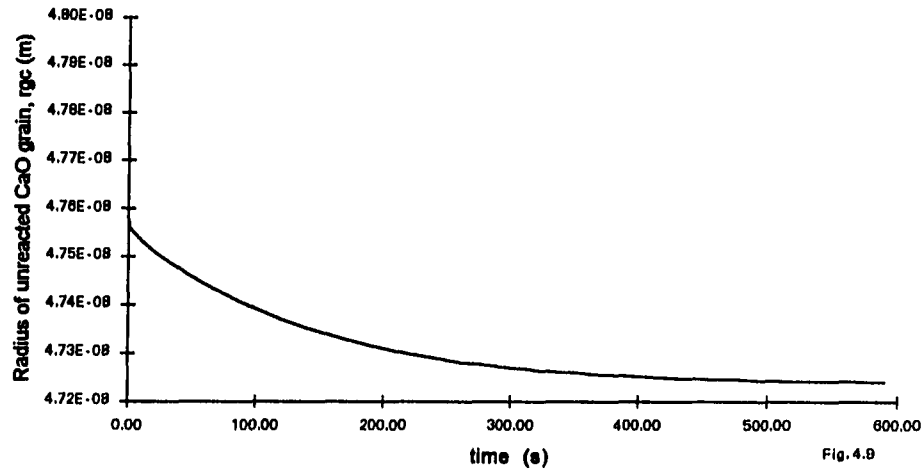


Figure 4.9: Radius of unreacted CaO grain core vs. time

seconds, suggesting that fast kinetics build up a thin layer of  $\text{CaSO}_4$  on the grain surface. Soon pore sizes are reduced because of product deposits on the pore walls and pore diffusion becomes rate limiting. Slow pore diffusion reduces the incoming flux of  $\text{SO}_2$  from the particle's exterior, thus slowing down the product layer build-up. This slow-down is evident in Fig. 4.9.

#### 4.4 Model simplification

Comparing the time histories of  $\text{CO}_2$  and  $\text{SO}_2$ , it is evident that calcination is complete before sulfation has proceeded very far. Carbon dioxide reaches the background within the first 62 seconds whereas, in the same time,  $\text{SO}_2$  reaches a minimum. Also, the gas residence time in the combustor is fairly small compared to other processes, thus quasi-steady assumptions can be made for all gaseous species. Based on these observations, the model can be simplified for use with the experimental data.

##### 4.4.1 Calcination

A quasi-steady assumption for the concentration of  $\text{CO}_2$  in the bed, at the particle surface, and at the surface of the unreacted particle core is made. This assumption is justified by the fact that the gas residence time,  $L/u$ , in the bed is relatively small (around 6.7 s) compared to other processes. Based on this hypothesis the transient terms in Eqs. 4.1, 4.3, and 4.4

$$\frac{d[\text{CO}_2]_R}{dt} \approx \frac{d[\text{CO}_2]_s}{dt} \approx \frac{d[\text{CO}_2]_c}{dt} \approx 0. \quad (4.20)$$

Equation 4.20 implies that Eqs. 4.1, 4.3, and 4.4 can be set to zero and solved for the concentration of  $\text{CO}_2$  in the reactor to yield

$$[\text{CO}_2]_R - [\text{CO}_2]_i = k_c a_r \frac{L}{u} = 4\pi k_c \frac{L}{u} \frac{N}{V_b} r_c^2 \quad (4.21)$$

The core radius can be expressed in terms of time by directly integrating Eq. 4.6

$$r_c = r_p \left( 1 - \frac{k_c M_L}{\rho_L r_p} t \right). \quad (4.22)$$

Recall Taylor's expansion for the exponential  $e^{-bx}$

$$e^{-bx} = 1 - bx + b^2 \frac{x^2}{2!} + \dots, \quad (4.23)$$

which, for short times, can be approximated as  $e^{-bx} \approx 1 - bx$ . Using this approximation, Eq. 4.22 can be written in terms of an exponential

$$r_c = r_p \exp \left( -\frac{t}{\tau'_c} \right), \quad (4.24)$$

where  $\tau'_c$  is defined as

$$\tau'_c \equiv \frac{\rho_L r_p}{k_c M_L}. \quad (4.25)$$

Equation 4.24 can be substituted into Eq. 4.21 yields

$$[CO_2]_R - [CO_2]_i = 4\pi k_c \frac{L}{u} \frac{N}{V_b} r_p^2 \exp \left( -\frac{t}{\tau_c} \right), \quad (4.26)$$

where  $\tau_c = \tau'_c/2$ . At time  $t = 0$ , the concentration of  $CO_2$  in the reactor is equal to  $[CO_2]_o$  and

$$[CO_2]_R - [CO_2]_o = 4\pi k_c \frac{L}{u} \frac{N}{V_b} r_p^2. \quad (4.27)$$

where  $[CO_2]_o$  is the maximum concentration of  $CO_2$  reached during calcination of the limestone batch. Equation 4.26 is divided by Eq. 4.27 to obtain the dimensionless form

$$\frac{[CO_2]_R - [CO_2]_i}{[CO_2]_o - [CO_2]_i} = \exp\left(-\frac{t}{\tau_c}\right). \quad (4.28)$$

Equation 4.28 can be used to estimate the calcination time constant,  $\tau_c$ , from the  $CO_2$  profiles obtained during calcination.

#### 4.4.2 Sulfation

Due to the slow sulfation kinetics, a quasi-equilibrium assumption can be made for the concentration of  $SO_2$  at the reaction site,  $[SO_2]_c$ , thus Eq. 4.18 becomes

$$\frac{d[SO_2]_c}{dt} = \eta_s \frac{D_{pl}}{t_{pl}} a_c \{ [SO_2]_s - [SO_2]_c \} - k_s a_c [SO_2]_c = 0. \quad (4.29)$$

Solving Eq. 4.29 for  $[SO_2]_c$  yields

$$[SO_2]_c = \frac{\eta_s \frac{D_{pl}}{t_{pl}} [SO_2]_s}{\eta_s \frac{D_{pl}}{t_{pl}} + k_s}. \quad (4.30)$$

The same quasi-equilibrium assumption can be made for the concentration of  $SO_2$  at the particle surface and the reactor,  $[SO_2]_s$  and  $[SO_2]_R$  respectively. Thus, Eq. 4.16

$$\frac{d[SO_2]_s}{dt} = h_s a_p \{ [SO_2]_R - [SO_2]_s \} + \eta_s \frac{D_{pl}}{t_{pl}} a_c \{ [SO_2]_c - [SO_2]_s \} = 0, \quad (4.31)$$

can be solved for the concentration of SO<sub>2</sub> at the particle surface by substituting for [SO<sub>2</sub>]<sub>c</sub> from Eq. 4.30 into Eq. 4.31

$$[SO_2]_s = \frac{h_s a_p [SO_2]_R}{h_s a_p + k_1 a_c}, \quad (4.32)$$

where  $k_1$  is defined as

$$k_1 = \left( \frac{t_{pl}}{\eta_s D_{pl}} + \frac{1}{k_s} \right)^{-1}. \quad (4.33)$$

According to the quasi-equilibrium assumption, Eq. 4.8 can be also be set to zero and solved for the concentration of SO<sub>2</sub> in the reactor in terms of the inlet SO<sub>2</sub> concentration to yield

$$[SO_2]_R = \frac{[SO_2]_i}{1 + k_2}, \quad (4.34)$$

where  $k_2$  is defined as

$$k_2 = \frac{V_b/Q}{1/(k_1 a_c) + 1/(h_s a_p)}. \quad (4.35)$$

Equation 4.34 can take different forms according to which regime is limiting: film diffusion, chemical reaction, pore diffusion, bulk mass transfer, or product layer diffusion.

#### a. Film diffusion is rate limiting

Film diffusion limited sulfation implies that  $1/h_s a_p \gg 1/k_s a_c$ , thus Eq. 4.35 becomes

$$k_2 = h_s a_p V_b/Q. \quad (4.36)$$

Substituting Eq. 4.36 into Eq. 4.34 yields

$$[SO_2]_R = \frac{[SO_2]_i}{1 + h_s a_p \frac{V_b}{Q}}, \quad (4.37)$$

which is independent of time, something that is not observed with either model simulation or the experiments. Consequently, film diffusion is not rate limiting in sulfation.

### b. Chemistry is rate limiting

If product layer diffusion is not rate limiting, then  $[SO_2]_s = [SO_2]_c$  and  $k_1 = k_s$ . If film diffusion is not rate limiting,  $[SO_2]_s = [SO_2]_R$  and  $k_2 = \eta_s k_s a_c V_b / Q$ . Accordingly, Eq. 4.34 yields the solution

$$[SO_2]_R = \frac{[SO_2]_i}{1 + \eta_s k_s a_c V_b / Q}. \quad (4.38)$$

Substituting  $a_c = \rho_{ba} S_g (r_{gc}/r_g)^2$  in Eq. 4.38 yields

$$[SO_2]_R = \frac{[SO_2]_i}{1 + k_3 \left(\frac{r_{gc}}{r_g}\right)^2}, \quad (4.39)$$

where  $k_3$  is

$$k_3 = \eta_s k_s \rho_{ba} S_g \frac{V_b}{Q}. \quad (4.40)$$

The grain core radius as a function of time can be estimated from Eq. 4.19 by noting that  $[SO_2]_s \approx [SO_2]_R$ :

$$\frac{dr_{gc}}{dt} = - \frac{\eta_s k_s M_A [SO_2]_R}{\rho_g}. \quad (4.41)$$

Substituting Eq. 4.38 into Eq. 4.40 and integrating for  $r_c$  yields

$$\left(1 - \frac{r_{gc}}{r_g}\right) + \frac{k_3}{3} \left[1 - \left(\frac{r_{gc}}{r_g}\right)^3\right] = \eta_s k_s M_A \frac{[SO_2]_i}{\rho_g r_g} t. \quad (4.42)$$

For chemistry being rate limiting, constant  $k_3$  is small (since it depends on the reaction rate constant). Then the assumption that

$$1 - \frac{r_{gc}}{r_g} \gg \frac{k_3}{3} \left[1 - \left(\frac{r_{gc}}{r_g}\right)^3\right]. \quad (4.43)$$

can be made and Eq. 4.42 can be approximated by

$$1 - \frac{r_{gc}}{r_g} = \eta_s k_s M_A \frac{[SO_2]_i}{\rho_g r_g} t, \quad (4.44)$$

For short times compared to the sulfation time, Eq. 4.44 approximated with the exponential form

$$r_{gc} = r_g \exp\left(-\frac{t}{\tau_{ch}}\right), \quad (4.45)$$

where

$$\tau_{ch} = r_g \frac{\rho_g}{\eta_s k_s M_A [SO_2]_i}, \quad (4.46)$$

which suggests that the time constant for chemistry rate limited sulfation is proportional to the grain size (a reasonable result for the shrinking grain core model since the reaction occurs at the grain level) and inversely proportional to the reaction rate constant. Equation 4.45 is substituted into Eq. 4.39 to yield

$$[SO_2]_R = \frac{[SO_2]_i}{1 + k_3 \exp\left(-\frac{t}{\tau_s}\right)}, \quad (4.47)$$

where  $\tau_s = \tau_{ch}/2$ . Noting that at  $t = 0$  the concentration of  $SO_2$  in the reactor becomes  $[SO_2]_o$ , Eq. 4.47 can be simplified to the form

$$\frac{[SO_2]_i/[SO_2]_R - 1}{[SO_2]_i/[SO_2]_o - 1} = \exp\left(-\frac{t}{\tau_s}\right). \quad (4.48)$$

For small perturbations in the  $SO_2$  background (small changes of  $[SO_2]_R$  from  $[SO_2]_i$ ), Eq. 4.48 can be changed to the more convenient form

$$\frac{[SO_2]_R - [SO_2]_o}{[SO_2]_i - [SO_2]_o} = \exp\left(-\frac{t}{\tau_s}\right). \quad (4.49)$$

If chemistry is rate limiting during sulfation, the time constant  $\tau_s$  is expected to be a weak function of temperature and independent of particle size.

### c. Product layer diffusion is rate limiting

If product layer diffusion is rate limiting, then Eq. 4.32 becomes

$$[SO_2]_c = \frac{\eta_s D_{pl}}{k_s t_{pl}} [SO_2]_s \quad (4.50)$$

and

$$k_1 = \eta_s \frac{D_{pl}}{t_{pl}}. \quad (4.51)$$

Since product layer diffusion is rate limiting,  $[SO_2]_s = [SO_2]_R$  and

$$k_2 = \eta_s \frac{D_{pl}}{t_{pl}} a_c \frac{V_b}{Q}. \quad (4.52)$$

Substituting Eq. 4.52 into Eq. 4.34 yields

$$[SO_2]_R = \frac{[SO_2]_i}{1 + \eta_s \frac{D_{pl} a_c V_b}{t_{pl} Q}}. \quad (4.53)$$

When  $a_c$  is substituted into Eq. 4.53, gives a form similar to Eq. 4.39

$$[SO_2]_R = \frac{[SO_2]_i}{1 + k_4 \left( \frac{r_{gc}}{r_g} \right)^2}, \quad (4.54)$$

where

$$k_4 = \frac{\eta_s D_{pl} \rho_{ba} S_g V_b}{t_{pl} Q}. \quad (4.55)$$

Also, substituting  $[SO_2]_c$  from Eq. 4.50 into Eq. 4.19 and noting that  $[SO_2]_s = [SO_2]_R$ , yields a differential equation for the radius of the unreacted grain core

$$\frac{dr_{gc}}{dt} = - \frac{M_A [SO_2]_i}{\rho_g} \left( \frac{t_{pl}}{\eta_s D_{pl}} + a_c \frac{V_b}{Q} \right)^{-1}. \quad (4.56)$$

Furthermore, the specific area  $a_c$  and the product layer thickness  $t_{pl}$  are substituted into Eq. 4.56

$$\frac{dr_{gc}}{dt} = - \frac{M_A [SO_2]_i}{\rho_g} \left[ \frac{r_g - r_{gc}}{\eta_s D_{pl}} + \rho_{ba} S_g \frac{V_b}{Q} \left( \frac{r_{gc}}{r_g} \right)^2 \right]^{-1}. \quad (4.57)$$

Integrating Eq. 4.57 with respect to time yields

$$\begin{aligned} & \frac{1}{\eta_s D_{pl}} \left\{ \frac{r_{gc}}{r_g} - 1 \right\} - \frac{1}{2\eta_s D_{pl}} \left\{ \left( \frac{r_{gc}}{r_g} \right)^2 - 1 \right\} \\ & + \frac{\rho_{ba} S_g V_b}{3 Q r_g} \left\{ \left( \frac{r_{gc}}{r_g} \right)^3 - 1 \right\} = - \frac{M_A [SO_2]_i}{\rho_g r_g^2} t. \end{aligned} \quad (4.58)$$

Since product layer diffusion is rate limiting (i.e.  $D_{pl}$  is small), the quantity  $1/(\eta_s D_{pl})$  is expected to be much larger than  $\rho_{ba} S_g V_b / (3 Q r_g)$ . Thus, Eq. 4.58 can be simplified to

$$1 - 2 \left( \frac{r_{gc}}{r_g} \right) + \left( \frac{r_{gc}}{r_g} \right)^2 = \frac{2 \eta_s D_{pl} M_A [SO_2]_i}{\rho_g r_g^2} t. \quad (4.59)$$

Eq. 4.59 can be simplified to

$$\left( 1 - \frac{r_{gc}}{r_g} \right)^2 = \frac{2 \eta_s D_{pl} M_A [SO_2]_i}{\rho_g r_g^2} t, \quad (4.60)$$

which cannot be easily linearized. For times short compared to the sulfation time, Eq. 4.60 can be approximated with a simple exponential

$$r_{gc} = r_g \exp \left[ - \sqrt{\left( \frac{t}{\tau_{pl}} \right)} \right], \quad (4.61)$$

where the time constant  $\tau_{pl}$  is defined as

$$\tau_{pl} = r_g^2 \frac{\rho_g}{2 \eta_s D_{pl} M_A [SO_2]_i}, \quad (4.62)$$

which suggests that the time constant is proportional to the square of the grain size. This result is in agreement with Borgwardt and Harvey [29] who estimated that the rate of sulfation (inverse sulfation time constant) of small, non-porous limestone particles is proportional to  $1/r_p^2$ .

Furthermore, if Eq. 4.61 is substituted into Eq. 4.54 and manipulated, the dimensionless  $SO_2$  concentration can be obtained

$$\frac{[SO_2]_R - [SO_2]_o}{[SO_2]_i - [SO_2]_o} = \exp \left[ -\sqrt{\left(\frac{t}{\tau_s}\right)} \right], \quad (4.63)$$

where  $\tau_s = \tau_{pl}/4$ . The dimensionless  $SO_2$  concentration in Eq. 4.63 can be plotted vs. time on a log-linear scale to obtain the slope  $\sqrt{\tau_s}$ .

#### d. Bulk mass transfer is rate limiting

If film diffusion is not rate limiting, then the rate at which  $SO_2$  is advected through the bed (bulk mass transfer) may be rate limiting. Assuming that product layer diffusion is not rate limiting, Eq. 4.42 can be derived, which for chemistry not being rate limiting, i.e.

$$1 - \frac{r_{gc}}{r_g} \ll \frac{k_3}{3} \left[ 1 - \left(\frac{r_{gc}}{r_g}\right)^3 \right], \quad (4.64)$$

can be simplified to

$$\frac{k_3}{3} \left[ 1 - \left(\frac{r_{gc}}{r_g}\right)^3 \right] = \eta_s k_s M_A \frac{[SO_2]_i}{\rho_g r_g}. \quad (4.65)$$

Eq. 4.65 can be linearized around  $r_{gc}/r_g = 1$  to yield the simple exponential relationship

$$\frac{r_{gc}}{r_g} = \exp \left( -\frac{t}{\tau_{bm}} \right), \quad (4.66)$$

where the time constant for bulk mass transfer,  $\tau_{bm}$ , is defined as

$$\tau_{bm} = \frac{V_b r_g S_g \rho_{ba} \rho_g}{Q 2M_A [SO_2]_i} \quad (4.67)$$

The time constant  $\tau_{bm}$  does not depend on the reaction rate constant or particle size. Instead, it is a function of the bed parameter  $Q/V_b$  and the physical properties of CaO grains.

Equation 4.66 is substituted into Eq. 4.39 to obtain the exponential decay for the  $SO_2$  in the bed

$$\frac{[SO_2]_R - [SO_2]_o}{[SO_2]_i - [SO_2]_o} = \exp\left(-\frac{t}{\tau_s}\right) \quad (4.68)$$

where  $\tau_s = \tau_{bm}/2$ . A similar expression can be derived from Eq. 4.58 with the assumption that product layer diffusion is faster than bulk mass transfer.

#### e. Pore diffusion is rate limiting

Recall Eq. 4.39

$$[SO_2]_R = \frac{[SO_2]_i}{1 + \eta_s k_s \rho_{ba} S_g \frac{V_b r_{gc}^2}{Q r_g^2}} \quad (4.69)$$

If pore diffusion is rate limiting, the grain core does not significantly shrink, i.e.  $r_{gc} \approx r_g$ . For large Thiele modulus values (i.e. slow pore diffusion), the effectiveness factor is inversely proportional to the Thiele modulus, i.e.  $\eta_s = 3/\phi_s$ , where

$$\phi_s = r_p \sqrt{\frac{D_{pl} \rho_a S_g}{t_{pl} D_{es}}} \quad (4.71)$$

Substituting  $D_{es} = D_{eso} e^{-t/\tau_p}$  into Eq. 4.69, yields

$$\phi_s = e^{t/2\tau_p} r_p \sqrt{\frac{D_{pl}}{t_{pl}} \frac{\rho_a S_g}{D_{eso}}} \quad (4.72)$$

Assuming that  $r_g = r_{gc}$ , and substituting the effectiveness factor into Eq. 4.69 gives

$$[SO_2]_R = \frac{[SO_2]_i}{1 + \frac{3}{\phi_s} k_s \rho_{ba} S_g \frac{V_b}{Q}} = \frac{[SO_2]_i}{1 + k_5 e^{-t/2\tau_p}} \quad (4.73)$$

where

$$k_5 = \frac{3k_s m_a}{r_p Q} \sqrt{\frac{S_g D_{eso}}{\rho_a D_{pl}/t_{pl}}} \quad (4.74)$$

Noting that at  $t = 0$ ,  $[SO_2]_R = [SO_2]_o$ , Eq. 4.73 can be simplified to the dimensionless form

$$\frac{[SO_2]_i/[SO_2]_R - 1}{[SO_2]_i/[SO_2]_o - 1} = \exp\left(-\frac{t}{\tau_s}\right), \quad (4.75)$$

where in this case  $\tau_s = 2\tau_p$ . The parameter  $k_5$  in Eq. 4.74 is a form of dimensionless ratio of the effective pore diffusivity of  $SO_2$  and the product layer diffusion coefficient.

Equation 4.75 can be further simplified, for small perturbations of  $SO_2$  from the background, to yield the result

$$\frac{[SO_2]_R - [SO_2]_o}{[SO_2]_i - [SO_2]_o} = \exp\left(-\frac{t}{\tau_s}\right), \quad (4.76)$$

where  $\tau_s = 2\tau_p$ . This time constant relationship is verified via comparison of the experimental and theoretical results in Fig. 4.6. The  $SO_2$  profile for calcined stone was obtained using  $\tau_p = 60$  s, which is approximately half of the time constant for sulfation ( $\tau_s = 128$  s). This demonstrates that the comprehensive and simplified models are consistent with one another.

## **5. EXPERIMENTAL APPARATUS**

### **5.1 Combustor**

The 0.2 m dia. fluidized bed combustor is shown schematically in Fig. 5.1. The distributor plate at the bottom of the bed is made out of stainless steel perforated with 250 2.4 mm holes. A 40-mesh stainless steel screen, spot welded on the plate, prevents material flow to the plenum and acts as a flame arrestor. The main body of the combustor consists of a mild steel water jacket lined with a 25 mm thick Kaocast RFT castable refractory. The plenum at the bottom of the bed serves as a mixing chamber for the air and liquefied petroleum (LP) gas mixture during the pre-heating cycle.

A 1.22 m long mild steel freeboard extends above the main body of the combustor serves both as an afterburner for elutriated fines, for improvement of combustion efficiency, and as a muffler. The flue gas exits the combustor via a roof-mounted exhaust fan.

Ignition of the preheat gas is achieved via two 10 cm long electrodes connected to a 10 kV transformer. The electrodes are bend downwards to ignite the LP gas as close as possible to the bed.

### **5.2 Fuel and sorbent feeding systems**

The preheat and heating cycles for batch tests were carried out using LP gas for fuel. Coal batches were fed to the bed via a 63 mm dia. slanted port on the side of the freeboard. A ball valve allowed closure of the port while pre-weighed fuel samples were loaded in. When the data recording routine was initiated, the valve was opened to dispense the batch into the bed.

Limestone tests were carried out under simulated coal combustion conditions. Natural gas was used to heat the bed to steady state. Pure sulfur dioxide was injected into the main air line to the combustor via a metering needle valve as shown in Fig. 5.1. Limestone was

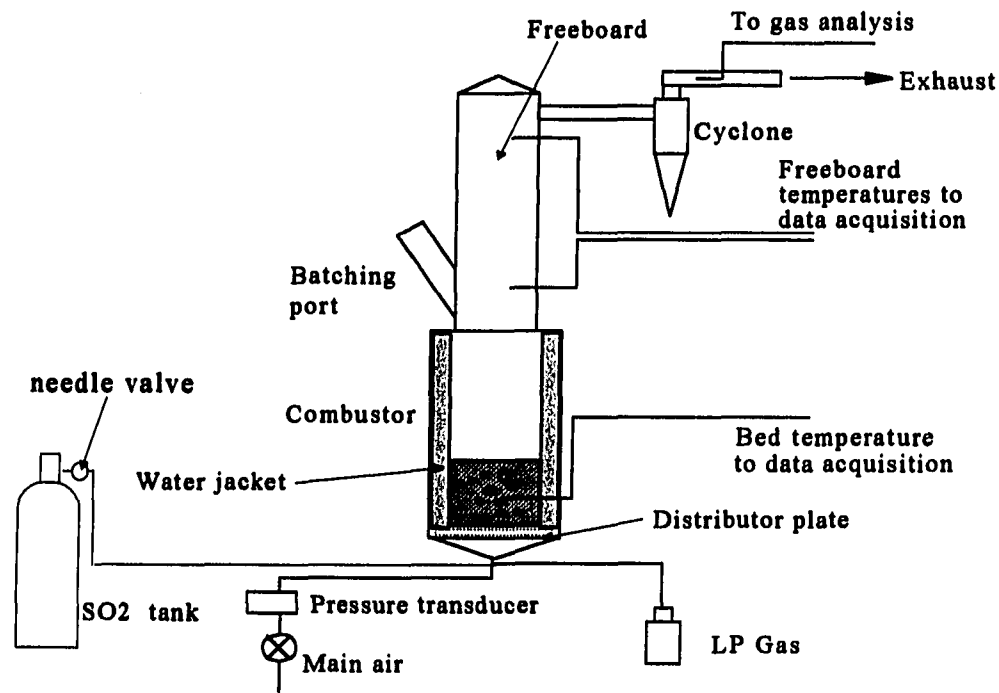


Figure 5.1: Experimental apparatus.

batched into the bed through the same port as the coal samples. The data recording program was initiated and the valve was opened to dispense the sorbent into the bed.

### 5.3 Gas sampling system

Five gas analyzers are used to monitor flue gas composition in the bed. Two Beckman Model 870 nondispersive infrared spectrometers measure CO and CO<sub>2</sub>, a Beckman Model 855 paramagnetic oxygen analyzer records O<sub>2</sub>, a Horiba VIA-300 is used to monitor NO<sub>x</sub>, and a Horiba VIA-500 monitors SO<sub>2</sub>.

Figure 5.2 shows the gas sampling and conditioning system used to process the flue gas prior to analysis. A sample of flue gas is extracted after the cyclone exhaust via a probe facing downstream in the flow, which reduces the amount of solids entering the sampling lines. The sampling line up to the filtering system is heat traced to approximately 250 °C. A

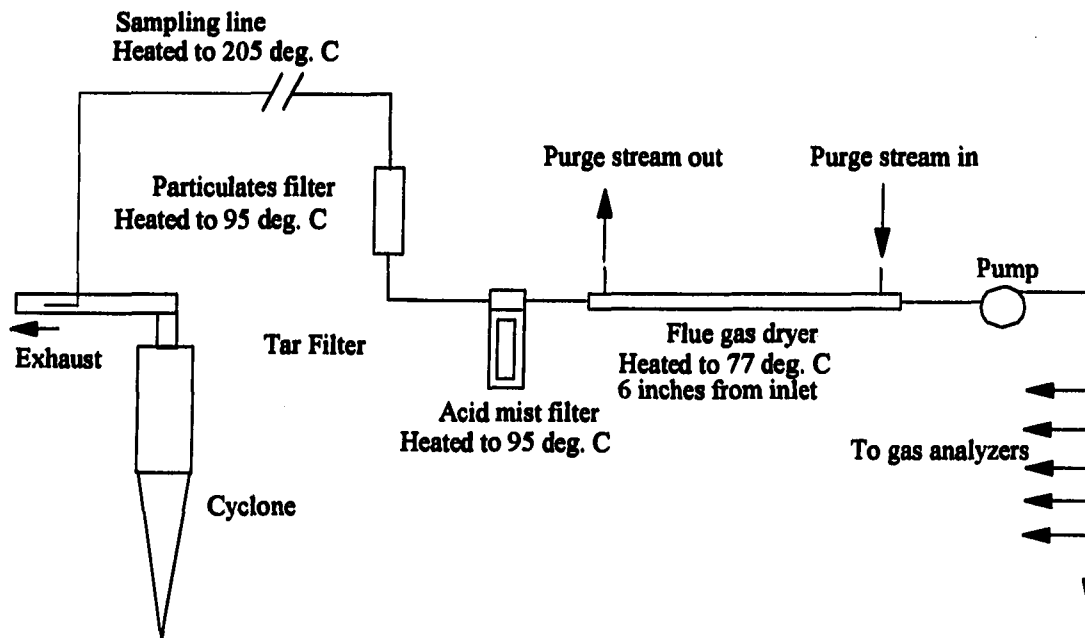


Figure 4.2: Gas sampling and filtering system.

Balston 30/12 microfibre filter, heat traced to 100 °C, is used to remove entrained solids from the sample at the entrance to the gas analysis unit. Acid mist is removed via a Perma Pure Model F-275-EG acid mist filter.

A Perma-Pure PD625-24APS membrane dryer was used to remove moisture from the sample. The dryer consists of fifty 0.5 mm dia. organic semi-permeable membrane tubes enclosed in a stainless steel tube. The moist flue gas sample flows inside the membrane tubes.

Dry purge air is passed outside the membranes through the stainless steel tube. Because of the differential water vapor pressure gradient, moisture from the flue gas flows through the walls of the membrane tubes into the dry purge stream. To obtain optimum moisture removal, the dryer is heated 15 cm from the inlet to a temperature of 77 °C. Dry purge air is produced by a Perma-Pure HD202-b heatless zeolite dryer capable of drying the air to a dew point of -45 °C. The drying system can dry the flue gas to a dew point of -9 to -12 °C.

#### **5.4 Data acquisition system**

The data acquisition system consists of an HP Vectra 386 SX-16 computer. Temperatures are measured using Type K thermocouple probes installed at locations shown in Fig. 5.1. The thermocouples are connected to two Metrabyte Model EXP-16 sub-multiplexer boards provided with a cold junction compensation. Amplifiers on the boards boost the signal to 0-5 V DC. An 8-channel type DAS-8 D/A converter is used to convert the analog signal from the thermocouple boards to a digital signal. Primary air flow is measured via a Shaevitz P3061 linear-variable-differential transformer (LVDT) pressure transducer. Compensation for the zero shift on the pressure transducer is available within the data acquisition code. Noise picked up in the air lines is filtered out via an analog low-pass filter. The 0-5 V DC transducer output is also fed to the DAS-8 for conversion. Flue gas concentrations are fed to the DAS-8 directly from the output stage of the analyzers which also provide a 0-5 V DC signal.

A program written in BASIC 7 monitors the output of the DAS-8. All data are continuously monitored throughout the tests. The routine is capable of logging data at a maximum rate of 7 data points per second.

## **6. MATERIALS AND METHODS**

### **6.1 Fuels and sorbents**

Coal batch tests were carried out using Indiana V bituminous coal the analysis of which is given in Table 6.1. The fuel was crushed and double-sieved to obtain sizes between 0.6 and 6 mm. Limestone was obtained from the Gilmore City formation in Iowa. An analysis of the sorbent is shown in Table 6.2. The limestone was also crushed and double sieved to different sizes (0.2-2 mm).

### **6.2 Methods and Techniques**

#### **6.2.1 Coal and char batch tests**

Coal batch tests were initiated by preheating the bed with propane gas until a temperature of 850 °C was reached. The air was then adjusted to achieve a bed velocity of 1 m/s, and the propane was regulated to keep the temperature to within 10 degrees of 850 °C. At these conditions, the oxygen level in the bed was 6-7 % and the background CO<sub>2</sub> 7-8 %.

Five grams of coal were placed inside the batching port with the ball valve closed. The data acquisition recording routine was turned on, and after approximately 5 seconds, the ball valve was opened to let the coal fall in the bed. Data logging was continued until the concentration of CO<sub>2</sub> reached the initial background from the combustion of propane.

#### **6.2.2 Limestone batch tests**

Limestone batch tests were carried out using simulated coal combustion. Natural gas was used to heat the bed to around 850 °C, at which point the air was adjusted to achieve a bed velocity of 1 m/s, and the fuel was regulated to keep the temperature to within 10 degrees of 850 °C. Pure SO<sub>2</sub> was injected to the combustor via a small metering needle valve so that the concentration of SO<sub>2</sub> in the flue gas could be controlled to within ±10 ppm.

Table 6.1: Proximate and ultimate analysis of Indiana Coal

Analysis	% by mass
<b>Proximate Analysis %</b>	
Moisture	6.60
Volatile Matter	32.10
Fixed Carbon	53.20
Ash	8.10
<b>Ultimate Analysis % (DAF-)</b>	
Carbon	74.90
Hydrogen	4.07
Nitrogen	1.56
Oxygen	9.47
Sulfur	1.30

Table 6.2 Analysis of the Gilmore formation limestone (calcined)

Constituent	Percent by weight
SiO <sub>2</sub>	2.02
Al <sub>2</sub> O <sub>3</sub>	1.04
Fe <sub>2</sub> O <sub>3</sub>	0.41
MgO	2.00
CaO	93.36
Na <sub>2</sub> O	0.19
K <sub>2</sub> O	0.02
TiO <sub>2</sub>	0.05
MnO	0.01
P <sub>2</sub> O <sub>5</sub>	0.10
SO <sub>3</sub>	0.97

Experiments were carried out at both 200 and 1000 ppm inlet SO<sub>2</sub> concentrations. Twenty grams of single sized limestone were inserted in the batching port and the data recording program was turned on. The batch was introduced to the bed by opening the ball valve. Data were recorded every 0.2s until the background SO<sub>2</sub> concentration was reached.

### **6.3 Methodology for estimating characteristic devolatilization and char burnout times**

#### **6.3.1 Devolatilization time constants**

Equation 3.12 is applied to the CO<sub>2</sub> profiles in estimating devolatilization time constants. A typical CO<sub>2</sub> profile from the combustion of 5 g of 3.33 mm Indiana coal is shown in Fig. 6.1. The initial rise of the CO<sub>2</sub> signal is associated with the flow through the gas analysis system and has a time constant equal to the instrumentation lag time,  $\tau_l$ . The rise is followed by a rapid decay in the CO<sub>2</sub> concentration which is associated with the devolatilization of coal. Devolatilization time constants are thus calculated from the fast decay immediately after the maximum concentration is reached. The quantity  $[CO_2]_i$  is estimated from the CO<sub>2</sub> profile by extrapolating the decay after the maximum concentration to time  $t_o$  as shown in Fig. 6.1. The approximately constant contribution of char to the signal,  $[CO_2]_f$  is also estimated by extrapolating the char burnout signal back to time  $t_o$  (Fig. 5.1). These parameters are then used to subtract the char contribution to devolatilization,  $[CO_2]_f$  as described by Eq. 3.12. A log-linear plot of the dimensionless CO<sub>2</sub> concentration gives a straight line, the inverse negative slope of which is the time constant for devolatilization,  $\tau_v$ .

#### **6.3.2 Char burnout time constants**

Char burnout time constants can be estimated by substituting Eq. 3.20 into Eq. 3.13, linearizing the resulting expression for CO<sub>2</sub> with respect to time, and obtaining characteristic char burnout times from the CO<sub>2</sub> profile in a manner similar to that used for devolatilization

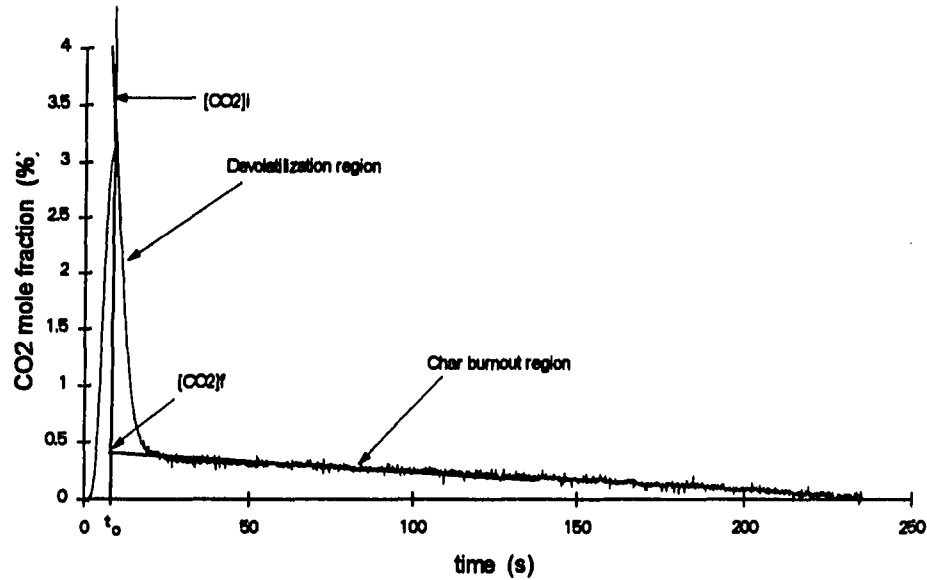


Figure 6.1: Typical CO<sub>2</sub> profile from batch test with 3.33 mm Indiana coal

analysis. This method, though successfully employed in some preliminary experiments, requires the use of relatively small coal samples to assure that the contribution of the interphase mass transfer,  $\tau_p$ , to the characteristic char burning time is small compared to other contributions; otherwise the analysis becomes very complicated. To reduce the influence of interphase time constant on  $\tau_c$  an alternative approach was used. The latter method calculates the recession in particle diameter by assuming that coal particles are spherical and burn as shrinking (constant density) spheres. In this respect, the ratio of the diameter of the particle at any time  $t$  to its initial diameter,  $d_i$ , is

$$\frac{d(t)}{d_i} = \left( \frac{m(t)}{m_i} \right), \quad (6.1)$$

where  $m(t)$  is the mass of char carbon remaining in the bed at time  $t$ , and  $m_i$  is the initial mass of carbon in the char. The quantity  $m_i$  is computed by subtracting the cumulative mass of

volatile carbon lost during devolatilization (estimated from the  $\text{CO}_2$  profile as given in Eq. 3.13) from the mass of elemental carbon in the parent coal

$$m_i = (\% \text{ carbon}) \times m_{\text{coal}} - QM_c \int_0^{\infty} \{ [\text{CO}_2]_i - [\text{CO}_2]_f \} \exp\left(-\frac{t}{\tau_v}\right) dt. \quad (6.2)$$

The quantity  $m(t)$  is calculated by subtracting the cumulative mass of carbon lost during combustion from the initial mass of carbon in the char.

$$\frac{m(t)}{m_i} = 1 - \frac{QM_c}{m_i} \int_0^t \{ [\text{CO}_2]_R - ([\text{CO}_2]_R - [\text{CO}_2]_f) \exp\left(-\frac{t}{\tau_v}\right) \} dt. \quad (6.3)$$

According to Eq. 3.20, and for times  $3\tau_v < t \ll \tau_c$ , a plot of  $\ln(d/d_i)$  versus time is a straight line with negative reciprocal slope equal to  $\tau_c$ . This alternative approach also has the advantage of reducing the noise in the analysis.

#### 6.4 Methodology for estimating time constants for calcination and sulfation

Carbon dioxide and  $\text{SO}_2$  profiles during limestone tests are shown in Figures 6.2 and 6.3 respectively. The background concentration was subtracted from the  $\text{CO}_2$  profiles.

The  $\text{CO}_2$  transient, which arises from the calcination of 0.43 mm limestone at  $850^\circ\text{C}$  and 1 m/s, is shown in Fig. 6.2. The profile, which resembles coal devolatilization, rises to a maximum and then decays in an exponential thereafter. The initial rise of the profile is attributed to the lag time of the sampling system. Also shown in Fig. 6.2 is the induction time associated with plug flow through the sampling lines. Time constants for calcination were obtained from the exponential decay immediately after the peak  $\text{CO}_2$  concentration occurs. As shown in chapter 4 the  $\text{CO}_2$  profile can be non-dimensionalized according to the equation

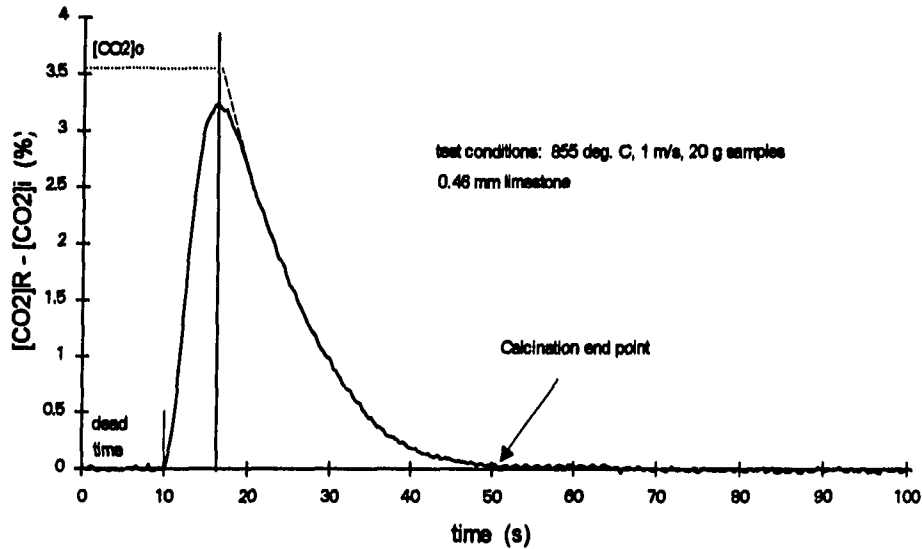


Figure 6.2: CO<sub>2</sub> traces from batch tests with 0.46 and 2.18 mm limestone

$$\frac{[CO_2]_R - [CO_2]_i}{[CO_2]_o - [CO_2]_i} = \exp\left(-\frac{t}{\tau_c}\right), \quad (6.4)$$

where  $[CO_2]_o$  is estimated from the CO<sub>2</sub> profile as shown in Fig. 6.2. Therefore, a semi-log plot of the dimensionless CO<sub>2</sub> concentration in Eq. 6.4 yields a straight line the inverse negative slope of which is equal to the calcination time constant,  $\tau_c$ .

The extend of calcination was estimated by integrating the CO<sub>2</sub> profiles and then comparing the actual moles of CO<sub>2</sub> evolved to the theoretical amount of CO<sub>2</sub> expected to evolve from the batched limestone

$$\% \text{ theoretical CO}_2 \text{ released} = \frac{y_c m_L}{M_L}. \quad (6.5)$$

Therefore, the % extend of calcination of limestone is defined as

$$\% \text{ Extend of calcination} = Q \frac{\int_0^{\infty} \{[CO_2]_R - [CO_2]_i\} dt}{y_c m_L / M_L}, \quad (6.6)$$

where  $y_c$  is the mass fraction of  $CaCO_3$  in the sample.

A typical sulfur dioxide profile is plotted in Fig. 6.3 for 0.46 limestone at 1 m/s and 850 °C. The profile drops rapidly to a minimum of  $[SO_2]_o$ , and rises exponentially to background thereafter. Time constants were estimated after calcination was over for each particle size. The calcination end point was estimated at the time when the  $CO_2$  profile returns to background as illustrated in Fig. 6.2. As shown in Chapter 4, for short times and chemistry rate limited sulfation, the  $SO_2$  concentration can be expressed as

$$\frac{[SO_2]_R - [SO_2]_i}{[SO_2]_o - [SO_2]_i} = \exp\left(-\frac{t}{\tau_s}\right), \quad (6.7)$$

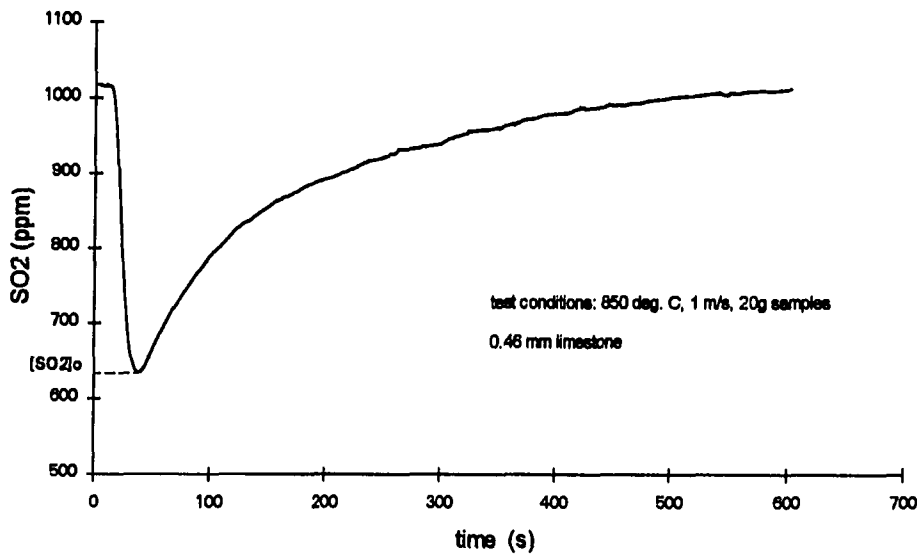


Figure 6.3:  $SO_2$  profile for 0.46 mm limestone

where  $[SO_2]_o$  is estimated from the  $SO_2$  profiles as the minimum  $SO_2$  concentration as illustrated in Fig. 6.3. A semi-log plot of the dimensionless  $SO_2$  concentration versus time yields a straight line with inverse negative slope equal to the time constant for sulfation  $\tau_s$ . Extent of sulfation was estimated by integrating the net profile  $[SO_2]_i - [SO_2]_R$ . The integral gives the actual moles of  $SO_2$  absorbed during sulfation. The result was then divided into the theoretical absorbed  $SO_2$  (found from the sulfation reaction) to estimate the percent  $SO_2$  absorption by limestone. Since one mole of  $CaCO_3$  absorbs one mole of  $SO_2$ , it is expected that the theoretical moles of absorbed  $SO_2$  will be

$$\text{theoretical } SO_2 \text{ absorbed} = \frac{y_c m_L}{M_L} \quad (6.8)$$

Thus, the percent sulfur dioxide absorbed may be defined as

$$\%SO_2 \text{ absorbed} = Q \frac{\int_0^{\infty} \{ [SO_2]_i - [SO_2]_R \} dt}{y_c m_L / M_L}. \quad (6.9)$$

## 7. RESULTS AND DISCUSSION FOR COAL BATCH TESTS

### 7.1 Devolatilization

As described in chapter 3, some researchers [2,5] suggest that char combustion does not begin until devolatilization is complete. They base this assumption on the premise that oxygen cannot diffuse to the particle while volatiles are being expelled. On the other hand, analysis in this work assumes that devolatilization and char combustion occur simultaneously. These two possibilities were investigated by comparing CO traces to CO<sub>2</sub> traces produced during batch tests. Figure 7.1 shows the transience in CO emissions to occur simultaneously with the sharp devolatilization peak of the CO<sub>2</sub> emissions. Accordingly, CO emissions can be described by the same first-order differential equation used to describe CO<sub>2</sub> released during devolatilization (CO can either be a primary product of devolatilization or a secondary

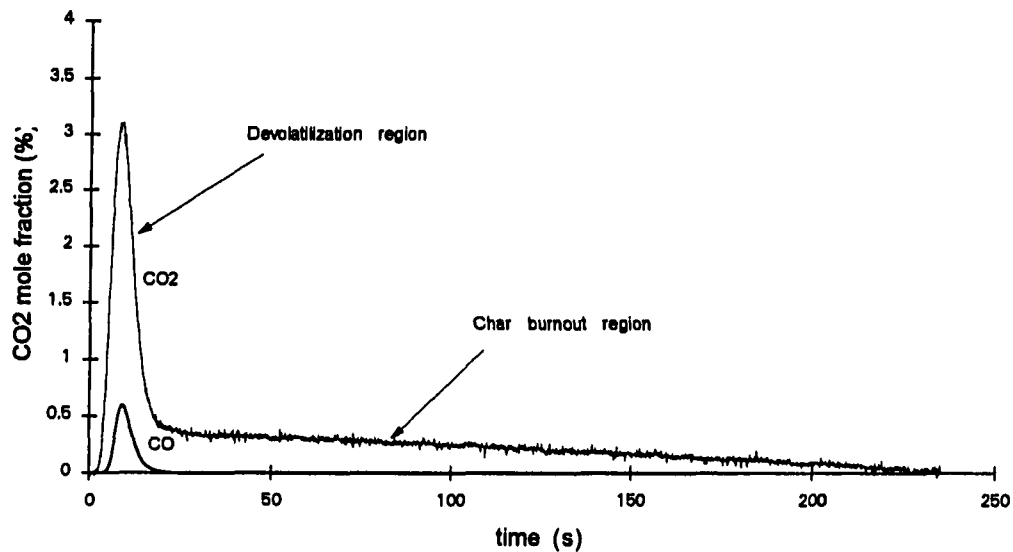


Figure 7.1: CO<sub>2</sub> and CO profiles from combustion of 3.33 mm Indiana coal

product via a fast chemical reaction). Since char burning does not contribute to the CO signal,  $[CO]_f$  is zero and the model for CO emissions becomes

$$[CO] = [CO]_i \exp\left(-\frac{t}{\tau_v}\right) \quad (7.1)$$

For a given batch test, time constants obtained from the CO profiles with the model in Eq. 7.1 agree with devolatilization time constants,  $\tau_v$ , obtained from CO<sub>2</sub> traces if simultaneous devolatilization and char burning are assumed; i.e. if Eq. 3.12 is used. If  $[CO_2]_f$  is assumed to be zero in Eq. 3.12, which would be the case if char does not burn during devolatilization, the time constants obtained from the CO and CO<sub>2</sub> traces do not agree. Based on this observation, devolatilization and char burnout are believed to occur simultaneously.

The next series of tests evaluated the particle size dependence of devolatilization time. Figure 7.2 is a plot of total devolatilization times,  $t_v = 3 \tau_v$ , for the Indiana coal as a function of the initial particle diameter in the range of 1 to 6.2 mm. Also shown are the devolatilization laws obtained by Essenhigh [1] and Ragland and Weiss [2]. The devolatilization data obtained from this work for particles larger than 3 mm agree closely with Essenhigh's [1] "d-squared" law but are 6-40% larger than the Ragland and Weiss [2] relationship. The relationship determined between devolatilization time and particle size was  $t_v = 0.96d_i^2$  (correlation coefficient of 0.91 and a standard error of coefficient equal to  $\pm 0.04 \text{ s/mm}^2$ ). Since coal rank does not significantly affect the dependence of devolatilization time on the initial particle size [1,2], the differences observed between the obtained  $t_v$  values and the Ragland and Weiss [2] relationship may be attributed to differences in coal particle shape. Ragland and Weiss [2] used spherical coal particles which they filed out of crushed coal particles. Essenhigh's [1] experiments and this work used particles that were produced by crushing and screening the parent coal. These particles resembled cubes or wedges. Differences in particle shape affect the Sherwood number of the particle which influences the mass transfer of

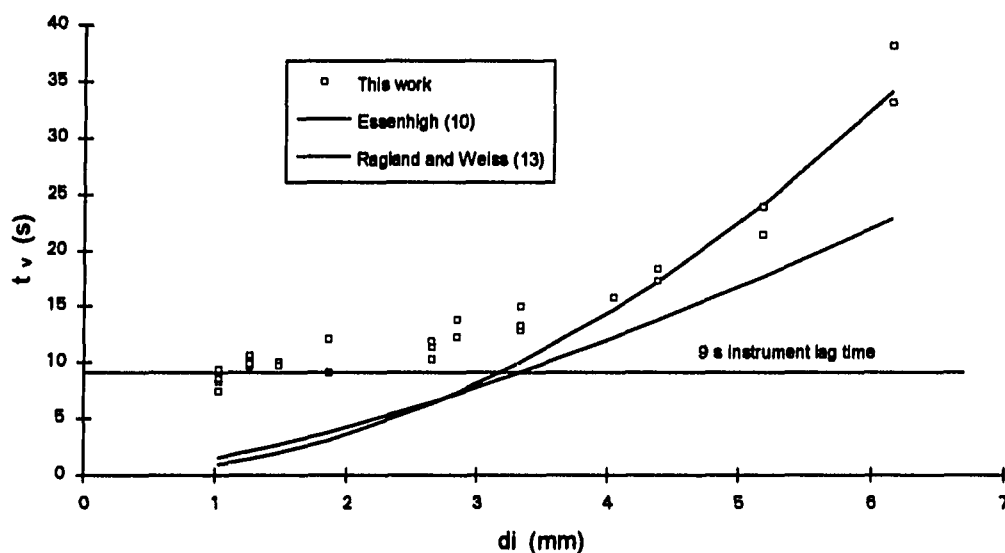


Figure 7.2: Total devolatilization times vs. initial particle diameter for Indiana coal

volatile matter from the particle to the bed, thus altering the power law dependence of devolatilization on particle size.

The discrepancies observed in Fig 7.2 for particles smaller than 3 mm are artifacts of the gas sampling system and are expected whenever devolatilization time constants are comparable or smaller than the lag time of the sampling system. As noted in chapter 4, the sampling system embodies extensive filtering prior to introducing the flue gas to the analyzers. The combustor and sampling system can be modeled as two CSTRs in series having a combined time constant  $\tau_f$ . The plug flow through the sampling line, associated with a dead time observed at the beginning of the signal, does not affect the analysis. The net response of the system at the gas analyzers during coal devolatilization is described by

$$\frac{[CO_2]_A - [CO_2]_f}{[CO_2]_i - [CO_2]_f} = \frac{\exp\left(-\frac{t}{\tau_v}\right) - \exp\left(-\frac{t}{\tau_f}\right)}{1 - \frac{\tau_f}{\tau_v}}, \quad (7.2)$$

where  $[CO_2]_A$  is the  $CO_2$  concentration measured at the gas analyzers. Step tests on the gas sampling system using  $CO_2$  as a tracer gas showed that it behaved as a first-order system with characteristic lag time,  $\tau_f$ , equal to 3.0 s. Similar tests on the analyzers alone showed that their lag times are much smaller than  $\tau_f$  (refer to chapter 3, page 2 for additional information on instrumentation lag time).

Assuming that  $\tau_v > \tau_f$ , a semi-logarithmic plot of non-dimensionalized  $CO_2$  concentration (Eq. 3.13) versus time will give a straight line with slope equal to the reciprocal of  $\tau_v$ . This is evident in Fig. 7.2 for particles larger than 3 mm. Smaller particles, on the other hand, have  $\tau_f > \tau_v$ , thus yielding a time constant closer to  $\tau_f$  than  $\tau_v$ . Figure 7.2 shows measured devolatilization times for particles smaller than 3 mm converging to  $3\tau_f$ . To measure devolatilization time constants smaller than  $\tau_f$  the use of a gas analysis system with lag time somewhat smaller than available for the present experiments would be required.

## 7.2 Char burnout

Char burnout is significantly slower than devolatilization. A number of researchers [1,2,3,11,15,16] have shown that char burnout is also a strong function of the initial particle size. Furthermore, Eqs. 3.19 and 3.21 developed using the methodology introduced in this work, suggest that char burnout time and characteristic char burnout time are strong functions of the initial coal particle size.

Characteristic char burnout times,  $\tau_c$ , were measured as a function of initial particle diameter for 5g coal batches burned in a bed heated with propane to  $850 \pm 10$  °C and a bed velocity of 1 m/s. The data was interpreted by preparing a plot of  $\log(\tau_c - \tau_i)$  vs.  $\log d_i$  as shown in Fig. 7.3. The time constant  $\tau_c - \tau_i$  is referred to as normalized time. The interphase time constant,  $\tau_i$ , was determined from Eqs. 3.21 and 3.22 by plotting  $\tau_c$  vs. initial mass of carbon in the coal batch,  $m_i$ , for a given particle diameter [3]. The plot also contains normalized

burnout times,  $t_c - t_i$ , where  $t_c$  is the time the transient  $\text{CO}_2$  signal disappeared into the steady-state background  $\text{CO}_2$  signal and  $t_i$  is the contribution of the interphase mass transfer (bubble to emulsion) of oxygen. The constant  $t_i$  is estimated in a similar manner as  $\tau_i$ . Although the magnitudes of  $\tau_c - \tau_i$  and  $t_c - t_i$  from a particular test are expected to be different, the dependence on initial particle size is expected to be the same, according to Eqs. 3.19 and 3.21.

For the range of particles tested (0.6 - 6 mm), the slope of the lines in Fig 7.3 is expected to be 2 (mass transfer limited kinetics as shown in Table 3.1) or at least 1.5, which is typical of mass transfer limited combustion with variable Sherwood number. Instead, the plot of  $\log(\tau_c - \tau_i)$  vs  $\log d_i$  gave a slope of  $1.320 \pm 0.038$  (correlation coefficient of 0.983). The normalized burnout time,  $t_c - t_i$ , data gave a slope of  $1.310 \pm 0.051$  (correlation coefficient was 0.975), except for the largest particles which displayed a much smaller slope. The large

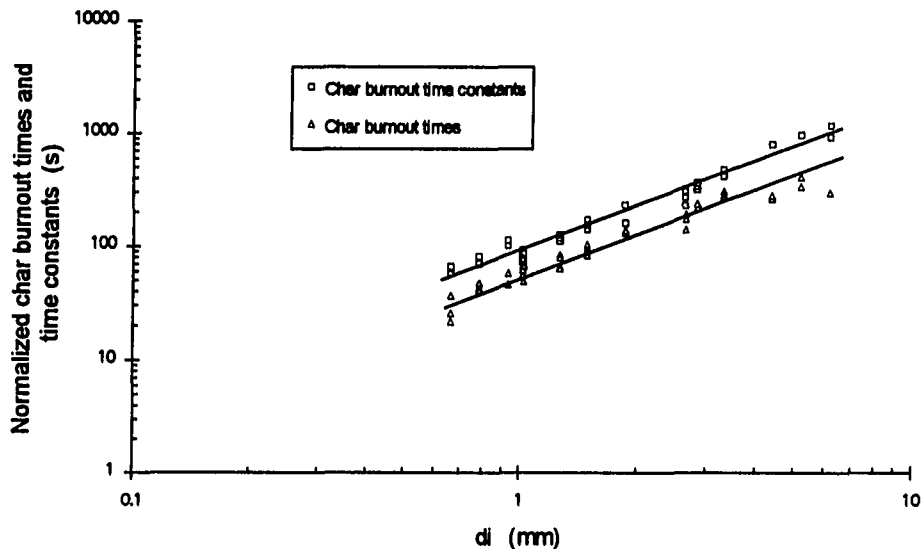


Figure 7.3: Char burnout times and time constants vs initial particle diameter

particle behavior may be attributed to the inability to estimate  $t_c$  from the weak, residual signal generated from large, slow-burning particles as burnout was approached. The agreement between  $\tau_c$  and  $t_c$  data for smaller particles signifies that the methodology developed for this study was sound but the coal was behaving in an unexpected manner.

A number of hypotheses were made in order to explain the behavior of the Indiana bituminous coal under investigation. The first hypothesis was that the char burning process was controlled by chemical kinetics. Pillai [11] and Basu [16], who also observed char burning time - initial particle diameter power laws between 1 and 2, attributed this behavior on the combined effects of chemical kinetics and mass transfer. To test this hypothesis, apparent activation energies for char burning were measured by varying the bed temperature at which the batch tests were performed for a single particle size. Table 7.1 shows the results from 1.55 mm Indiana coal tests. If the char burnout was controlled by chemical kinetics, the activation

Table 7.1 Variable temperature tests with 1.55 mm Indiana coal

Test	Temperature (K)	$\tau_c$ (s)	$t_c$ (s)
BTa1	1039	130	93
BTa2	1049	128	104
BTa3	1082	155	109
BTa4	1100	156	106
BTa5	1143	185	120

energy is expected to be close to 40 kcal/mol. However, a semi-logarithmic plot of  $1/(\tau_c - \tau_i)$  vs. reciprocal bed temperature, shown in Fig. 7.4 yielded an apparent activation energy of  $-5.5 \pm 2.6$  kcal/mol (correlation coefficient equal to 0.82). Also shown in Fig 7.4 is a semi-logarithmic plot of  $1/(t_c - t_i)$  vs.  $1/T$  which yielded an apparent activation energy of  $-0.076 \pm 0.5$  kcal/mol (correlation coefficient of 0.81). The near zero activation energies measured

from these tests suggest that the burning of char is controlled by mass transfer of oxygen to the particle and not by chemical kinetics.

Further evidence that mass transfer is rate limiting in the combustion of char is found in the ratio of  $(t_c - t_i) / (\tau_c - \tau_i)$  shown in Table 7.2. As shown in Table 3.1, a ratio approaching unity is expected if chemical kinetics is rate limiting. Most tests in Table 7.2 show ratios between 0.5 and 0.66, as expected for mass transfer limited reaction. The lower ratios observed in Table 7.2 for particles larger than 3.33 mm are evidence of the fact that burnout times,  $t_c$ , cannot be accurately measured due to the weak  $\text{CO}_2$  signal as burnout is approached.

A second hypothesis was that primary fragmentation [1,2,12,14,17,30] is responsible for the smaller than expected exponent. This hypothesis was developed from an analysis on the burnout time of fragmented particles. Assuming that fragmentation produces  $N_f$  spherical fragments, the diameter of the fragmented particles is related to the initial particle diameter by

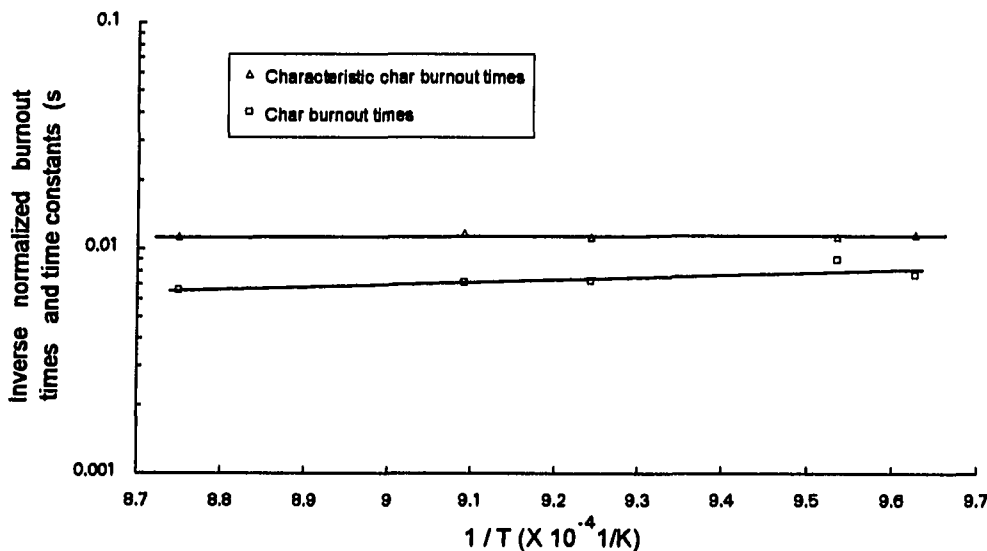


Figure 7.4: Variable temperature tests with 1.55 mm Indiana coal.

$$\frac{d_f}{d_i} = \left( \frac{1}{N_f} \right)^{\frac{1}{3}} \quad (7.3)$$

This formulation, although an oversimplification of the actual fragmentation process, is nevertheless consistent with experimental results of Chirone et al. [14] and Ragland and Pecson [17]. Furthermore, the number of fragments is expected to increase with particle size [1,14].

Chirone et al. [14] report a near linear dependence of  $N_f$  on initial particle size

$$N_f \propto d_i \quad (7.4)$$

Substituting Eq. 7.4 into Eq. 7.3 yields

Table 7.2 Ratios of time constants

$d_i$ (mm)	$t_c - t_i$ (s)	$\tau_c - \tau_i$ (s)	$(t_c - t_i)/(\tau_c - \tau_i)$
0.66	28	66	0.42
0.78	43	75	0.57
0.93	53	109	0.49
1.02	63	80	0.79
1.26	74	119	0.62
1.48	95	154	0.62
1.86	137	194	0.71
2.65	171	271	0.63
2.84	268	339	0.79
3.33	290	452	0.64
4.38	276	801	0.34
5.18	378	969	0.39
6.15	269	930	0.29

$$d_f \propto d_i^{\frac{2}{3}} \quad (7.5)$$

Mass transfer limited char combustion with constant Sherwood number predicts that the characteristic char burnout time increases with the square of the fragmented particle diameter

$$\tau_c \propto d_f^2 \quad (7.6)$$

Substituting Eq. 7.5 into Eq. 7.6 yields the apparent power law due to burning of coal fragments

$$\tau_c \propto d_i^{\frac{3}{4}} \equiv d_i^{1.33} \quad (7.7)$$

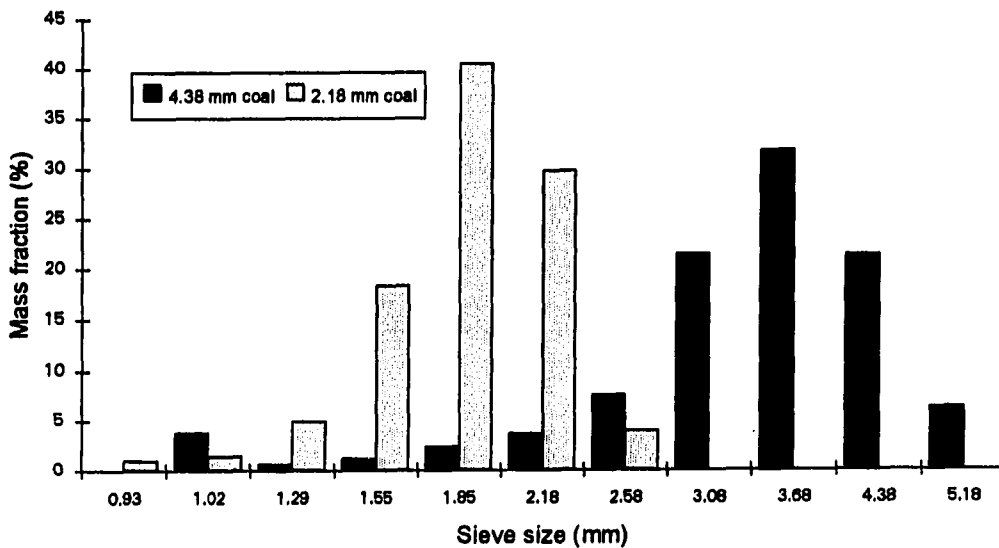


Figure 7.5: Size distribution of fragments from quench tests with Indiana coal

This dependence is very close to that measured experimentally and gives an indication as to how fragmentation affects the dependence of burnout time on initial particle size. The experimental results are in good agreement with the fragmentation theory.

To test the fragmentation hypothesis, char fragments were recovered 20-25 s after batching coal samples to the fluidized bed. The size distribution of the fragments was compared with the original distribution of the charge. During this test, 40 g of 2.18 mm Indiana coal were batched into the bed, which was heated with propane gas at around 1116 K and 1 m/s. After devolatilization was over (~ 20-25 s), air and propane were shut off and a small flow of nitrogen gas was introduced to quench the combustion. The char that remained in the bed was then recovered and sieved to obtain the size distribution of char fragments. As Fig. 7.5 illustrates, the 2.18 mm-dia. coal produces a large number of fragments during devolatilization. The average size of fragments was estimated to be 1.81 mm, which is around 84% of the original diameter of coal particles. A second quench test with 50 g of 4.38 mm coal produced fragments that had average size close to 3.07 mm (around 70% of the original size) and a much wider size distribution (Fig. 7.5). These tests verify that significant fragmentation occurs and that the extent of fragmentation increases with particle diameter. These observations are in accordance with the experimental data of Chirone et. al. [14] and Ragland and Pecson [17].

The tests carried out in this work showed that, for Indiana bituminous coal of size 0.6 to 6 mm, both the release of volatiles and char combustion are controlled by mass transfer across the film surrounding the coal particle. Primary fragmentation of char particles during the release of volatiles results in a lower than expected power law dependence of burnout times on initial particle size.

## **8. RESULTS AND DISCUSSION FOR SULFUR SORPTION**

Limestone batch tests focused on estimating activation energies for calcination and sulfation as well as investigating the effect of particle size on calcination and sulfation time constants. Tests to estimate activation energies were carried out at four different temperatures using three particle sizes for each temperature. Variation of time constants, extent of calcination, and extent of sulfation with particle size were investigated at 850 °C. All tests were carried out at 1 m/s bed velocity and under simulated coal combustion conditions. The bed was heated with natural gas and SO<sub>2</sub> was injected in the main air stream via a metering valve. The background SO<sub>2</sub> level was kept at 1000 ppm (except when otherwise noted). This condition was deduced after analysis of the model in chapter 4 showed that lower background SO<sub>2</sub> concentrations resulted in depletion of SO<sub>2</sub> in the emulsion phase and complicated the analysis because of the introduction of a characteristic interphase time analogous to the depletion of emulsion phase in O<sub>2</sub> during char combustion.

### **8.1 Investigating the effect of inlet SO<sub>2</sub> conditions**

The goal of this set of experiments was to investigate the effect of inlet SO<sub>2</sub> conditions on the extent of limestone calcination, sulfation, and the characteristic times involved in the two processes. Tests were carried out with 1 mm limestone at 854 °C and two inlet SO<sub>2</sub> conditions: 200 ppm and 1000 ppm.

#### **8.1.1 Extents of calcination and sulfation**

The extent of calcination and extent of sulfation for different limestone sample masses are listed in Table 8.1. The tests show anywhere from 85 to 100% of the limestone is calcined regardless of inlet SO<sub>2</sub> conditions. Changes in inlet SO<sub>2</sub> level result in a slight increase in limestone calcination as SO<sub>2</sub> is increased from 200 ppm to 1000 ppm. Values for

**Table 8.1 Variation of extents of calcination and sulfation and time constants with sample mass and inlet SO<sub>2</sub> conditions**

<b>Test</b>	<b>Inlet SO<sub>2</sub> (ppm)</b>	<b>Limest. Mass (g)</b>	<b>Extent of calcination (%)</b>	<b>Extent of sulfation (%)</b>	<b><math>\tau_c</math> (s)</b>	<b><math>\tau_s</math> (s)</b>
limvma2	200	10	79	0.77	21.3	104.4
limvma3	200	15	90	1.62	21.8	217
limvma4	200	20	91	1.62	21.8	263.4
limvma5	200	25	90	1.84	22.3	316.7
limvma6	200	30	90	2.03	21.3	370.6
limvma7	200	35	86	1.61	21.9	418.6
limvmb1	1000	5	99	5.46	17.52	104.1
limvmb2	1000	10	99	4.34	17.23	108.2
limvmb3	1000	15	96	5.87	19.28	127.3
limvmb4	1000	20	96	5.75	20.09	121.8
limvmb5	1000	25	98	7	19.69	147

the extent of sulfation are much lower compared to what other researchers have reported [20,22-25]. This suggests that either the limestone batched in the bed is not well utilized under these conditions, or that the weak SO<sub>2</sub> signal toward the end of the profile could not be accurately measured by the instruments, thus resulting in calculation errors. This case is similar to char combustion where the weak CO<sub>2</sub> signal, produced as burnout is approached, is lost in the background noise.

The inlet concentration of SO<sub>2</sub> has a considerable effect on the degree of sulfation. Increasing the inlet concentration increases the degree of sulfation. It is hypothesized that the lower inlet concentrations may result in depletion of SO<sub>2</sub> in the emulsion phase. In such an event, diffusion between emulsion and bubble becomes important, thus the utilization of limestone is reduced. This hypothesis is further investigated in the next section where the effect of sample mass on the characteristic times is investigated.

### 8.1.2 Characteristic times for calcination and sulfation

Characteristic times for calcination for the two inlet conditions are plotted against sample mass in Fig. 8.1. Little effect of inlet  $\text{SO}_2$  conditions on calcination time constants is evident. Tests with 200 ppm  $\text{SO}_2$  at the inlet exhibit slightly lower characteristic calcination times compared to tests with 1000 ppm inlet  $\text{SO}_2$ . This result may be due to the higher initial sulfation rates, which consume the produced  $\text{CaO}$ , thus shifting the equilibrium of the calcination reaction



toward producing more  $\text{CaO}$ .

For a particular sample mass, the characteristic time for sulfation is doubled as the inlet  $\text{SO}_2$  concentration is reduced from 1000 ppm to 200 ppm, with the exception of tests with 10

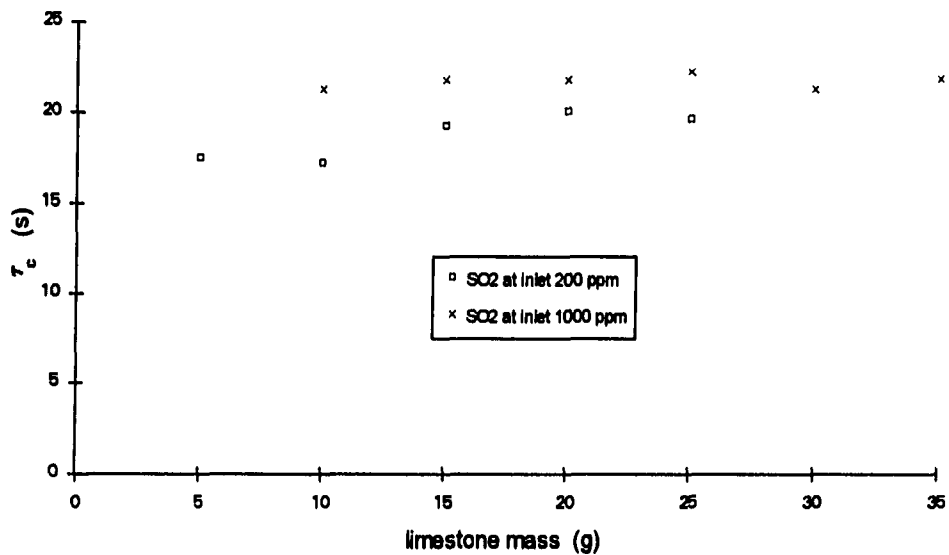


Figure 8.1: Calcination time constants vs. sample mass for 1 mm limestone particles

of limestone where the  $\text{SO}_2$  signal is weak and the calculation of the time constant is prone to large errors. Evidently, the higher inlet  $\text{SO}_2$  conditions favor faster sulfation of the sorbent. In addition, interphase mass transport time for 1000 ppm  $\text{SO}_2$  is significantly smaller compared to 200 ppm  $\text{SO}_2$ . This observation becomes evident from the pronounced dependence of characteristic times on sample mass when inlet  $\text{SO}_2$  is held at 200 ppm (see Fig. 8.2).

## 8.2 The effect of sample mass

### 8.2.1 Extents of calcination and sulfation

As seen in Table 8.1, for a particular inlet condition, the extent of calcination and sulfation of limestone remain virtually unchanged except a test at 10 g and 200 ppm which exhibited slightly lower extent sulfation and a test at 25 g and 1000 ppm where the degree of sulfation was somewhat higher than expected. Small limestone batches produce weak, noisy

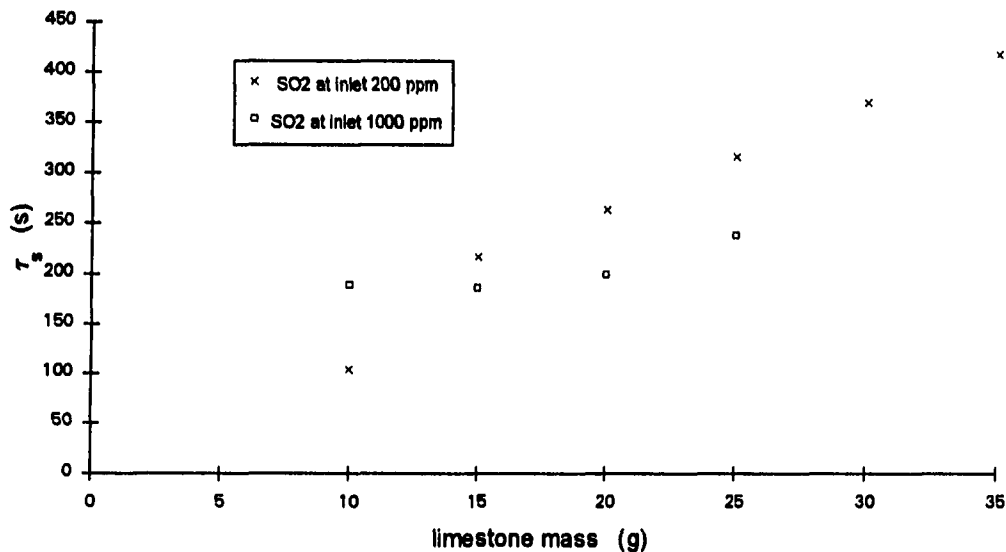


Figure 8.2: Sulfation time constants vs. mass for 1 mm limestone particles

SO<sub>2</sub> transients which result in large computation errors. On the other hand, large batches of limestone may be utilized more effectively due to the higher bulk density of the material in the bed, which result in better material mixing and a better possibility that a limestone particle is sulfated.

### 8.2.2 Characteristic times for calcination and sulfation

A plot of the time constant for calcination vs. sample mass for the two inlet SO<sub>2</sub> concentrations (200 ppm and 1000 ppm) is shown in Fig. 8.1. The smaller time constants observed with 200 ppm SO<sub>2</sub> compared to 1000 ppm SO<sub>2</sub> suggest that calcination is somewhat slower at the lower SO<sub>2</sub> inlet conditions. No significant change in calcination time constant with limestone mass is observed with either inlet SO<sub>2</sub> concentration.

Time constants for sulfation are plotted against limestone batch mass in Fig. 8.2. At 200 ppm inlet SO<sub>2</sub> there is a significant variation of the sulfation time constant with sample mass, indicating that the contribution of interphase mass transport to sulfation time constant is significant due to depletion of SO<sub>2</sub> in the emulsion. Consequently, the analysis of the time constants becomes more complicated. This case is analogous to the depletion of O<sub>2</sub> during char combustion, which introduces an interphase mass transport time to the analysis of char burnout times. No significant variation in the time constant for sulfation,  $\tau_s$ , with limestone mass is observed for the 1000 ppm tests, indicating that the SO<sub>2</sub> in the emulsion is not depleted. As the batch mass becomes larger than 25 g, however, the characteristic sulfation time increases (Fig. 8.2). This means that depletion of SO<sub>2</sub> in the emulsion may become significant, and the contribution of interphase mass transport from bubble to emulsion to the sulfation time constant is substantial. Based on this premise, variable particle size and variable temperature tests were carried with limestone samples of 20 g and inlet SO<sub>2</sub> around 1000 ppm.

### 8.3 Effect of bed temperature

The objective of these tests was to investigate the variation in the extent of calcination and sulfation with temperature for each particle size and to estimate activation energies for calcination and sulfation from the respective time constants. Variable temperature tests were carried out with 20 g samples of 0.46, 0.66, and 0.92 mm limestone at five different temperatures for each particle size. The fluidization velocity was kept at 1 m/s for all tests. Table 8.2 lists the extents of calcination and sulfation for each particle size at test temperatures.

#### 8.3.1 Extents of calcination and sulfation

There is no significant variation in the extent of calcination with temperature or particle size, except for one extraneous case with 0.46 mm particles at 740 °C which produced more CO<sub>2</sub> than other cases. However, at low temperatures (730-750 °C), the calcination rate is significantly reduced. In fact, the CO<sub>2</sub> signal becomes so weak that is lost in the background noise. Uncertainties in estimating the amount of CO<sub>2</sub> produced at the low temperature tests resulted in the unavailable data for extent of calcination in Table 8.2 for tests limtc2 and limvtc3.

The extent of sulfation is expected to be a strong function of temperature as shown by several researchers [20, 22-24]. The optimum temperature for sulfation of limestone is expected to be around 850 °C [20, 22-25]. This optimum temperature is best explained by the increased particle porosity occurring due to the higher extent of calcination at the higher temperatures [25]. At temperatures in excess of 850 °C, sulfation becomes fast enough to occur at the pore mouths before significant diffusion has taken place and the extent of sulfation is expected to decrease. There is, however, variation in the optimum sulfation temperature depending on the reactor type, operating conditions, and limestone characteristics.

A plot of the extent of sulfation vs. bed temperature is shown in Fig. 8.3. The trends are the same for all three particles. There is a marked increase in the extent of sulfation for as temperature increases from 720 to 800 °C. The extent of sulfation drops to a minimum at

Table 8.2 Variation of extent of calcination and sulfation with temperature

Particle size (mm)	Test	Bed temp. (°C)	Extent of calcination	Extent of sulfation
0.46	limvtd1	904	79	13.6
	limvt1	857	77	9.9
	limvta1	815	80	9.9
	lmvtb1	787	80	11.5
	limvtc1	740	94	9.1
0.66	limvtd3	908	80	10.6
	limvt2	857	86	6.2
	limvta2	820	74	9.6
	limvtb2	784	84	8.6
	limvtc2	735	N/A	5.9
0.92	limvtd3	910	80	8.1
	limvt3	854	81	5.4
	limvta3	820	78	6.2
	lmvtb3	778	80	5.8
	limvtc3	733	N/A	3.7

around 870 °C and increases thereafter. This result is in disagreement with a number of researchers [20,23-25] who observed that limestone utilization decreases monotonically at temperatures in excess of 850 °C.

It is hypothesized that the initial increase in sulfation extent is due to increase in internal particle area due to faster sulfation, which results in higher utilization of the stone. At temperatures higher than 800-820 °C, sulfation is fast enough to occur before SO<sub>2</sub> has diffused into the particle, thus plugging the pores and reducing the extent of sulfation. After 870 °C, CaSO<sub>4</sub>, which is deposited at the pore mouths, begins to dissociate according to the reaction

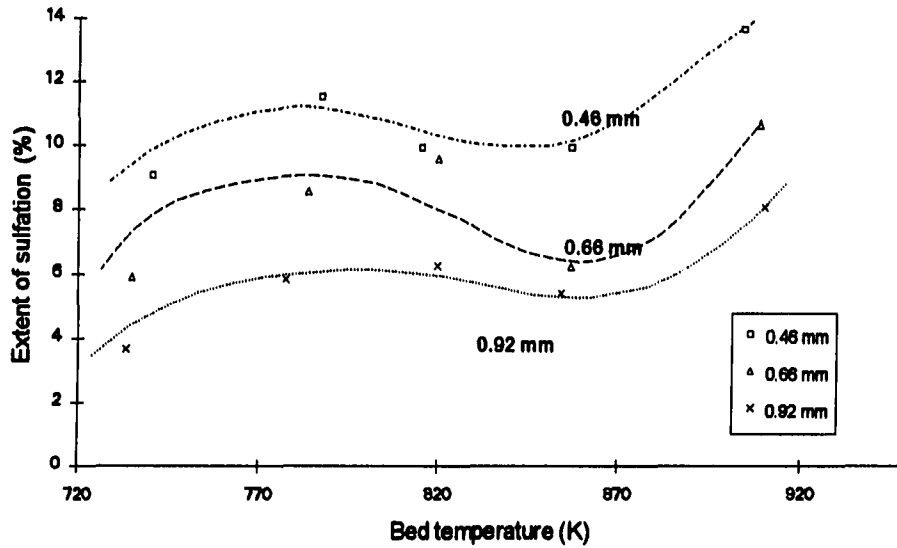
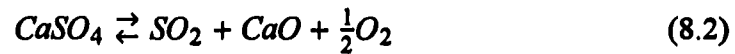


Figure 8.3: Variation of extent of sulfation with temperature



The dissociation of  $\text{CaSO}_4$  reopens the pore mouths, thus making more internal area available to sulfation. This results in a markedly increase in limestone utilization.

### 8.3.2 Activation energies

#### a. Calcination

The time constant for chemically controlled calcination is defined as

$$\tau_c \equiv \frac{\rho L^2 p}{2k_c M_L} \quad (8.3)$$

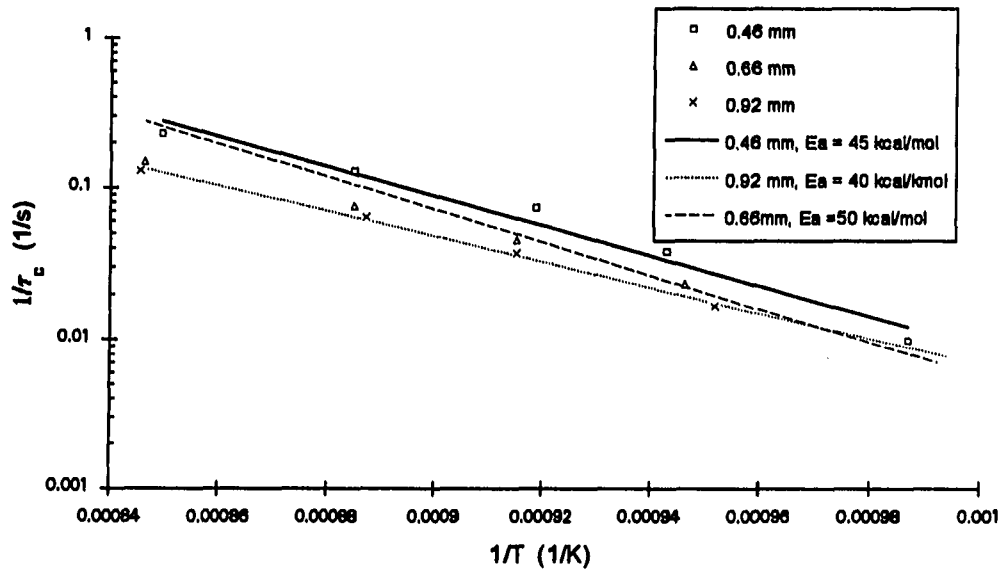


Figure 8.4: Activation energies for calcination

According to Eq. 8.3, the time constant for calcination is inversely proportional to the reaction rate constant  $k_c$ . Based on this observation, a plot of inverse characteristic calcination time vs. inverse absolute bed temperature is expected to yield a large activation energy, which is indicative of chemically controlled reactions. A plot of inverse calcination time constants vs. inverse absolute bed temperature on a log-linear scale for the three particle sizes is shown in Fig 8.4. The average apparent activation energy for calcination is estimated to be  $45 \pm 5$  kcal/mol with little variation for different particle sizes. This result is in good agreement with Borgwardt [31] who estimated activation energies for calcination of 1-10  $\mu\text{m}$  of 48-49 kcal/mol and Powell and Searcy [32] who also estimated apparent activation energies for calcination of  $49 \pm 3$  kcal/mol. On the other hand, the apparent activation energy for calcination obtained in this work is somewhat higher than the 36 kcal/mol obtained by Mulligan et. al. [4] for 212-150  $\mu\text{m}$  limestone in a thermogravimetric balance. It is well known that mass transfer limited processes are not activated ( $E_a = 0$ ) and that pore diffusion limited processes are characterized by reduced activation energies (1/2 to 1/4 of the actual value) [27]. The large

activation energies observed for calcination are indicative of a chemical kinetics limited process. This finding is further justified by data in section 8.4.

### b. Sulfation

The temperature dependence of sulfation time constants varies considerably according to the rate controlling regime. The time constant for chemically controlled sulfation is defined by

$$\tau_s = r_g \frac{\rho_g}{2\eta_s k_s M_A [SO_2]_i} \quad (8.4)$$

and is a function of the sulfation rate constant,  $k_s$ . In the case that product layer diffusion is rate limiting, the time constant becomes

$$\tau_s = r_g^2 \frac{\rho_g}{4\eta_s D_{pl} M_A [SO_2]_i}, \quad (8.5)$$

which, is a function of the product layer diffusion coefficient,  $D_{pl}$ . Simmons and Garman [33] and Bhatia and Perlmutter [34] determined that the activation energy for chemistry rate limited sulfation is of the order of 13-14 kcal/mol, whereas the activation energy for the product layer diffusion limited process is close to 30 kcal/mol. Other researchers estimated activation energies for product layer limited sulfation in the range of 33-53 kcal/mol [4,31,35]. It is, therefore expected to see a small activation energy if sulfation is chemically controlled, or a large activation energy if the reaction is controlled by diffusion through the product layer.

If pore diffusion is rate limiting, the time constant  $\tau_s$  is equal to twice the time constant for pore plugging,  $\tau_p$ , which is derived from the exponential decay of the pore diffusion coefficient. Then, the activation energy measured from the tests will be associated with the pore plugging constant according to the Arrhenius expression [28]

$$\frac{1}{\tau_p} = \frac{1}{\tau_{po}} \exp\left(-\frac{E_{ap}}{RT}\right). \quad (8.6)$$

Activation energies for sulfation were estimated by plotting inverse sulfation time constants ( $1/\tau_s$ ) vs. inverse bed temperature on a log-linear scale as shown in Fig. 8.4. An average apparent activation energy of  $14 \pm 2$  kcal/mol was obtained from these tests. The variation of activation energies between particle sizes was relatively small, but more variation may be expected for smaller particles as chemistry and/or product layer diffusion become rate limiting.

This activation energy is in agreement with the 13-14 kcal/mol quoted by Bhatia and Perlmutter [34] for chemically controlled sulfation. On the other hand, the sulfation activation energy estimated in this work contradicts activation energy values of 33-53 kcal/mol estimated by Mulligan et al. [4], Borgwardt [31] for product layer diffusion limited sulfation of small limestone particles (15-100  $\mu\text{m}$ ).

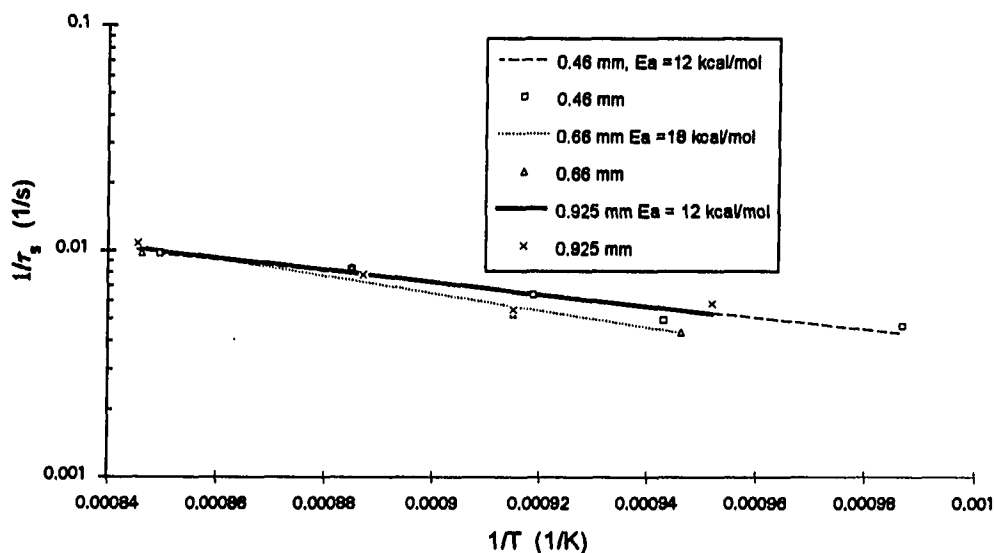


Figure 8.4: Activation energies for sulfation

Pore diffusion limited sulfation may also produce small activation energies. This observation is made under the hypothesis that sulfation of limestone may initially be controlled by chemistry. When a thin layer of product has been deposited on the grains, the reaction control will shift to product layer diffusion. As the product layer builds in the pores, though, pore diffusion becomes rate limiting and the apparent activation energy is expected to be anywhere from 1/4 to 1/2 of the activation energy of the already controlling process [27]. In this case the apparent activation energy is believed to be 1/4 to 1/2 of the value for product layer diffusion. This result is derived from pore diffusion limited catalytic reactions where, depending on the pore structure, the activation energy may be reduced by as much as 1/4 of the value for the surface reaction [27].

Accordingly, the activation energy of 14 kcal/mol estimated for sulfation suggests that either chemistry and/or pore diffusion may control the sulfation reaction. Distinction between these regimes can only be made by estimating the particle size dependence of the sulfation time constant.

#### **8.4 Effect of particle size**

Variable particle tests were carried out at 854 °C and 1 m/s fluidization velocity. The inlet SO<sub>2</sub> was kept at around 1000 ppm, and single sized limestone between 0.275 mm and 3.075 mm was used.

##### **8.4.1 Extents of calcination and sulfation**

Table 8.3 lists percent calcination and percent sulfation for the variable size tests. Extent of calcination fluctuates randomly and does not show any definitive variation with particle size. The slightly smaller values (72-77%) calculated for some of the 280 μm particles may be due partial elutriation of the sorbent from the bed since the maximum elutriable limestone particle size is of the order of 200 to 250 μm.

Table 8.3: Percent calcination and sulfation for variable size tests

Test	Particle size (mm)	Extent of calcination (%)	Extent of sulfation (%)
50X60a1	0.28	100	9.9
50X60a2	0.28	77	10.4
45X50a2	0.33	97	16.8
40X45a1	0.39	77	12.8
40X45a2	0.39	72	10.6
35X40a1	0.46	79	11.2
35X40a2	0.46	77	9.9
30X35a1	0.55	95	7.8
25X30a1	0.66	86	6.2
18X20a1	0.93	81	5.3
limvmb4	1.09	88	5.8
14X16a1	1.29	90	5.7
12X14a1	1.55	86	4.8
10X12a3	1.85	100	4.5
8X10a1	2.18	100	3.7
6X7a1	3.08	80	1.5

The extent of sulfation decreases with increasing particle size, either because of plugging of pores by  $\text{CaSO}_4$  or the cessation of the reaction due to product deposits on active sites. Bigger particles have more internal area most of which may become unavailable to  $\text{SO}_2$  due to plugging of pores by  $\text{CaSO}_4$  closer to the particle's outer surface. Thus, most of the particle's core is not fully utilized.

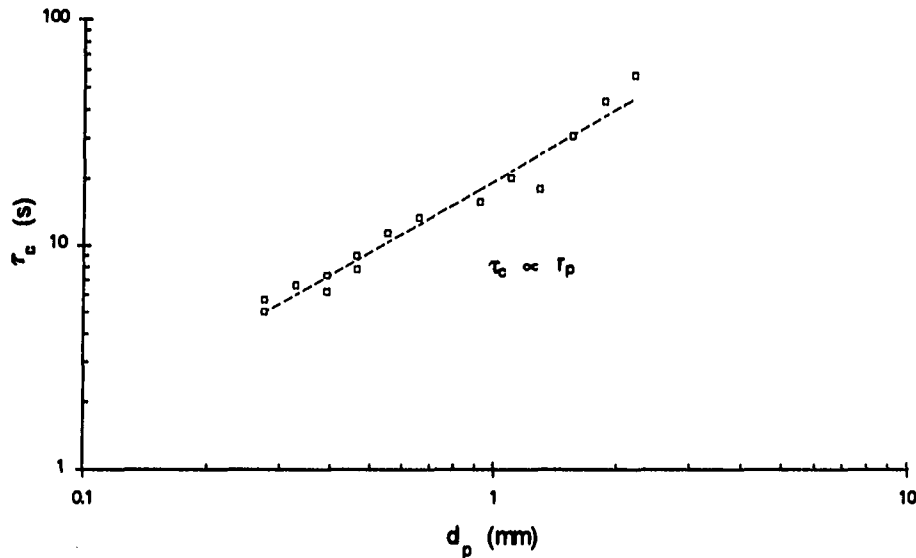


Figure 8.5: Calcination time constants versus limestone particle size

#### 8.4.2 Time constants for calcination and sulfation

##### a. Calcination

Recall the time constant in Eq. 8.3 for chemistry limited calcination

$$\tau_c = \frac{\rho_L d_p}{4k_c M_L} \quad (8.7)$$

Equation 8.3 suggests that the calcination time constant is expected to be linear with particle diameter. Time constants for calcination are plotted versus particle size on log-log scales in Fig. 8.5. The slope of the line is unity, indicating that the time constant is, indeed, proportional to the particle size. This result suggests that chemistry is rate limiting and is in agreement with the conclusion derived from the activation energy computed in section 8.3.

##### b. Sulfation

Interpretation of sulfation time constants is not as straight forward. Borgwardt and Harvey [29] observed that the dependence of sulfation rates on particle size is a function of

the average pore size of the sorbent particle. For limestone with pore sizes between 0.2 and 0.7  $\mu\text{m}$ , the sulfation rate is inversely proportional to diameter [29]. This result is deduced from the fact that, due to slow pore diffusion, the reduced penetration of the reactant gas into the sorbent confines the reaction to the outside periphery of the particles and only the superficial area participates in the reaction. The reaction rate is proportional to this superficial area, which, in turn, is proportional to  $1/d_p$  (equivalent to  $1/r_p$ ) [29]. Sulfation rates for particles with relatively large pores (1.5  $\mu\text{m}$ ) are independent of particle size. Obviously, large pores do not restrict the diffusion of  $\text{SO}_2$  to the reaction site and, since the reaction rate constant  $k_s$  is independent of particle size, the reaction rate is not a function of particle size.

When very small limestone particles are involved (of the order of 15  $\mu\text{m}$  dia. and smaller), pore diffusion is completely eliminated due to small pore size, and sulfation takes place at the exterior of the particle. In this case,  $\text{CaSO}_4$  deposits on the outer surface of the particle [29]. Diffusion of  $\text{SO}_2$  through this external product layer results in the reaction rate being proportional to  $1/r_p^2$  [29]. The work described in this book deals with limestone particles of 0.2 to 2 mm dia., which are assumed to consist of CaO micrograins. Since product layer diffusion occurs at the grain level, the sulfation reaction rate is independent of particle size and is expected to be proportional to  $1/r_g^2$ , where  $r_g$  is the radius of the CaO grain. Table 8.4 summarizes the rate limiting regimes in limestone sulfation as described by Borgwardt and Harvey [29].

For chemistry rate limiting, the time constant for sulfation is defined by Eq. 8.4 as

$$\tau_s = r_g \frac{\rho_g}{2\eta_s k_s M_A [\text{SO}_2]_i}, \quad (8.4)$$

which is independent of particle size but proportional to grain radius (a logical result since the reaction occurs at the grain level). Product layer diffusion limited sulfation changes the time constant to

$$\tau_s = r_g^2 \frac{P_g}{2\eta_s D_p M_A [SO_2]_i} \quad (8.5)$$

This result is in agreement with Borgwardt and Harvey [29] who estimated that for product layer diffusion limited sulfation of 15  $\mu\text{m}$  particles and smaller, the reaction rate is proportional to the inverse square of particle size (in this work, sulfation takes place at the grain surface). Consequently, the time constant is expected to be independent of particle size.

Table 8.4: Particle dependence of sulfation reaction rate

Average pore size ( $\mu\text{m}$ )	Controlling	Reaction rate particle dependence	Time constant particle dependence
0.015	product layer diffusion	independent (depends on grain size $\propto 1/r_g^2$ )	independent (depends on grain size $\propto r_g^2$ )
0.2-0.7	pore diffusion	$1/r_p$	$r_p$
1.5	chemistry	independent (depends on grain size $\propto 1/r_g$ )	independent (depends on grain size $\propto r_g$ )

A plot of sulfation time constants vs. limestone particle size on log-log scale is shown in Fig. 8.6. The plot can be divided into two regions based on particle size. In this case, two power laws, between the sulfation time constant and particle size, may be deduced. For particles between 200  $\mu\text{m}$  and 660  $\mu\text{m}$ , the sulfation time constant varies as

$$\tau_s \propto r_p^{0.2}, \quad (8.5)$$

which has a very weak correlation coefficient (0.42), a relatively weak correlation significance (significance is the P-value of t-statistic is 0.052 for a confidence level of 0.05), and a standard error of the power coefficient of 41% (i.e. the power coefficient is  $0.2 \pm 0.08$ ). A strong correlation is supported by near unity correlation coefficients, P-values that are substantially

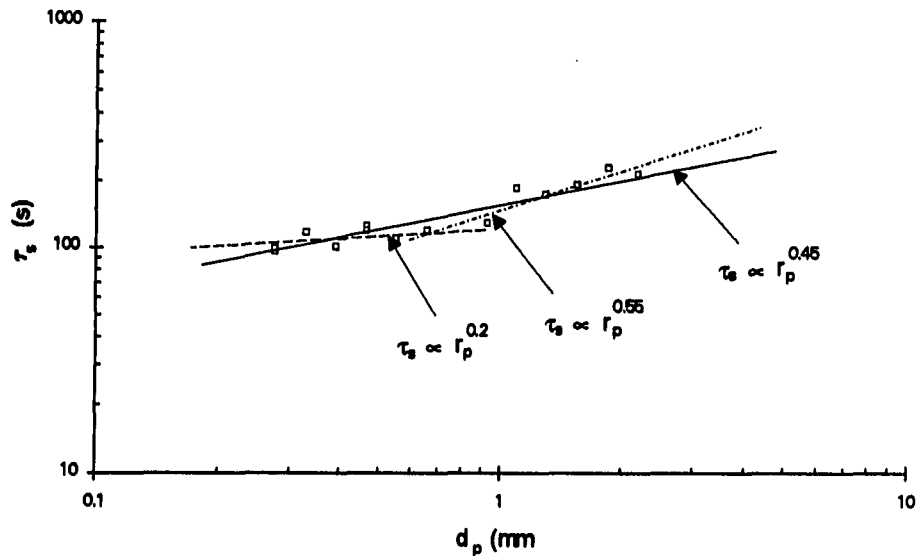


Figure 8.6: Sulfation time constants versus limestone particle size

smaller than the confidence level of the regression, and very small standard errors of the regression coefficients. This observation suggests that the power dependence of  $\tau_s \propto r_p^{0.2}$  may not be feasible in this range of particle sizes, or that more data is required to validate the relationship in Eq. 8.5 (only 6 data points were statistically tested in this size range).

As particle size increases beyond 660  $\mu\text{m}$ , the relationship between sulfation time constant and diameter becomes

$$\tau_s \propto r_p^{0.55}, \quad (8.6)$$

suggesting a stronger dependence on particle size. This is evidence that pore diffusion is becoming rate limiting as particle size increases. Again, sulfation may start out as a chemically controlled process. Soon pores, which are now numerous and longer compared to those for small particles, fill with product deposits and pore diffusion becomes rate limiting. The

power law deduced in Eq. 8.6 has a correlation coefficient of 0.75 and a P-value of 0.01. The standard error of the regression coefficient was 27% ( $0.55 \pm 0.14$ ).

A more powerful correlation may be estimated if the entire range of particle sizes (0.2-2 mm) is considered in the analysis. The power law in this case is

$$\tau_s \propto r_p^{0.45} \quad (8.7)$$

and has a correlation coefficient of 0.89, a P-value of  $4.9 \times 10^{-8}$ , and a standard error of the power coefficient no larger than 7% ( $0.45 \pm 0.031$ ). The strong correlation data indicate that this relationship is more feasible. A power law of 0.45 may suggest that sulfation is initially governed by chemistry or product layer diffusion, but soon, pore diffusion becomes rate limiting.

Complete chemistry control is possible if pores are of large size (1.6  $\mu\text{m}$ ) [29]. For particles larger than 125  $\mu\text{m}$  dia. and with pores around 0.42  $\mu\text{m}$  in size, the reaction is totally governed by pore diffusion [29]. It is hypothesized that the limestone used in this work has intermediate size pores (between 0.42 and 1.6  $\mu\text{m}$ ), thus both chemistry and pore diffusion determine the reaction rate. The fact that, as particle size is reduced below 0.66 mm, the time constant seems to become more weakly dependent on particle size, implies that chemistry may become more dominant for the smaller particle sizes. This result is based on the premise that time constants for sulfation of small and large particle limestones are estimated at different stages of the process.

Time constants for sulfation are always estimated after calcination is complete. Calcination occurs very fast for small particles and sulfation time constants for short times are calculated very early in the sulfation process. As seen in Fig. 8.7, which shows dimensionless plots of  $\text{CO}_2$  and  $\text{SO}_2$  for 390  $\mu\text{m}$  limestone particles, no significant sulfation occurs before calcination is complete. Thus, the time constant is taken at fairly early times where the process is still governed by the rate of the surface reaction. Unlike small particles, significant sulfation has occurred prior to cessation of calcination for 1.55 mm particles (as seen in Fig. 8.8).

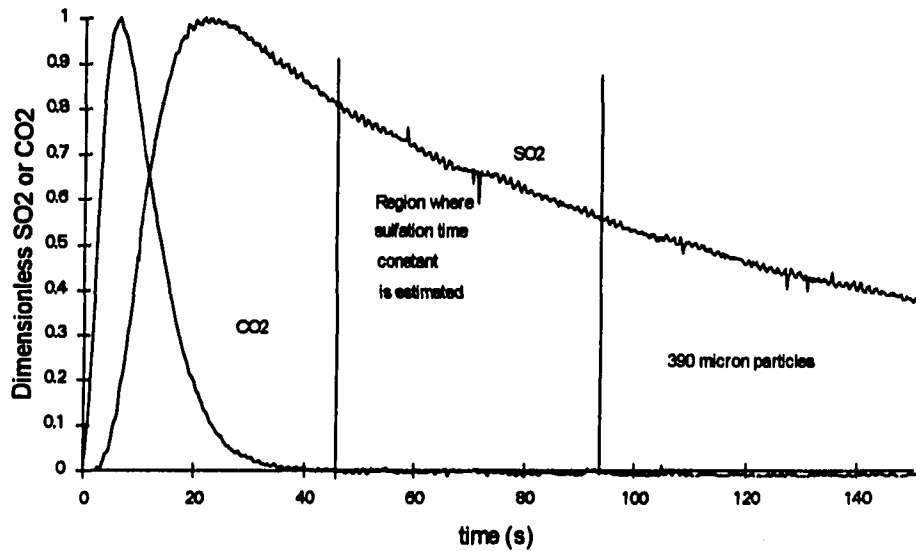


Figure 8.7: Dimensionless  $\text{CO}_2$  and  $\text{SO}_2$  profiles for 390 micron particles

The time constant is now taken at a region farther away from the initial sulfation region. At later times, pore diffusion is more dominant than either chemistry.

A broader picture of sulfation can be drawn from the idea that as the reaction proceeds, different processes become rate limiting. At early times, sulfation is limited by the intrinsic kinetics of the surface reaction (chemistry). Product layer diffusion becomes rate limiting at intermediate times and for short intervals as the deposition of  $\text{CaSO}_4$  around the grains offers an additional resistance to  $\text{SO}_2$ . Finally, as the product fills the pores, pore diffusion becomes rate limiting. Consequently, the stage of sulfation at which the time constant is computed determines the dependence of the latter on particle size.

Overall, the low activation energies and weak power law dependence of sulfation time constants on particle size are indicative of chemistry controlling the process at early times and pore diffusion at the later stages of the process.

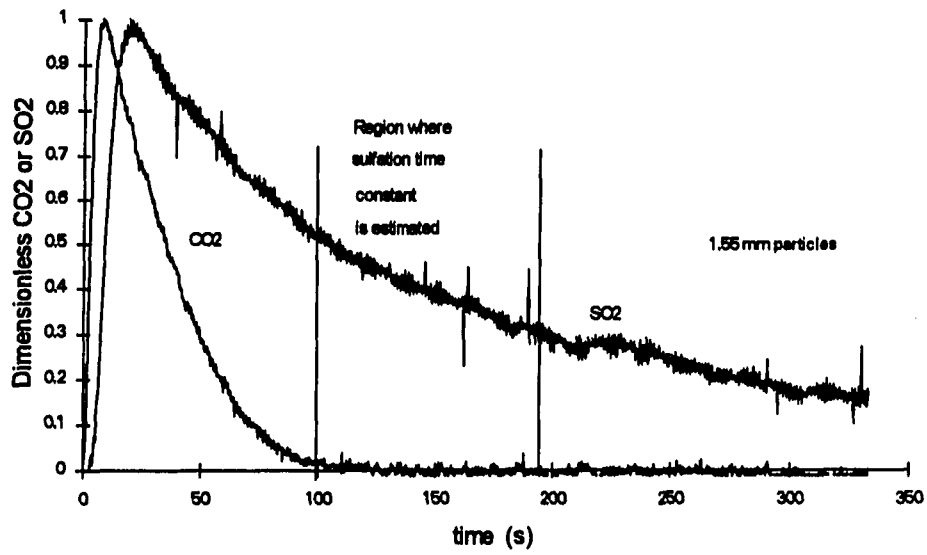


Figure 8.8: Dimensionless CO<sub>2</sub> and SO<sub>2</sub> profiles for 1.55 mm particles

## 9. CONCLUSION

A new methodology that utilizes transient operation of coal fired boilers to investigate kinetics of coal combustion and limestone calcination and sulfation is introduced. The technique employs perturbations in  $\text{CO}_2$  and  $\text{SO}_2$  profiles to obtain characteristic times for coal devolatilization, char burning, limestone calcination, and limestone sulfation. This new method is suitable for use in large scale boilers since it employs standard boiler instrumentation. Furthermore, the technique is not intrusive to the boiler's operation and requires little or no sample preparation.

Validation tests were carried out using monosized samples of coal and limestone batched in a small fluidized bed combustor heated with propane or natural gas. To simulate sulfur release from coal, sulfur dioxide was injected to the bed during the limestone tests.

### 9.1 Coal combustion

Devolatilization times estimated using this method are comparable to those obtained by other researchers [1,2,11] and vary proportionally with the square of initial coal particle size for particles larger than 3 mm. Volatiles release times for coal particles smaller than 3 mm were fouled by the lag of the sampling system, which had a characteristic lag time of 3 s.

Variation of characteristic char burning times with particle size was also investigated. Characteristic char burning times were found to be proportional to  $d^{1.3}$ , which is contrary to the classical  $d$ -squared law reported by other researchers [1,3,11,15] for mass transfer limited char combustion. Ratios of char burnout times to characteristic char burning times were estimated to be around 0.6, suggesting that the combustion of char is controlled by mass transfer of oxygen to the particle. Additional evidence that support this observation are the near-zero activation energies obtained for the combustion of char.

The lower than expected power law relationship between characteristic char burning times and initial particle size was attributed to primary fragmentation of coal. Primary

fragmentation reduces the initial char size, thus reducing the time required for the combustion of the char particles. To investigate this hypothesis, char samples were obtained by quenching the bed with nitrogen immediately after devolatilization of monosized coal batches was completed. The average size of char obtained from these tests was between 70 to 80 % of the initial particle size, indicating that primary fragmentation reduces the initial char particle size significantly. This result is in agreement with Chirone et al. [13] who also confirmed that primary fragmentation of coal decreases the char particle size.

## 9.2 Limestone calcination

The extent of limestone calcination did not vary considerably with particle mass, bed temperature, or particle size. Characteristic limestone calcination times were found to be independent of particle mass. Activation energies of  $45 \pm 5$  kcal/mol for calcination were estimated by plotting inverse characteristic times for calcination vs. inverse bed temperature. This result is in good agreement with activation energies of calcination obtained by Borgwardt [32] and Powell and Searcy [33]. Large activation energies suggest that limestone calcination is exclusively controlled by chemical kinetics. This result is confirmed by the fact that the time constants for calcination were proportional to limestone particle size, which is expected for limestone calcination according to the relationship

$$\tau_c = \frac{\rho_L d_p}{2 k_c M_L} \quad (9.1)$$

## 9.3 Sulfation kinetics

In general, the extents of sulfation obtained in this work are significantly lower than what other researchers have reported [20, 23-26]. It is believed that the limestone is not utilized very well primarily because of severe pore plugging. Over longer time periods attrition of the particles in the bed may open up fresh sites on the sulfated particles, which will consume additional  $\text{SO}_2$ . However, the attrition process is very slow and the weak  $\text{SO}_2$  signal produced (much like the weak  $\text{CO}_2$  signal produced by large, slow burning char particles) is

lost in the background noise. It is, therefore, believed that the actual extent of sulfation is much higher than what measured by these experiments.

The extent of sulfation was not significantly affected by limestone sample mass, but it increased considerably when the inlet  $\text{SO}_2$  concentration was increased from 200 ppm to 1000 ppm. This result was attributed to both higher sulfation rates and increased interphase mass transfer between bubble and emulsion at the higher  $\text{SO}_2$  conditions.

The extent of sulfation increases as temperature changes from 720 to 800 °C, decreases for temperatures between 800 and 870 °C, and increases again thereafter. The increase of the extent of sulfation between 720 and 800 °C was attributed to larger pore area generated by increased calcination rates. Between 800 and 870 °C the extent of sulfation decreases. Due to increased sulfation rates,  $\text{SO}_2$  reacts with CaO before it has diffused in the particle, thus plugging the pores and making internal particle area unavailable to further sulfation. As temperature exceeds 870 °C, dissociation of  $\text{CaSO}_4$ , which plugs the pores, makes the internal particle area available to  $\text{SO}_2$ . Consequently, the extent of sulfation increases as temperature exceeds 870 °C.

Characteristic sulfation times doubled when inlet  $\text{SO}_2$  changed from 1000 ppm to 200 ppm obviously because of slow-down in interphase mass transfer between bubble and emulsion at the lower inlet conditions. In addition, the characteristic sulfation time is independent of sample mass when inlet  $\text{SO}_2$  is at 1000 ppm. This was not the case for 200 ppm  $\text{SO}_2$ , where limestone depleted the  $\text{SO}_2$  in the emulsion phase, and the contribution of interphase mass transfer, between bubble and emulsion, to the characteristic sulfation time became important. Consequently, the characteristic sulfation time varied considerably with sample mass at 200 ppm inlet  $\text{SO}_2$ .

Activation energies of  $14 \pm 2$  kcal/mol were obtained for sulfation. There is good agreement between this activation energy and values reported by Bhatia and Perlmutter [36] for chemistry limited sulfation. The lower than expected activation energies were in

disagreement with some researchers [4,22,31,34], who obtained activation energies in the range of 30-53 kcal/mol for product layer diffusion limited sulfation. Particle size affects the controlling regime for sulfation. Product layer diffusion becomes rate limiting during sulfation of small particles 1-15  $\mu\text{m}$  as the product builds outside the particle and obstructs the direct reaction of  $\text{SO}_2$  with  $\text{CaO}$ . Sulfation of large particles used in this work (0.28-2 mm) is limited by chemistry in the beginning but quickly becomes limited by pore diffusion and pore plugging, a result that is in good agreement with results obtained by Simmons and Garman [35].

Since both chemistry and pore diffusion limited sulfation yield similar activation energies, the distinction as to which process is rate limiting can be made by investigating the particle size dependence of the characteristic time for sulfation.

For chemistry or product layer diffusion limited sulfation, the characteristic time is expected to be independent of particle size [32]. Pore diffusion limited sulfation is expected to have time constants that are proportional to  $r_p$ . The sulfation time constant for particles between 0.2 and 0.66 mm was found to be proportional to  $r_p^{0.2}$ . The weak particle dependence of characteristic sulfation time on particle size and the low activation energy are indicative of chemical kinetics being rate limiting early in the sulfation process. Particles between 0.66 to 2 mm yielded time constants that were proportional to  $r_p^{0.55}$ , suggesting that pore diffusion becomes important at the later stages of sulfation. A power law of  $r_p^{0.45}$ , which also suggests pore diffusion becomes rate limiting, is deduced for the entire particle range (0.2-2 mm) under consideration.

Based on the variable particle size results, it is expected that characteristic sulfation times become independent of particle size for particles smaller than 0.2 mm and proportional to limestone particle size for particles larger than 2 mm.

The method which was used to obtain the time constants may have also contributed to this particle size dependence. Time constants for sulfation are estimated from the  $\text{SO}_2$  profiles at the time when calcination is completed. Particles smaller than 0.66 mm calcine fast and

little or no sulfation takes place prior to the completion of calcination. Thus, the time constant is measured at a point early in the sulfation process where chemistry is rate limiting. Significant sulfation has occurred prior to the completion of calcination of particles larger than 0.66 mm. Consequently, the time constant is measured at an intermediate time in the sulfation process where build up of  $\text{CaSO}_4$  begins to plug the pores and pore diffusion is becoming rate limiting.

Furthermore, the simplifications on the sulfation model were made with particular emphasis on short time behavior of the  $\text{SO}_2$  profiles which prevents successful prediction of the sorbent's behavior at later times when pore diffusion is the rate limiting mechanism.

#### **9.4 Suggestions for future tests**

Based on the results obtained in this work, several suggestions can be made for future tests involving calcination and sulfation of limestone.

Calcination tests should be repeated without  $\text{SO}_2$  in the bed to investigate if, indeed, sulfation affects the initial rate of calcination. Furthermore, step tests may improve the utilization of limestone as compared to what was observed for limestone batches since sorbent attrition affected the utilization in the former tests. Also, the use of calcined limestone may help investigate whether early time behavior of  $\text{SO}_2$  is affected by calcination. Finally, the effect of bed velocity on calcination and sulfation should be investigated.

**BIBLIOGRAPHY**

1. Essenhigh, R. H. *Journal of Engineering for Power*: 183-190, July 1963.
2. Ragland, K. W. and Weiss, G. A. *Energy* 4: 141-148 (1979).
3. Avedesian, M. M. and Davidson, J. F. *Trans. Instn. Chem. Engrs* 51: 121-131 (1973).
4. Mulligan, T., Pomeroy, M., and Bannard, J. E. *Journal of the Inst. of Energy* 62: 40-47 (1989).
5. Saxena, S. C. *Prog. Energy Combust. Sci.* 16: 55-94 (1990).
6. Essenhigh, R. H. *Chemistry of coal utilization*, Second Supplementary Vol., Martin A. Elliot (ed.), Wiley & Sons, New York 1981: 1153-1312.
7. Given, P. *Fuel* 39: 147 (1960).
8. Howard, J. B. *Chemistry of coal utilization*, Second Supplementary Vol., Martin A. Elliot (ed.), Wiley & Sons, New York 1981: 665-784.
9. Daw, C. S., Stallings, J. W., Rowley, D. R., Perna, M. A., and Divilio, R. J. *Proc. of the 11th ASME International Conference on Fluidized Bed Combustion*, Montreal, Canada: 1145-1150 (1991).
10. Anthony, D. B., Howard, J. B., Hottel, H. C., and Meissner, H. P. *15th Symp. (Int.) Combustion*, The Combustion Institute, Pittsburgh 1975: 1303-1317.
11. Pillai, K. K. *J. Inst. Energy* 58: 3-7 (1985).
12. Stubington, J. F. and Sumayono *Fuel*: 63, 1013-1019 (1984).
13. Chirone, R., Massimilla, L., and Salatino, P., *Prog. Energy Combust. Sci.* 17: 297-326 (1991).
14. Chirone, R. and Massimilla, L. *22nd Intl. Symp. on Comb.* (The Combustion Institute): 267-277 (1988).
15. Ross, I. B., and Davidson, J. F. *Trans. Instn. Chem. Engrs.* 59: 108-114 (1981).
16. Basu, P. *Fuel* 56: 390-392 (1977).

17. Ragland, K. W. and Pecson, F. A. *22nd Intl. Symp. on Comb.* (The Combustion Institute) Pittsburg, PA, 1988.
18. *Reviews in coal science*, IEA Coal Research, Butterworths, London, 1989.
19. Moffat, A. J. *Proceedings of the Central States Section of the Combustion Institute* (1982).
20. Christofides, N. J. and Brown, R. C. *Proceedings of the 11th Intl. Conf. on Fluid. Bed. Comb.* Montreal, Quebec, Canada (1991).
21. Simmons, G. A., Garman, A. R., and Boni, A. A. *AIChE Journal* 33: 211-217 (1987).
22. Borgwardt, R. H., Bruce, K. R., and James, B. *Ind. Eng. Chem. Res.* 26 (#10): 1993-1998 (1987).
23. Hadji-Sulaiman, M. Z. and Scaroni, A. W. *Fuel Proc. Technol.* 31: 193-208 (1992).
24. Jonke, A. A., Vogel, G. J., Carls, E. L., Ramaswami, D., Anastasia, L., Jarry, R., and Haas, M. *Air Pollution and Its Control, AIChE Symposium Series*, R. W. Coughlin, A. F. Sarofim, and N. J. Weinstein. 68 (#126): 241-251 (1972).
25. Brown, R. C. *Fossil Fuels Utilization (Environmental Concerns)*, R. Markuszewski and B. Blaustein (Ed.), American Chemical Society, Washington, DC 1986: 98-108.
26. Fogler, H. S. *Elements of Chemical Reaction Engineering*, Neal R. Admundson (Ed.), Prentice-Hall, New Jersey 1986: 560-595.
27. Doraiswamy, L., *Heterogeneous reactions: analysis, examples, and reactor design*, Wiley, New York 1984.
28. Szekely, J., Evans, J. W., and Sohn, H. Y., *Gas solid reactions*, Academic Press, New York 1976: 101-103.
29. Borgwardt, R. H. and Harvey, R. D., *Environmental Science and Technology* 6: 350-360 (1972).
30. Sundback, C. A., Beer, J. M., and Sarofim, A. F., *20th Symp (Int.) on Combustion*, (The Combustion Institute) 1984: 1495-1503.
31. Borgwardt, R. H., *AIChE Journal* 31: 103-111 (1985).
32. Powell, E. K., and Searcy, A. W., *Metallurgical Transactions* 11B: 427 (1980).

33. Simmons, G. A. and Garman, A. R., *AIChE Journal* 32 (#9): 1491-1499 (1986).
34. Bhatia, S. K. and Perlmutter, D. D., *AIChE Journal* 27 (#2): 226-234 (1981).
35. Simmons, G. A., Parker, T. E., and Morency, J. R., *Combustion and Flame* 74: 107-110 (1988).
36. La Nauze, R. D., *Fluidization* (2nd Ed.), Academic Press, London 1985, pp. 648-674.
37. *Perry's Chemical Engineer's Handbook* (6th ed.) Robert H. Perry (ed.), McGraw Hill, New York 1984, pp. 3-247 to 3-291.

## APPENDIX A. INTRAPARTICLE DIFFUSION KINETICS

### A.1 Model development

The intraparticle diffusion model is developed based on simple mass balances on the diffusing species in and/or out of the particle. A simple representation of the model is shown in Fig. A.1 [27]. The model is developed based on L. Doraiswamy's [27] heterogeneous reaction book and on catalysis theory in Fogler [26].

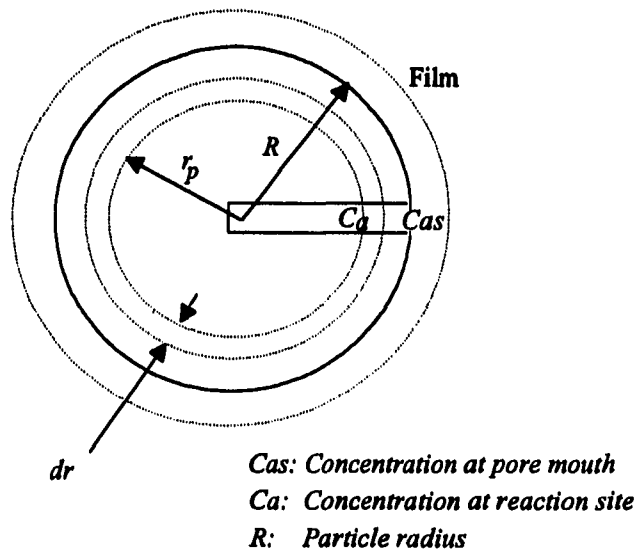


Figure A.1: Schematic representation of intraparticle diffusion model

The assumptions that apply here are:

- Isothermal particle
- Single reactant involved (denoted as A)
- Fick's law applies:  $\text{Mole Flux} = D_e \frac{dC_a}{dr_p}$
- No volume change occurs
- Quasi-steady conditions exist in the particle (applied in this work)

Based on the assumptions stated above, the mass balance on the concentration of A through a spherical element inside the particle is

$$\text{Mole in} - \text{Mole out} = \text{Mole produced/consumed by reaction.} \quad (\text{A.1})$$

According to Fick's law, the moles of A going through the spherical element of thickness  $dr$  is

$$\text{Moles in} = 4\pi r_p^2 D_e \frac{dC_a}{dr_p}, \quad (\text{A.2})$$

where  $r_p$  is the radius at which this element is taken,  $D_e$  is the effective diffusivity through the particle, and  $C_a$  is the concentration of A inside the particle. The moles of A going out of the particle pores are

$$\text{Moles out} = 4\pi(r_p + dr_p)^2 D_e \left[ \frac{dC_a}{dr_p} + \frac{d}{dr_p} \left( \frac{dC_a}{dr_p} \right) dr_p \right]. \quad (\text{A.3})$$

The moles of A produced by reaction are

$$\text{Moles produced} = -4\pi r_p^2 dr_p \cdot (\text{Reaction rate}). \quad (\text{A.4})$$

Equation A.3 can be expanded and simplified by neglecting terms of higher order, i.e.  $dr_p^2$  and  $dr_p^3$  to yield

$$\text{Moles out} = 4\pi D_e \left( r_p^2 \frac{dC_a}{dr_p} + 2r_p dr_p \frac{dC_a}{dr_p} + r_p^2 dr_p \frac{d^2 C_a}{dr_p^2} \right). \quad (\text{A.5})$$

Substituting Eqs. A.2, A.4, and A.5 into Eq. A.1 and simplifying yields

$$D_e r_p^2 \frac{d^2 C_a}{dr_p^2} + D_e 2r_p \frac{dC_a}{dr_p} = -r_p^2 \cdot (\text{Reaction rate}) \quad (\text{A.6})$$

Assuming a first order reaction

$$\text{Reaction rate} = k_v C_a, \quad (\text{A.7})$$

where  $k_v$  is the intrinsic reaction rate constant Eq. A.6 becomes

$$D_e r_p^2 \frac{d^2 C_a}{dr_p^2} + D_e 2r_p \frac{dC_a}{dr_p} = r_p^2 k_v C_a. \quad (\text{A.8})$$

Dividing Eq. A.8 by  $D_e$  and  $r_p$

$$\frac{d^2 C_a}{dr_p^2} + \frac{2}{r_p} \frac{dC_a}{dr_p} = \frac{k_v}{D_e} C_a. \quad (\text{A.9})$$

Equation A.9 can be non-dimensionalized by claiming the following non dimensional variables

- Dimensionless concentration  $\hat{C}_a = \frac{C_a}{C_{as}}$
- Dimensionless radius  $\hat{R} = \frac{r_p}{R}$

$$\frac{C_{as}}{R^2} \frac{d^2 \hat{C}_a}{d\hat{R}^2} + \frac{2}{R\hat{R}} \frac{C_a}{R} \frac{d\hat{C}_a}{d\hat{R}} = \frac{k_v C_{as}}{D_e} \hat{C}_a \quad (\text{A.10})$$

Multiplying Eq. A.10 by  $R^2$  and dividing by  $C_a$  gives

$$\frac{d^2 \hat{C}_a}{d\hat{R}^2} + \frac{2}{\hat{R}} \frac{d\hat{C}_a}{d\hat{R}} = R^2 \frac{k_v}{D_e} \hat{C}_a \quad (\text{A.11})$$

The Thiele modulus,  $\phi_{s1}$ , for spherical particles and first order reaction kinetics is defined as

$$\phi_{s1} = R \sqrt{\frac{k_v}{D_e}} \quad (\text{A.12})$$

Substituting Eq. A.12 into Eq. A.11

$$\frac{d^2 \hat{C}_a}{d\hat{R}^2} + \frac{2}{\hat{R}} \frac{d\hat{C}_a}{d\hat{R}} = \phi_{s1}^2 \hat{C}_a. \quad (\text{A.13})$$

Equation A.13 can be solved analytically for the dimensionless concentration of A at the spherical element under consideration. The boundary conditions are

- $\hat{C}_a = 1$  at  $\hat{R} = 1$  and
- $\frac{d\hat{C}_a}{d\hat{R}} = 0$  at  $\hat{R} = 0$

A solution to Eq. A.13 can be found by assuming a functional form for  $\hat{C}_a$ , otherwise the problem is not trivial. Assuming that

$$\hat{C}_a = \frac{1}{\hat{R}} [C_1 \sinh(\phi_{s1}x) + C_2 \cosh(\phi_{s1}x)] \quad (\text{A.14})$$

and applying the boundary conditions, the solution to A.13 is

$$\hat{C}_a = \frac{\sinh(\phi_{s1}\hat{R})}{\hat{R} \sinh \phi_{s1}}. \quad (\text{A.14})$$

By definition, the internal effectiveness factor  $\eta$  is

$$\eta = \frac{\text{Actual reaction rate}}{\text{Reaction rate if particle is at surface conditions}} \quad (\text{A.15})$$

If pore diffusion is the rate limiting step, then the actual reaction rate will be equal to the rate of species diffusion through the pores. According to Fick's law

$$\text{Actual reaction rate} = 4\pi R^2 D_e \left[ \frac{d\hat{C}_a}{d\hat{R}} \right]_{\hat{R}=1} \frac{C_{as}}{R} \quad (\text{A.16})$$

The reaction rate if the internal surface of the particle is exposed to the surface concentration of  $C_a$  is

$$\left( \begin{array}{c} \text{Reaction rate at} \\ \text{surface conditions} \end{array} \right) = \frac{4}{3} \pi R^3 k_v C_{as} \quad (\text{A.17})$$

Substituting  $d\hat{C}_a/d\hat{R}$  into Eq. A.16 and simplifying yields

$$\text{Actual reaction rate} = 4\pi R C_{as} D_e (\phi_{s1} \coth \phi_{s1} - 1) \quad (\text{A.18})$$

Dividing Eq. A.18 by Eq. A.17 to obtain the effectiveness factor

$$\eta = \frac{4\pi R C_{as} D_e (\phi_{s1} \coth \phi_{s1} - 1)}{\frac{4}{3} \pi R^3 k_v C_{as}} = \frac{3}{R^2 \frac{k_v}{D_e}} (\phi_{s1} \coth \phi_{s1} - 1) \quad (\text{A.19})$$

Substituting the Thiele modulus from Eq. A.12 into Eq. A.19 yields the first order effectiveness factor for spherical particles

$$\eta = \frac{3}{\phi_{s1}^2} (\phi_{s1} \coth \phi_{s1} - 1) \quad (\text{A.20})$$

### A.2 Estimating the effective diffusion coefficient $D_e$

The effective diffusion coefficient,  $D_e$ , is defined as a combination of the pore diffusion coefficient,  $D_p$ , and the Knudsen diffusivity,  $D_K$  (27)

$$\frac{1}{D_e} = \frac{1}{D_p} + \frac{1}{D_K}. \quad (\text{A.21})$$

The pore diffusivity may be estimated from the diffusion coefficient in the bulk of the flow (27)

$$D_p = D_a \frac{\epsilon_p}{\zeta} \quad (\text{A.22})$$

where  $\epsilon_p$  is the particle void and  $\zeta$  is the tortuosity factor, which is a measure of the complexity of the pore structure.

Knudsen diffusion occurs in the pores when the mean free path of the diffusing species is larger than the pore diameter. The molecules of the diffusing species bounce off the pore walls as they diffuse inside the particle, thus slowing down their motion. The Knudsen diffusion coefficient is given by the formula

$$D_e = \frac{19400}{\zeta} \frac{\epsilon_p^2}{S_g \rho_p} \left( \frac{T}{M} \right)^{\frac{1}{2}}, \quad (\text{A.23})$$

where  $\rho_p$  is the particle density,  $S_g$  is the A.E.T. pore area, and  $M$  is the molecular weight of the diffusing species.

## APPENDIX B. PARAMETERS USED IN CALCINATION/SULFATION MODEL

### B.1 Mass transfer coefficients for CO<sub>2</sub> and SO<sub>2</sub>

Mass transfer coefficients for CO<sub>2</sub> and SO<sub>2</sub> are estimated using the particle Sherwood number for fluidized beds given by La Nauze [36]

$$Sh = 2\epsilon_b + 0.69 Re^{1/2} Sc^{1/3}, \quad (\text{B.1})$$

where the particle Reynolds number,  $Re$ , and the Schmidt number,  $Sc$ , are specific to each gas since they depend on gas properties. The mass transfer coefficient is estimated from the Sherwood number as

$$h = \frac{Sh D_{AB}}{d_L}, \quad (\text{B.2})$$

where  $D_{AB}$  is the binary diffusion coefficient of species A (either CO<sub>2</sub> or SO<sub>2</sub>) in air (species B). Gas properties for SO<sub>2</sub> and CO<sub>2</sub> are tabulated in Perry's Chemical Engineer's Handbook [37]. Binary diffusion coefficients are estimated from empirical relationships found in the same reference [37].

### B.2 Reaction rates for calcination and sulfation

The reaction rate constants used in the simulation were approximated from the simplified model results since these could be made a priori to the simulation using the test results. The time constant for calcination is defined as

$$\tau_c = \frac{\rho L r_p}{k_c M_L}. \quad (\text{B.3})$$

The rate constant for calcination,  $k_c$ , is estimated from the data using appropriate time constants and particle sizes. The average reaction rate constant estimated from all tests was 0.2 m/s.

Sulfation rate constants were taken from Mulligan et al. [4] to be 0.02 m/s.

The time constant for pore plugging,  $\tau_p$ , is related to the sulfation time constant as

$$\tau_p = \frac{\tau_s}{2}. \quad (\text{B.4})$$

Thus, this parameter was estimated from the experimental characteristic time for sulfation for 1 mm limestone particles, which was approximately 128 s (test 18X20a1).

### B.3 Initial conditions

Initial conditions involve 1000 ppm of  $\text{SO}_2$  at the reactor inlet and 20 g of limestone batched in the bed. Table B.2 lists all initial conditions used.

Table B.2: Initial conditions for simulation

Parameter	Initial condition
$[\text{CO}_2]_R$	8 %
$[\text{CO}_2]_s$	8 %
$[\text{CO}_2]_c$	8 %
$[\text{SO}_2]_R$	1000 ppm
$[\text{SO}_2]_s$	1000 ppm
$[\text{SO}_2]_c$	1000 ppm
$m_L$	20 g
$r_{ge}$	$4.8 \times 10^{-8}$ m
$r_c$	0.001 m

## **APPENDIX C. CALIBRATION OF INSTRUMENTS AND MEASUREMENT ACCURACY**

### **C.1 Calibration of instruments**

The following sections give a brief account on how the instrumentation used in this work was calibrated including standards used for calibration plus calibration equipment. Note that calibration standards, like calibration gases and reference equipment, were chosen based on the requirements of this work. Variation in calibration standards is possible when the operating parameters are changed.

#### **C.1.1 Gas analyzer calibration**

Routine gas analyzer calibration was carried out every two to three days to compensate for drift. Drift values for each analyzer are given in Table C.1. Calibration gases were obtained from Air Products Inc. in Allentown, PA 18105. Pure nitrogen (99.9%) was used as zero gas. Table C.1 lists the concentrations of the calibration gases used in this work. Also given in Table C.1 are the error in the measurement for each unit and the repeatability as specified by the manufacturer.

Internal calibration of the instruments was performed when analyzers after extensive system maintenance. A Keithley model 197A high accuracy digital multimeter was used to measure reference potentials during the internal calibration. The detailed calibration was carried once every 6 months after maintenance of the instruments. Information for calibration of these instruments can be found in the operator's manual provided with the instruments.

#### **C.1.2 Calibration of flowmeters**

Orifice flowmeters were calibrated against a standard wet test flowmeter manufactured by the American Meter Co. in New York. Flowrates measured by the wet test meter were compared against the reading obtained from the differential transducer connected across the

Table C.1: Analyzer drifts and calibration gas concentrations

Gas analyzer	Scale	Drift (on a 24 hour basis)	Calibration gas	Error	Repeatability
Beckman 755 O <sub>2</sub> analyzer	25%	1% of full scale	7 % O <sub>2</sub> in nitrogen	1%	1% of full scale
Beckman 870 CO <sub>2</sub> analyzer	30%	1% of full scale	15% CO <sub>2</sub> in nitrogen	1%	1% of full scale
Beckman 870 CO analyzer	1.2%	1% of full scale	812 ppm CO in nitrogen	1%	1% of full scale
VIA-300 NO <sub>x</sub> analyzer	1000 ppm	1% of full scale	800 ppm NO <sub>x</sub> in nitrogen	1%	1% of full scale
VIA-500 SO <sub>2</sub> analyzer	2000 ppm	1% of full scale	1573 ppm SO <sub>2</sub> in nitrogen	1%	1% of full scale

orifice flowmeters. The accuracy of the flowrate measurement was approximately 5% of the full scale.

### C.1.3 Calibration of thermocouples

Thermocouple gain boards were calibrated on a 0-5V scale using a high accuracy D.C. power supply. Reference voltages were measured via the Metrabyte data acquisition program on the HP Vectra 386SX/16 computer used. Temperature readings were calibrated to an accuracy of  $\pm 2$  °C.

## APPENDIX D. PROGRAM CODE

```

*   A program to predict the species concentrations in a
*   fluidized bed for calcination and sulfation of
*   limestone. Per second basis.
*   Limestone batch.

*   Declare variables used as double precision
*       implicit double precision (a-h, o-z)
*   Declare primary integers
*       integer neq, iw
*   Specify working parameters (neq = number of equations)
*       parameter (neq=9,iw=(12+neq)*neq+50)
*   Declare secondary integers and arrays
*       integer ifail, istep
*       dimension y(neq),w(iw)
*   Declare external routines and common variables
*       external d02eaf, fcn
*       common CaO,fconv,dp
*       common pnum,rgrain
*   Variable definition
*   y(1) = SO2 concentration in bed (mol/m^3)
*   y(2) = SO2 concentration at particle surface (mol/m^3)
*   y(3) = SO2 concentration at reaction site (mol/m^3)
*   y(4) = radius of grain core (m)
*   y(5) = CO2 concentration in bed (mol/m^3)
*   y(6) = CO2 concentration at particle surface (mol/m^3)
*   y(7) = CO2 concentration in particle core (mol/m^3)
*   y(8) = mass of limestone (g)
*   y(9) = radius of uncalcined limestone core (m)
*   -----
*   Initial values of variables
*       dp = 1000.0d-6
*       rgrain = 4.8d-8
*       y(1) = 0.0109d0
*       y(2) = 0.0109d0
*       y(3) = 0.0109d0
*       y(4) = rgrain*.99999d0
*       y(5) = 0.8734d0
*       y(6) = 0.8734d0

```

```

y(7) = 0.8734d0
y(8) = 20.0d0
y(9) = dp/2.0d0*0.99999d0
i = 0
time = 0.0d0

```

```

* Tolerance of integration
  tol = 1.d-25

```

```

* -----
* Creating output
  open (unit=10, name='csred3.out', status='old')
  open (unit=20, name='csred2.out', status='old')
  open (unit=30, name='solids.out', status='old')
* Send headings and initial values to output
  write (10,*) 'time'
  write (10,*) 'time','SO2R','SO2s','SO2','ri'
  write (20,*) 'time','CO2R','CO2s','CO2','rc'
  write (10,99998)time,y(1),y(2),y(3),y(4)
  write (20,99998)time,y(5),y(6),y(7),y(8)
  write (30,99999)time,y(9)

```

```

* -----
* Beginning iteration
* The routine d02eaf is found in the NAG library that is
* resident on the Vincent work stations. For further help
* on how to use the subroutine 'add nag' on Vincent and then
* type 'naghelp'. Further documentation may be found in
* room 191 Durham.

```

```

  ifail = 0
  do istep = 1,5500

```

```

* Subdividing step for initial integration time
  if (istep.le.4500) then
    tend = dfloat(istep)/50.0d0
  else
    tend = 90.0d0 + dfloat(istep-4500)/2.0d0
  endif

```

```

* Calling the integration subroutine
  call d02eaf(time,tend,neq,y,tol,fcn,w,iw,ifail)

```

```

    i = i + 1
    if (i.eq.20) then
*   print *, time, y(8)
        i = 0
*   Send data to output
        write (10,99998)time,y(1),y(2),y(3),y(4)
        write (20,99998)time,y(5),y(6),y(7),y(8)
        write (30,99999)time,y(9)
    endif

    end do
    close unit=10
*   close unit=20
99998 format (1x,e12.5,',',e12.5,',',e12.5,',',e12.5,',',e12.5)
99999 format (1x,e12.5,',',e12.5)
    stop
    end

* -----
* Subroutine fcn is called by d02eaf interally. This routine contains
* the system of differential equations to be integrated
    subroutine fcn(time,y,f)
    implicit double precision (a-h, o-z)
    integer neq
    parameter (neq=9)
    dimension y(neq), f(neq)
*   Declare common variables
    common CaO,fconv,dp
    common pnum,rgrain
* -----
* Pi
    pi = 3.14d0
*   Bed paramters
*   Superficial bed velocity (m/s)
    u = 1.0d0
*   Minimum fluidization velocity (m/s)
    umf = 0.15d0
*   Bed depth (m)
    bl = 0.1524d0
*   Intrinsic bed parameter (1/s)
    cbed = u/bl
*   Bed diameter (m)
    dbed = 0.2032d0

```

- \* **Bed area**  
 $abed = \pi * d_{bed}^{**2} / 4.0d0$
- \* **Bed volume**  
 $v_{bed} = bl * abed$
- \* **Bed voids**
- \* **Bubble void**  
 $vb = 0.65d0$
- \* **Void at minimum fluidization**  
 $vmf = 0.8d0$
- \* **Limestoned mass (g)**  
 $sm = 20.0d0$
- \* **Bulk density of limestone in bed**  
 $rhobc = sm / v_{bed}$
- \* **Particle paramters**
- \* **Grain density (g/m<sup>3</sup>)**  
 $rhog = 2500.0d3$
- \* **Particle void**  
 $pvoid = 0.4$
- \* **Calcined particle density**  
 $rhop = rhog * (1.0d0 - pvoid)$
- \* **Limestone density**  
 $rho1 = 2500.0d3$
- \* **Particle volume (m<sup>3</sup>)**  
 $vpar = \pi * dp^{**3} / 6.0d0$
- \* **B.E.T. area of particle (m<sup>2</sup>/g)**  
 $sgs = 50.0d0$
- \* **Limestone fractional conversion**  
 $fconv = 1.0d0 - y(8) / sm$
- \*  $fconv = 1.0d0$
- \* **Production of calcium oxide from limestone**  
 $CaO = fconv * sm * 0.56d0$
- \* **Bulk density of CaO in bed**  
 $rho_{ba} = CaO / v_{bed}$
- \* **Film mass transfer coefficients (m/s)**
- \* **Carbon dioxide**  
 $hc = 0.544d0$
- \* **Sulfur dioxide**  
 $hs = 0.476d0$

```

*      Reaction rate constants
*      Calcination (m/s)
      rc = 0.2d0
*      Sulfation (m/s)
      rs = 1.1d-2

*      Gas inlet concentrations (mol/m^3)
*      Carbon dioxide
      CO2i = 0.8734d0
*      Sulfur dioxide2
      SO2i = 0.0109d0
*      Number of limestone particles
      pnum = sm/(pi*dp**3/6.0d00*rhol)

*      External area of particles per bed volume
      ap = pi*dp**2*pnum/vbed
*      Grain area at reaction radius
      ac = (y(4)/rgrain)**2*rhoba*sgs
*      Particle area at reaction radius
      ar = 4.0d0*(pi*y(9)**2)*pnum/vbed

*      Effective diffusivity of CO2 in particle (m^2/s)
      deffc = 1.4d-4
*      Effective diffusivity of SO2 in particle (m^2/s)
      deffs = 2.96d-5*dexp(-time/60.0d0)
*      Product layer thickness
      tpl = rgrain - y(4)

*      Product layer diffusivity (m^2/s)
      dpl = 1.0d-14

*      Effectiveness factor
      if (tpl.le.0.0) then
        phis = dp/2.0d0*(rs*rhop*sgs/deffs)**0.5
      else
        phis = dp/2.0d0*(dpl/tpl*rhop*sgs/deffs)**0.5
      endif

```

```

      etas = 3.0d0/phis**2*(phis/dtanh(phis) - 1.0d0)
*   Rates
*
*   SULFATION

      f(1) = -cbed*(y(1) - SO2i) + hs*ap*(y(2)-y(1))
      f(2) = hs*ap*(y(1)-y(2)) + etas*dpl/tpl*ac*(y(3)-y(2))
      f(3) = etas*dpl/tpl*ac*(y(2)-y(3)) - rs*ac*y(3)
      f(4) = - rs*56.0d0*y(3)/rhog

*
*   CALCINATION
      if (y(9).le.0.0) then
      f(5) = 0.0d0
      f(6) = 0.0d0
      f(7) = 0.0d0
      f(8) = 0.0d0
      f(9) = 0.0d0
      else
      f(5) = -cbed*(y(5) - CO2i) + hc*ap*(y(6) - y(5))
      rdif = 1.0d0/y(9) - 2.0d0/dp
      dummy = pnum/vbed
      f(6) = hc*ap*(y(5) - y(6))+4.0d0*pi*deffc/rdif*(y(7)-y(6))*dummy
      f(7) = 4.0d0*pi*deffc/rdif*(y(6)-y(7))*dummy + rc*ar
      f(8) = -rc*100.0d0*ar*vbed
      f(9) = -rc*100.0d0/rhol
      endif

      return
      end

```